AD-A247 935

AD

MTL TR 91-38

ADVANCED BAFFLE MATERIALS TECHNOLOGY DEVELOPMENT

DTIC
S ELECTE
MAR 25 1992
D D

October 1991

E. A. JOHNSON, C. J. VONBENKEN, W. D. HALVERSON,
R. D. EVANS, J. S. WOLLAM, and B. W. MURRAY

Spire Corporation
Patriots Park
Bedford, MA   01730

FINAL REPORT   Contract DAAL04-87-C-0036

Prepared for

U.S. ARMY MATERIALS TECHNOLOGY LABORATORY
Watertown, Massachusetts   02172-0001

92-07512

92 3 24 075

The findings in this report are not to be construed as an official Department of the Army position, unless so designated by other authorized documents.

Mention of any trade names or manufacturers in this report shall not be construed as advertising nor as an official indorsement or approval of such products or companies by the United States Government.

DISPOSITION INSTRUCTIONS

Destroy this report when it is no longer needed.
Do not return it to the originator.

REPORT DOCUMENTATION PAGE	READ INSTRUCTIONS BEFORE COMPLETING FORM

1. REPORT NUMBER MTL TR 91-38	2. GOVT ACCESSION NO.	3. RECIPIENT'S CATALOG NUMBER

4. TITLE *(and Subtitle)* ADVANCED BAFFLE MATERIALS TECHNOLOGY DEVELOPMENT	5. TYPE OF REPORT & PERIOD COVERED Final Report – June 1987 to September 1990
	6. PERFORMING ORG. REPORT NUMBER FR-10106

7. AUTHOR(s) E. A. Johnson, C. J. VonBenken, W. D. Halverson, R. D. Evans, J. S. Wollam, and B. W. Murray	8. CONTRACT OR GRANT NUMBER(s) DAAL04-87-C-0036

9. PERFORMING ORGANIZATION NAME AND ADDRESS Spire Corporation Patriots Park Bedford, MA 01730	10. PROGRAM ELEMENT, PROJECT, TASK AREA & WORK UNIT NUMBERS D/A Project: 63224C

11. CONTROLLING OFFICE NAME AND ADDRESS U.S. Army Materials Technology Laboratory ATTN: SLCMT-PR Watertown, Massachusetts 02172-0001	12. REPORT DATE October 1991
	13. NUMBER OF PAGES

14. MONITORING AGENCY NAME & ADDRESS(if different from Controlling Office)	15. SECURITY CLASS. (of this report) Unclassified
	15a. DECLASSIFICATION/DOWNGRADING SCHEDULE

16. DISTRIBUTION STATEMENT *(of this Report)*

Approved for public release; distribution unlimited.

17. DISTRIBUTION STATEMENT *(of the abstract entered in Block 20, if different from Report)*

18. SUPPLEMENTARY NOTES

John F. Dignam COR

19. KEY WORDS *(Continue on reverse side if necessary and identify by block number)*

Optical baffles	Beryllium alloys	Hardened baffles
Optical seekers	Martin black	Texturing
Aluminum alloys	Ion-assisted texturing	Baffles

20. ABSTRACT *(Continue on reverse side if necessary and identify by block number)*

(SEE REVERSE SIDE)

Block No. 20

ABSTRACT

~~Optical~~ sensors for strategic defense will require optical baffles to achieve adequate off-axis stray light rejection and pointing accuracy. Baffle materials must maintain their optical performance after exposure to both operational and threat environments. In addition, baffle materials must not introduce contamination which would compromise the system signal-to-noise performance or impair system mission readiness.

Critical examination of failure mechanisms in current materials has suggested an innovative approach to producing superior baffle materials. The highly textured coatings of the best current baffle materials are quite fragile and contribute to system contamination problems. Spire has developed technology to texture the substrate directly, thereby removing minute, fragile interfaces subject to mechanical failure. This program has demonstrated that ion beam texturing produces extremely dark surfaces which are immune to damage from ordinary handling. This technology allows control of surface texture feature size and hence the optical wavelength at which the surface absorbs.

The USAMTL/Spire program has produced dramatic improvements in the reflectance of ion beam textured aluminum without compromising mechanical hardness. In simulated launch vibration tests, this material produced no detectable contamination on adjacent catcher plates. By following the recommendations in this report, the Army can extend this technology to beryllium and exploit these technological breakthroughs to meet the stray light suppression needs of advanced sensor systems.

TABLE OF CONTENTS

LIST OF ILLUSTRATIONS

LIST OF ILLUSTRATIONS (Continued)

LIST OF ILLUSTRATION (Continued)

LIST OF ILLUSTRATIONS (Concluded)

LIST OF TABLES

SECTION 1

EXECUTIVE SUMMARY

Although baffles are a passive component of telescope systems, they are physically quite large and occupy much of the space and weight in typical sensor systems (Figure 1-1). In many sensor designs, the baffling governs the off-axis stray light rejection and hence the signal-to-noise performance of the system. To perform their primary mission of absorbing in-band stray light, baffle materials must be exposed to a variety of out-of-band radiation. Thus, the baffle is the most exposed component of an optical sensor system in the natural and radiation-enhanced environment of space. It must successfully perform its mission so that the sensor system can accomplish its crucial role in strategic defense.
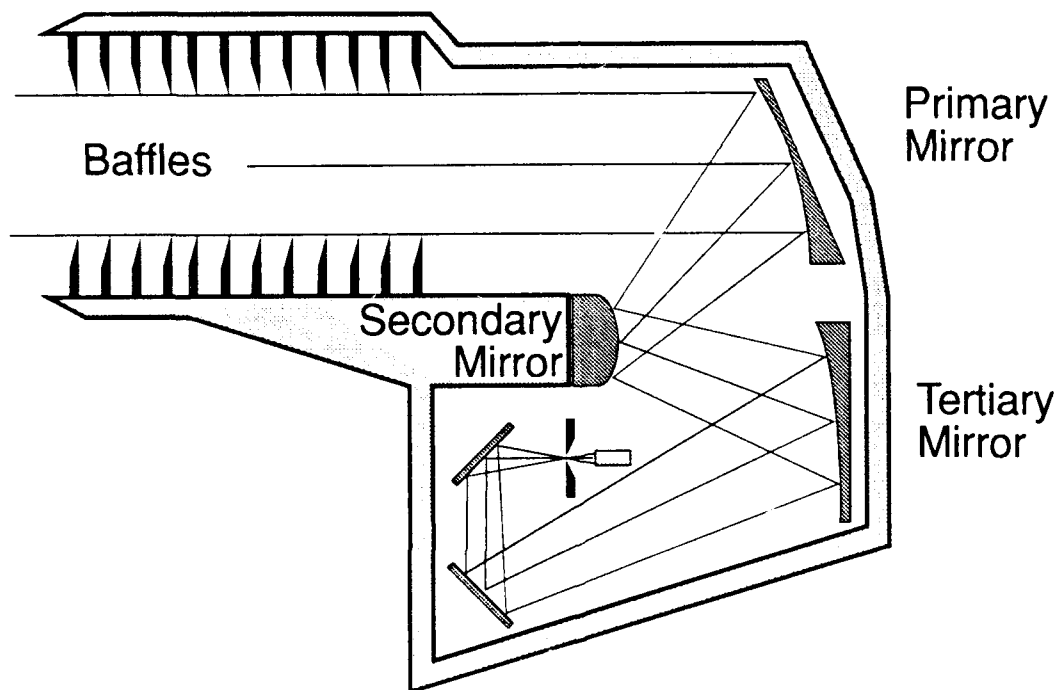
FIGURE 1-1. SCHEMATIC OF TYPICAL TELESCOPE DESIGN.

The advanced baffle material development program, sponsored by the U.S. Army Material Technology Laboratory, was initiated in June 1987. It has been highly successful in identifying the deficiencies of presently available baffle materials and in making rapid progress in the development of promising new materials and processing techniques. Strategic defense mission needs on both short and long time-scales, require baffle materials with optical, mechanical, and radiation hardness specifications which are presently not available. The diagram of Figure 1-2 schematically shows the necessary evolution of optical baffle materials for strategic defense missions. Presently, state-of-the-art baffle materials have either good optical performance, high mechanical strength, adequate space-environment performance, or hardness against nuclear or laser radiation. No commercial material exists which has even two of the necessary combined qualities, let alone all four. Flight Test Validation (FTV) missions will require, in the near term, baffle structures which have good optical and mechanical performance, as shown in Figure 1-2. In the long term, baffles for tactical missions will require materials which are qualified in all four areas: optical, mechanical, space environment, and radiation hardness.
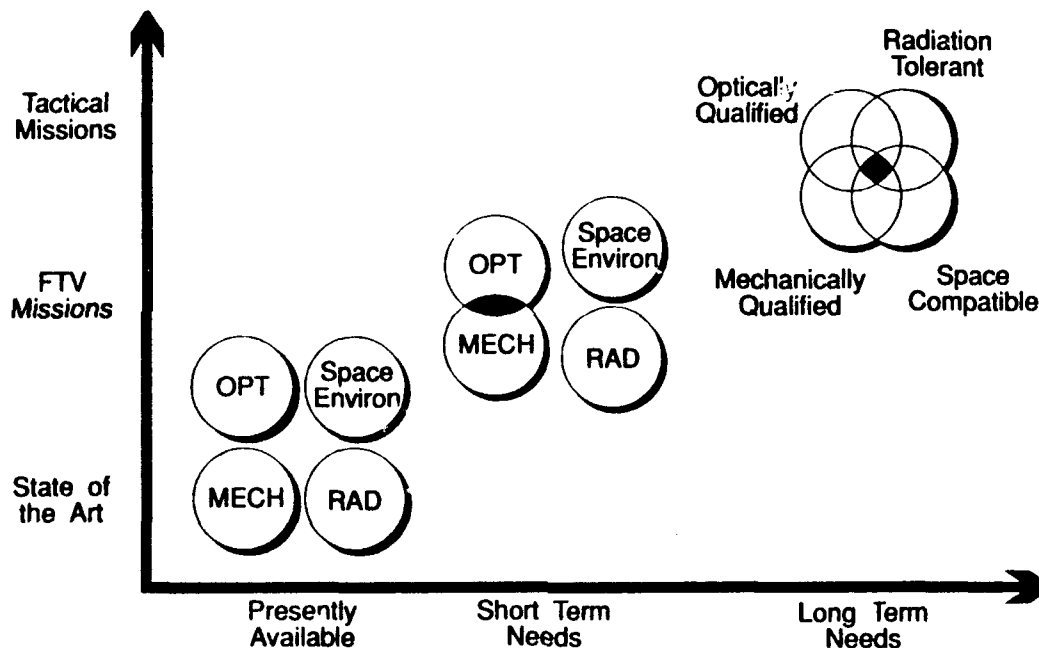
FIGURE 1-2.   EVOLUTION OF OPTICAL BAFFLE MATERIALS FOR STRATEGIC DEFENSE SYSTEMS.

During this program, an ion-assisted texturing process was developed to form mechanically strong and optically black surfaces on metals. The technique was successfully applied to aluminum substrates, and preliminary tests indicate that it can be applied to beryllium metal which is the material of choice for nuclear radiation hardness (Figure 1-3). Development of the surface texturing process on inexpensive, readily available aluminum substrates can satisfy near-term FTV mission requirements before complete development of texturing for beryilium, a metal with limited availability and high cost which produces highly toxic by-products. Ion-assisted texturing techniques developed for aluminum will be applicable, with little modification, to beryllium processing.
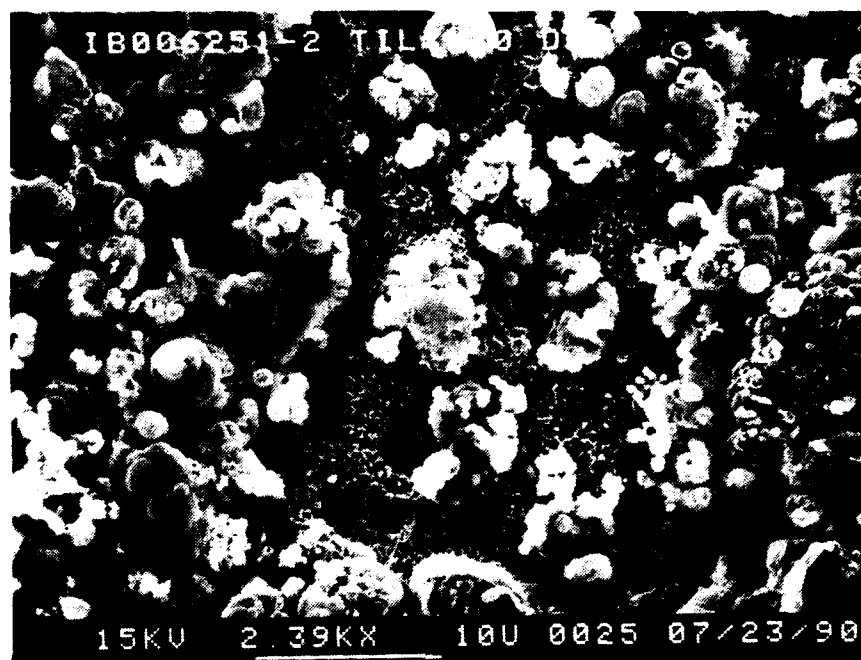
FIGURE 1-3.   SCANNING ELECTRON MICROGRAPHS OF TEXTURED ALUMINUM.

Concurrently, Spire has developed an ion-assisted technique to form thin ceramic over coatings which are optically absorptive, chemically inert, very resistant to radiation, and highly adherent to a variety of substrates. In addition, results from a Delta Star rocket experiment carrying a Spire made sample indicates tremendous promise for ceramic hard coatings in preventing atomic oxygen erosion of space based structures (Figure 1-4). The sample tested was a boron nitride coating deposited by a ion beam assisted deposition technique involving physical vapor deposition of boron (B) concurrent with nitrogen ion bombardment. Boron nitride as well as other ceramic coatings (Si_3N_4, Al_2O_3) produced at room temperature developed superior adhesion and high chemical inertness and appear as likely candidates for affording protection against atomic oxygen attack. The ceramic coatings have also been shown to improve the mechanical strength and radiation hardness of a commercial baffle material (Martin black) and to improve the optical performance of Spire's textured aluminum.

1 - 3

Quartz Crystal Microbalance Data From Delta Star Mission

FILM THICKNESS ($\mu g/cm^2$)

40

30

20

10

0

IBED BN Film
slope: $-1.65 \times 10^{-3} \mu g/cm^2/hr$

Parylene
Control Film
slope: $-0.20 \mu g/cm^2/hr$

0   48   96   144   192   240   288   336

TIME ELAPSED FROM LAUNCH (hours)
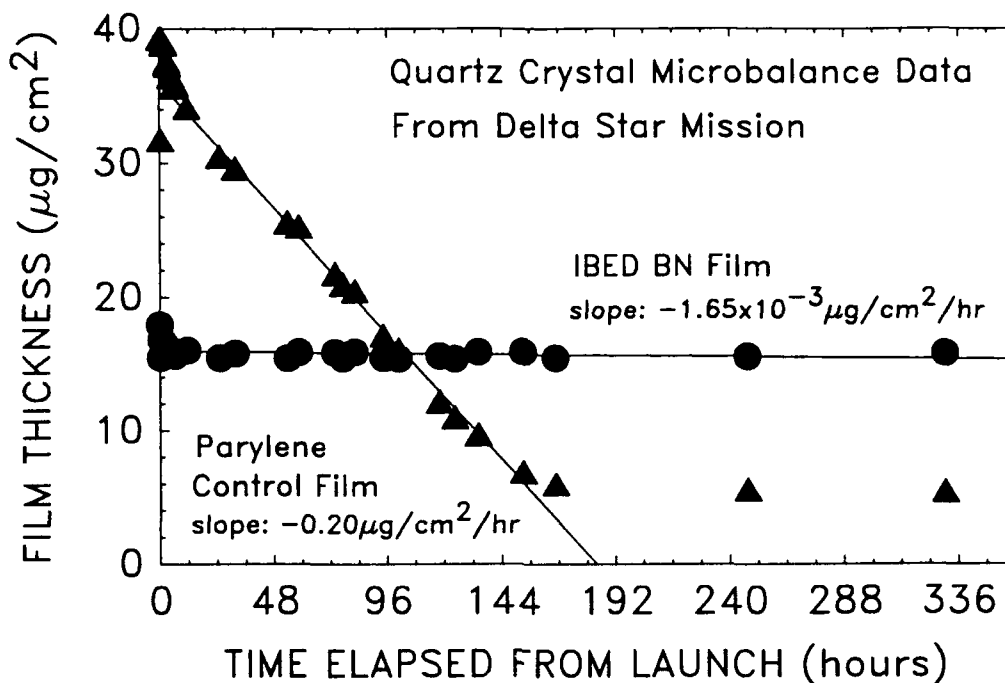
FIGURE 1-4.   EROSION RATE FOR SPIRE MANUFACTURED BORON NITRIDE FILM.

The Spire/MTL program for Advanced Baffle Materials Technology Development has produced a critical examination of the optical performance, flight-worthiness, and radiation hardness of current commercially available baffle materials. Of more than fifty materials tested, only a few met optical performance specifications typical of advanced strategic defense sensor systems, and none of the optically qualified materials survived simulated launch and flight vibration. Because of this, Functional Technology Validation (FTV) missions with imminent launch dates have an urgent need for improved baffle materials which are optically dark and mechanically hard. Tactical missions, with somewhat later launch dates, have additional requirements for materials capable of performing their mission in a threat environment.

Careful study of results from testing of current baffle materials has produced a detailed understanding of the fundamental failure mechanisms in these materials. This understanding, in turn, has enabled rapid identification and optimization of processes for producing coupons of superior baffle materials. The program has relied exclusively on processes which are flexible and which allow tailoring of optical properties, mechanical properties, and radiation hardness. Although aluminum was the vehicle for this process technology development during the initial stages of the program, the process for aluminum may be easily transferred to beryllium to form more radiation tolerant baffle materials.

SECTION 2

PROGRAM OVERVIEW

2.1 CURRENT BAFFLE TECHNOLOGY

To determine the state-of-the-art of baffle technology, an extensive search of both the classified and unclassified literature was conducted and a "library" containing more than 550 documents was compiled. Sources included a search of the DASIAC system in Santa Barbara for data from classified programs; a survey of relevant files maintained at the Army's Advanced Materials Technology Laboratories (Watertown, MA) and Strategic Defense Command headquarters (Huntsville, AL); and searches through the following databases:

- NTIS:
  - International Aerospace Abstracts Database
  - Astronomical Telescopes: Performance Evaluation
  - Searchable Physics Information Notices Database
  - Optical Coatings: Processes, Materials, and Evaluations

- Engineering Information, COMPENDEX Database:
  - Telescopes Aboard Spacecraft

- Duston Associates:
  - Reviewed INSPEC, NTIS, SciSearch, Conference Papers Index for data on particle generation

- DIALOG

- DETIR Directed Energy Holdings (DASIAC)

Supplemental information on the characteristics of proprietary baffle materials under development at Aerojet, Ball Aerospace, Martin, and Rockwell International was obtained through program managers, with whom contacts were made largely with the assistance of Breault Research Organization. Breault maintains an extensive file of optical data on current baffle materials from which results were extracted as needed for this program. The baffle program library is still growing, it presently comprises more than 1,000 titles. More than 550 of these have been carefully reviewed by team members who have prepared short synopses of relevant information. A computerized catalog of the entire collection has been established and is updated continuously as new reference materials are identified.

From information contained in the "Baffle Library," nearly one hundred potential baffle materials were identified; working experience in space exists for a small number of these, most notably Chemglaze Z-306 (used on the Hubble Space Telescope) and Martin Black (Infrared Astronomy Satellite Telescope). Efforts were made to obtain samples of all one hundred for testing. About fifty were actually received.

Review of the library for optical data and hardness properties met with limited success, and in no instance was all the information necessary to estimate post-encounter performance of a baffle available. For a few baffle materials, data from Misty North and Diesel Train provide guidance on damage mechanisms and give points with which theory can be compared, but uncertainty in these observations is great. It was concluded that, for most materials, nuclear effects testing with an appropriate simulator, accompanied by analysis, would be needed to determine damage mechanisms and the change in optical performance as a function of nuclear conditions.

It was further concluded that the analytical capabilities necessary to compute mechanical and thermal response are largely in place although the necessary input data may be missing. PUFF-TFT or reduced versions computing energy transport and redistribution without coupled hydrodynamics should be adequate to permit correlation of theory with experiment for thin film baffle structures which can be approximated as a series of planes. No means of treating the response of textured surfaces to high intensity thermal pulses was found in the literature, therefore, an effort was initiated to create a technique for estimating energy deposition in such surfaces. This culminated in the "HOT-ROD" program developed under Task 2 of the program, described in Appendix D.

2.2 BAFFLE MATERIAL TEST METHODOLOGY

2.2.1 Optical Analysis

Total hemispherical reflectance measurements were performed on materials using a Xenon arc lamp, monochrometer, and integrating sphere. The set-up is pictured in Figure 2-1. Light from the arc lamp is focused onto the entrance slits of the monochrometer; output of the monochrometer is then collimated and focused onto the sample by a pair of lenses. The integrating sphere collects all forward scattering light, allowing the detector to measure reflectance. A pyroelectric detector with an NEP of 1E-7 watts is used. Signal-to-noise ratio with good samples (i.e., Martin Black) Is low, about 3 to 1. The monochrometer was scanned by a synchronous motor driving the grating through a sine bar; lenses used were planoconvex and biconvex and made of borosilicate glass. In addition, a 3.39 micron He:Ne and a 10.6 micron CO_2 laser can also be used as illumination sources.

Reflectance measurement is obtained by measuring a calibrated standard, then the sample. Output of the sample is divided by the output of the reference and then multiplied by the reflectance of the standard. Standards were purchased from Reflectance Research, North Sutton, NH, and calibrated to NBS standards with relative accuracy of half a percent. Standards used in the 400 to 2500 nanometer range had reflectivities of 1.1% and 98%. For the infrared region, a diffuse gold standard with reflectivity of 96% was used.

Optical testing capabilities were extended through acquisition of a Fully Automated SCATterometer (FASCAT) from Breault Research for BRDF measurements. The FASCAT (Figure 2-2.) is equipped to make BRDF measurements at 10.6 microns and 633 nanometers using CO_2 and He:Ne lasers, respectively, with computer-controlled optics and menu-driven data analysis. It is housed in a Class-1000 clean room environment to minimize particle contamination, an effect which can greatly influence BRDF measurements.
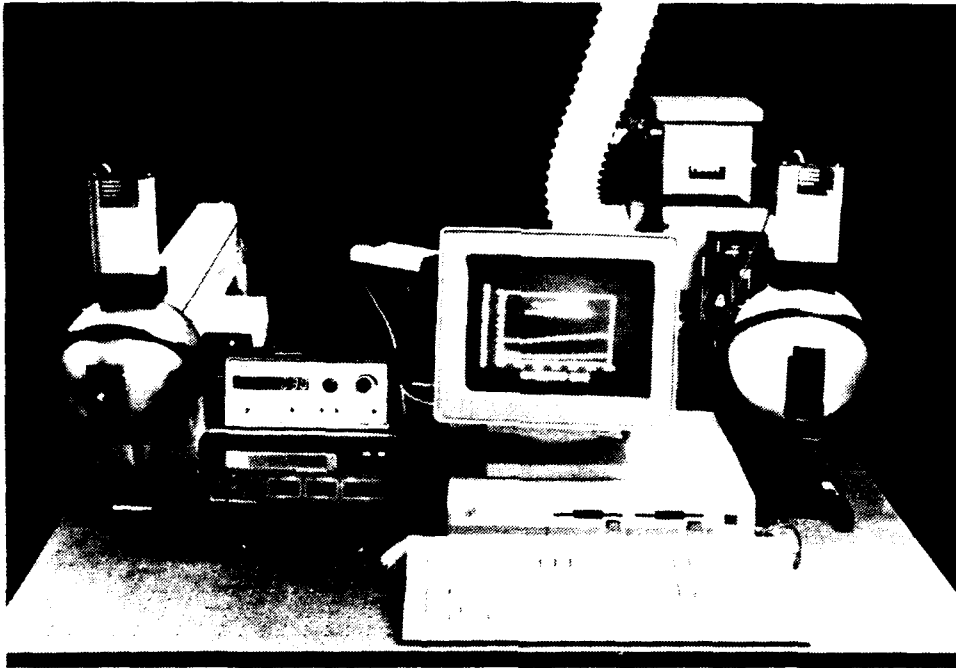
FIGURE 2-1.   PHOTOGRAPH OF TOTAL HEMISPHERICAL REFLECTANCE
               MEASUREMENT SYSTEM.
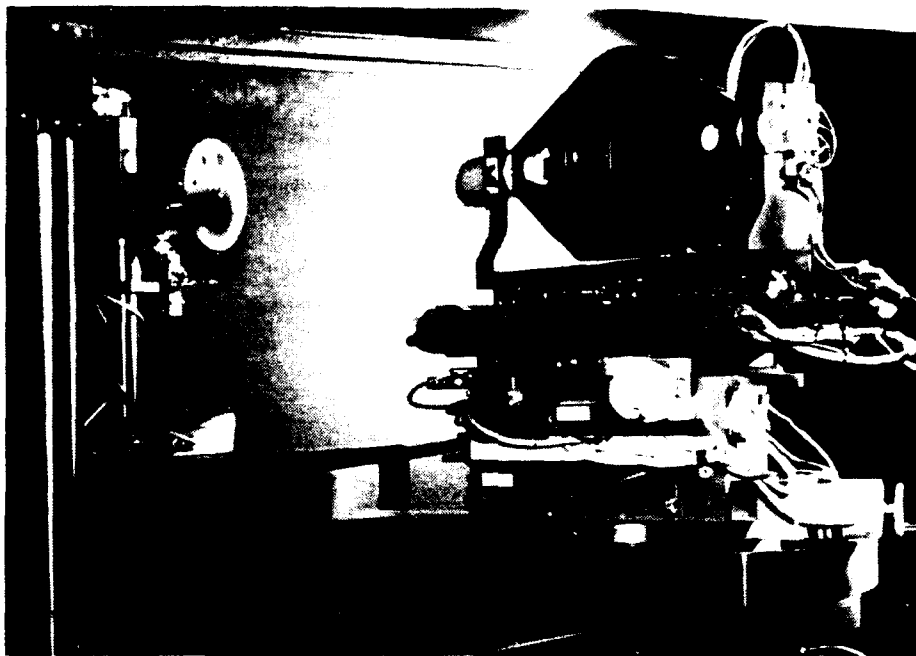
FIGURE 2-2.   PHOTOGRAPH OF THE FASCAT.

2.2.2 Pulsed Electron Irradiation Facility

For many optical systems with a requirement for nuclear hardness, the primary mirror and optical baffle can exposed to the low energy X-rays generated by a nuclear device. Most of the energy released by such a device is carried predominantly by soft X-rays. An above-ground-test (AGT) simulation of nuclear weapons effects, therefore, would be the production of an intense burst of soft X-rays. However, the development of a pulsed X-ray source capable of satisfying all the requirements for AGT simulation has proved to be a difficult problem. Traditional flash X-ray machines, which rely on the bremsstrahlung from MeV electrons slowing down in a converter foil, produce hard X-rays with an energy spectrum which is cut off at the K-edge of the element making up the foil (e.g., Ta has a K-edge of 67 keV).

A new generation of pulsed plasma X-ray sources is currently under development. A recurring problem with these machines is that debris from the plasma discharge (typically fueled by an exploding wire or gas puff) contaminates target surfaces. The debris often masks the radiation damage incurred by the X-rays and prevents meaningful optical scatter data to be obtained. In order to shield samples from this shower of debris, the X rays from plasma machines are typically passed through tight collimating apertures. Unfortunately, this severely restricts the area of a target which can be illuminated. A second concern for these pulsed X-ray sources is the lack of radiation fluence reproducibility from shot to shot. The availability of a contaminant-free radiation source with a reproducible fluence output that can be used for developing new optical surfaces and optimizing optical fabrication processes is at present highly limited.

At Spire, three pulsed electron beam sources (SPI-PULSE 300, 5000, 6000) are routinely used in the development and optimization of mirrors, optical coatings, and baffle materials. The low cost in maintaining these sources and their long term reliability have allowed rapid process optimization for the fabrication of baffle materials.

SPI-PULSE 300

The SPI-PULSE 300 accelerator operates by allowing a $\approx$ 3.0 nF, 100 kV epoxy condenser to discharge through a field emission diode. The total energy store in the capacitor, at 100 kV charge, is roughly 15J (3.58 cal). The electron pulse emerging from the diode lasts roughly 60 nsec and has an approximately white energy spectrum between 0 and 50 keV. During each pulsed irradiation event, a resistive divider provides the voltage history of the diode while an inductive current monitor provides a current history. An electron energy spectrum may then be computed from the measured current and voltage traces. Figure 2-3 is a photograph of the SPI-PULSE 300, and Figure 2-4 is a schematic of its field emission diode.

Figure 2-5 illustrates typical diode voltage and current traces monitored with a fast digitizing oscilloscope. Using a Spire developed software package, the current-voltage trace can be used to generate a time-integrated electron energy spectrum. Another feature of the 300 is its ability to measure particulate debris blown off the sample surface. The Real Time Particle Monitoring (RTPM) system uses a He:Ne laser to measure particle speed and size by measuring the amount of light scattered by the ejected particulates. Figure 2-6 illustrates the apparatus. The height and breadth of the PMT generated pulses directly relate to the size and speed, respectively, of the particulates.
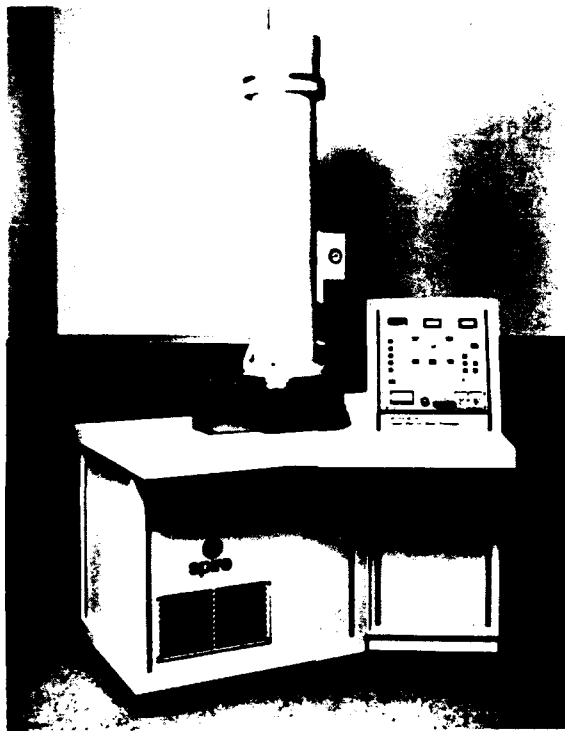
FIGURE 2-3. SPI-PULSE™ 300 PULSED ELECTRON BEAM GENERATOR.
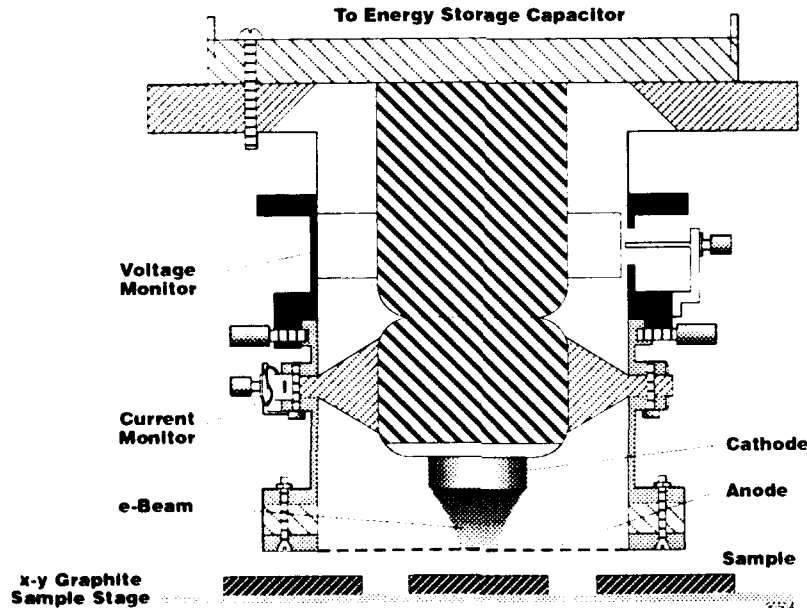
FIGURE 2-4.   SPI-PULSE™ 300 DIODE CONFIGURATION.   (The electron beam is accelerated from the cathode to the transparent W mesh anode (at ground potential) and then drifts through the anode to irradiate the sample. E-beam fluence can be reduced by placing W wire screens between the anode and sample to attenuate some of the beam without altering its energy distribution.)

2 - 5
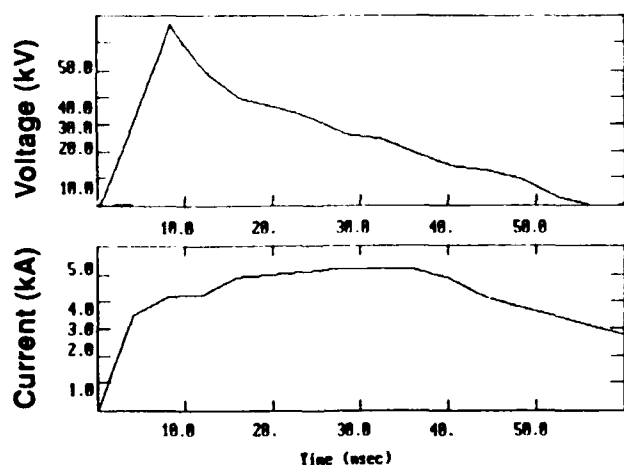
Current / Voltage Curves
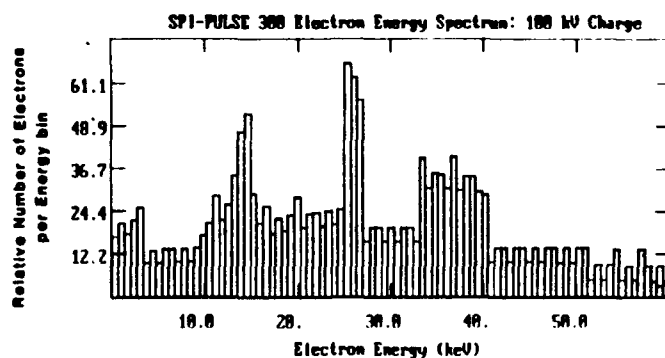
Electron Energy Spectrum in Beam

FIGURE 2-5.   MEASURED CURRENT AND VOLTAGE HISTORIES FOR A TYPICAL
RADIATION EVENT WITH THE CALCULATED ENERGY SPECTRUM.
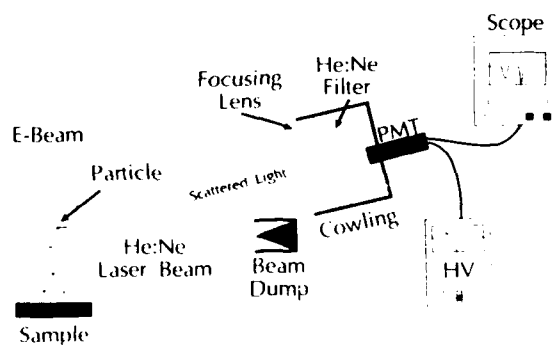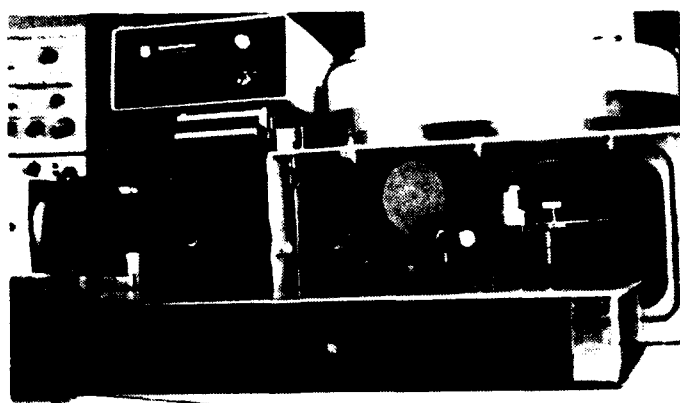
FIGURE 2-6.   APPARATUS USED TO MEASURE REAL-TIME MATERIAL BLOW-OFF.

SPI-PULSE 6000 AND 5000

In order to enhance Spire's X-ray simulation department, two SPI-PULSE's were purchased from the Chomerics Corporation. The SPI-PULSE™ 600 is currently in storage awaiting future expansion of the department, and the SPI-PULSE™ 6000 which underwent a complete refit in the summer of 1989. A map of peak fluence vs. charging voltage has been made (Figure 2-7). The machine was configured as follows:

Cathode:	1" Diameter Graphite
Anode:	Tungsten 30 x 30 Mesh
Cathode-Anode Gap:	0.080" (variable)
Anode-Sample Gap:	0.690" (variable)
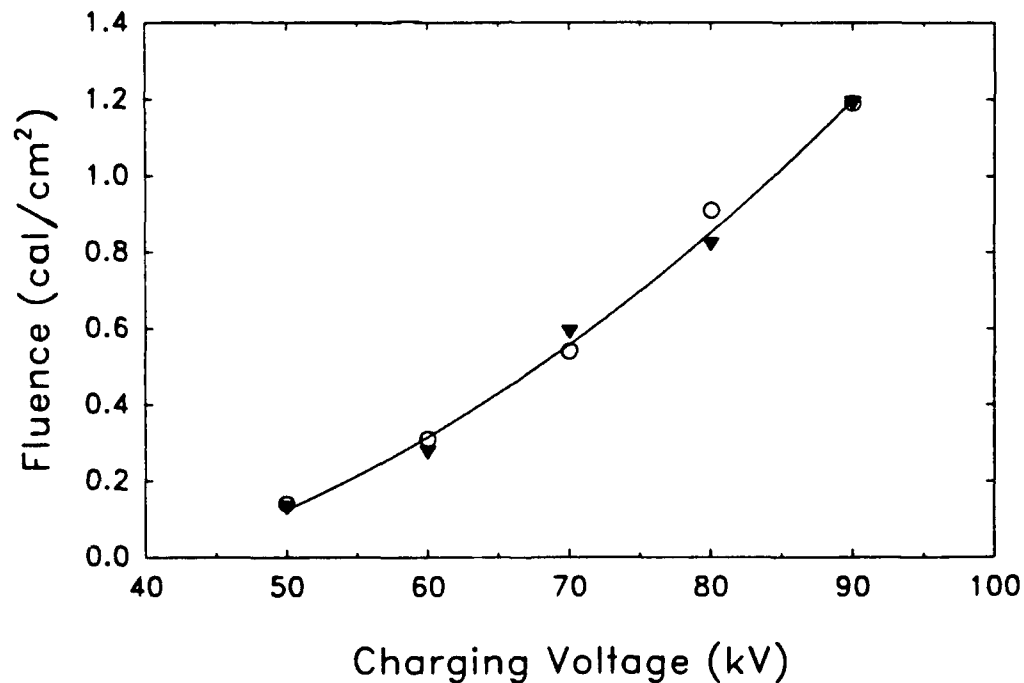
FIGURE 2-7. MAP OF PEAK FLUENCE VS. CHARGING VOLTAGE FOR THE SPI-PULSE 6000.

A map of fluence vs. distance from beam center was also developed (Figure 2-8). The beam is a smooth uniform gaussian for all charging voltages measured.
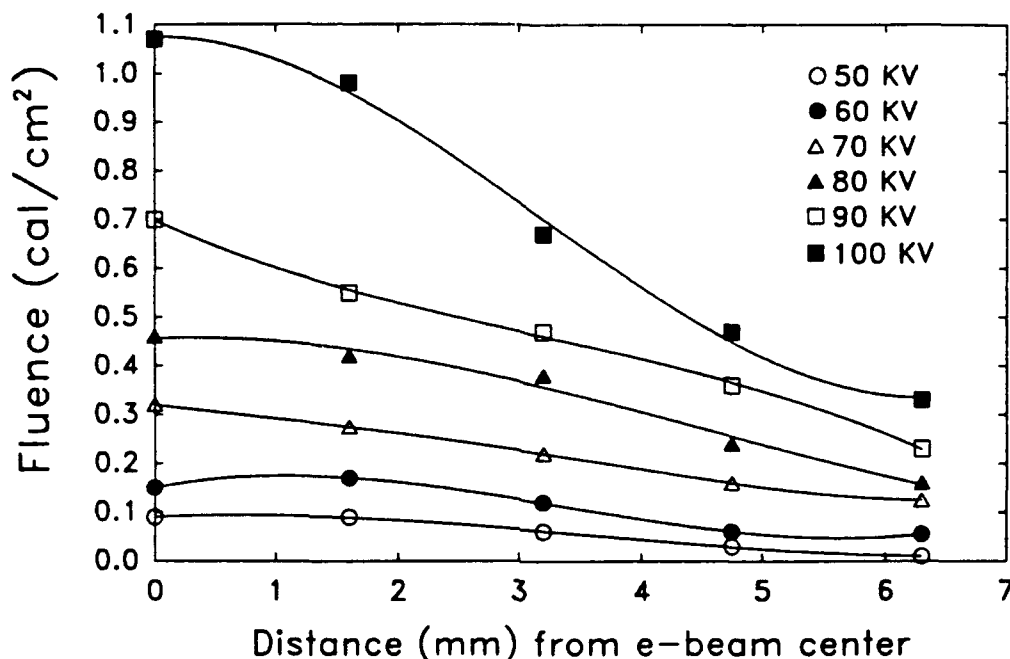
FIGURE 2-8. SPI-PULSE 6000 BEAM PROFILES.

With a 0.080" cathode-anode gap, a pulse width 100 nanoseconds was recorded. In order to more closely simulate a flash x-ray event, the cathode anode gap was adjusted to reduce pulse times to 60 nanoseconds. Figure 2-9 shows the progression of pulse width as a function of cathode-anode spacing.

The SPI-PULSE 6000 will complement Spire's electron irradiation facilities. The SPI-PULSE™ 5000, which is similar to the 6000 is committed to the testing of advanced beryllium mirrors. The 6000's beam, like the 300's can be analyzed with the fast digitizing oscilloscope.

2.2.3 Differences Between Intense Electron and X-ray Beams

Both electrons and photons can scatter from target atoms and from collective target atom excitations (phonons). Both electrons and photons can ionize target atoms and cause a cascade of secondary emission and other higher order events. Electrons though, have a finite chance of being involved in collisions with single target electrons or with collective target electron excitations (plasmons). Because of this, the range of electrons is shorter than the range of photons with the same kinetic energy.
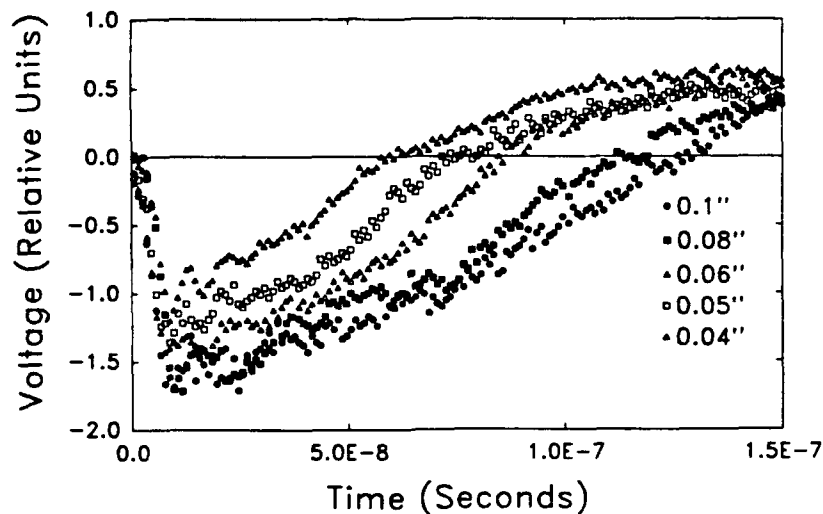
FIGURE 2-9. PULSE WIDTH VS. CATHODE-ANODE SPACING.

The most striking difference between intense electron and photon bombardment is that electrons carry electrical charge. Although all incident radiation causes some target ionization and some charge deposition through secondary events, electron beams deposit charge as a primary event. If all of the charge deposited by a pulsed electron beam (or even a small fraction of it) could be stored in the surface of a dielectric material, the resulting electric fields would be enormous.

Consider the [un-physical] case of a 100 kA/cm^2 current pulse which lasts for 0.120 µsec and deposits all of its charge in a uniform sheet on the surface of a target material. From elementary electricity and magnetism, Gauss's law gives the electric field at the surface:

$$E = \sigma/2\varepsilon_o = \frac{(I/da) \cdot dt}{2\varepsilon_o} = \frac{(10^5 \text{ A/cm}^2) \cdot 10^{-7} \text{sec}}{2 \cdot 8.85 \times 10^{-12} \text{ F/m}} = 5.65 \times 10^{12} \text{ V/m}. \tag{1}$$

This electric field is unrealistically large, well above the breakdown strength of any laboratory vacuum or any known material. Even if a small fraction of this charge were to be stored at the dielectric surface, the resulting electric field could exert a dramatic influence on the path of incoming electrons.

Charge Storage in Irradiated Dielectrics: The Literature

A range of observable phenomena accompany charge buildup in electron-irradiated dielectric materials. One effect is range reduction of incoming electrons[1] and, experimentally, the beam electrons may be used as a probe of the local electric field.[2] Another effect which has been used to study charge buildup is bulk dielectric breakdown and spontaneous discharge.[3] Other workers have studied surface flash-over in during electron bombardment of dielectrics.[4] Concerns about charge buildup in space craft and re-entry vehicles has prompted a great deal of interest in dielectric charging. Because of this interest, much of the available data on these phenomena has been compiled in convenient hand-book form for design work.[5]

One important phenomenon accompanying intense irradiation (with photons or electrons) of dielectric materials is the ionization of target atoms. Because of this and the consequent promotion of atomic electrons into conduction bands of the solid, the population of charge carriers in the material increases dramatically. Radiation induced conductivity is exceedingly sensitive to dose rate and at very high dose rates, insulating materials can become conductors. Physically, this is sensible since high dose rates must be represented by high frequency electric field terms and the distinction between conductors and insulators is artificial at high frequencies.

Radiation induced conductivity has been studied extensively, and several of the general references cited above contain overviews of the phenomenon. In addition, there are good analytical models for radiation induced conductivity[6] and for the dependence of radiation induced conductivity on various experimental parameters.[7] Experimentally, the strongest influence on radiation induced conductivity is the dose rate.[8]

Electron Range and Straggle

Many of the energy loss processes which characterize electron stopping in solid surfaces are discreet inelastic scattering events. Because of this, stochastic models, implemented through Monte Carlo computer codes, have been widely used to compute energy deposition profiles for electrons striking a solid surface.[9] However, because of applications interest in electron energy loss for electron microscopy and electron beam micro-analysis, excellent tabulated cross sections are available for electrons with energies between 1 keV and 100 keV.[10]

In these calculations, the depth/dose profile for electrons bombarding a surface is assumed to be a fixed function of the electrons' kinetic energy. In each case, the mean electron range and straggle (the centroid and width of the energy deposition profile) are computed by analytic fits to the tabulated cross sections.

Energy deposition was evaluated as a function of time in 10 nsec steps. For each time step, the instantaneous voltage determines the depth and width (range and straggle) of the electron energy deposition profile while the instantaneous current determines the amount of charge deposited during a time step. Figure 2-10 shows the time history of the electron beam depth/dose relation. The analysis proceeds by taking into account a retarding voltage, due to charge build-up, and leakage current, due to radiation induced conductivity, during each 10 nanosecond time step.

Effect of Hypothetical Stored Charge

The model for the calculations of charge build-up is that the electrons which strike the target during a given time step form a uniform sheet of charge buried at a depth equal to the mean electron range for that time step.
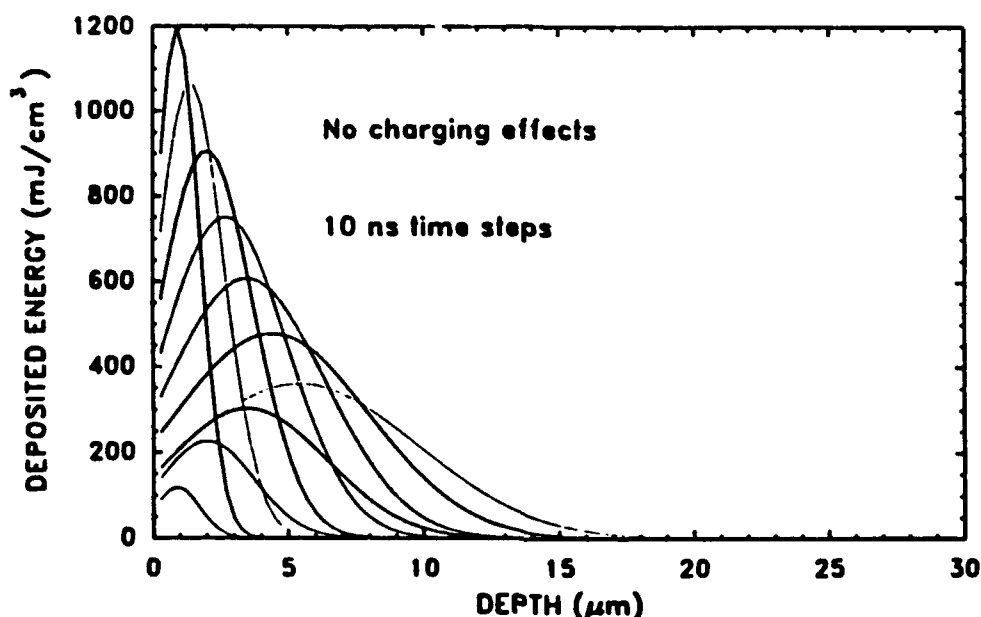
FIGURE 2-10. TIME DEPENDANT DEPTH DOSE PROFILES FOR ELECTRON ENERGY
DEPOSITION IN ALUMINA. These profiles represent the range and strength
of electrons in 10 nanosend time steps.

This charge distribution generates a strong repulsive potential in the dielectric medium
and may reduce the range of incoming electrons. In this calculation, the electric potential is
evaluated at the interface between the dielectric slab and the vacuum. The energy of this
"retarding potential" is then subtracted from the incoming electron beam energy during all
subsequent time steps and is therefore allowed to reduce the range of beam electrons. The
retarding potential may be found analytically from the definition of electric potential and a
straight-forward integral over the charge distribution:

$$V_r = \frac{2\pi \rho \left[\sqrt{area/\pi - z_0^2} - z_0 \right] + V_{ro}}{\epsilon_r \epsilon_0}$$ (2)

where $\rho = Idt/area$, $\epsilon_r = 4.85$ is the relative permittivity of the medium, z_0 is the mean depth of
electron penetration, and V_{ro} is the accumulated retarding potential from the previous steps. If
all the charge is stored in the dielectric, values of V_r (for a square centimeter beam spot) quickly
climb into the megavolt range. After the first time step, the potential is so high that it repels all
incoming electrons. Physically, this corresponds to beam instability as enormous local electric
fields deflect the beam (or perhaps cause the beam to bounce back). To illustrate the
phenomenon, only a small portion of the built up charge was allowed to remain at its deposition
site. This way, the charge build-up is much slower, and the calculation can proceed through
several time steps before building un-realistically large electric fields. Figure 2-11 demonstrates
the effect with 0.4% of the total charge retained.
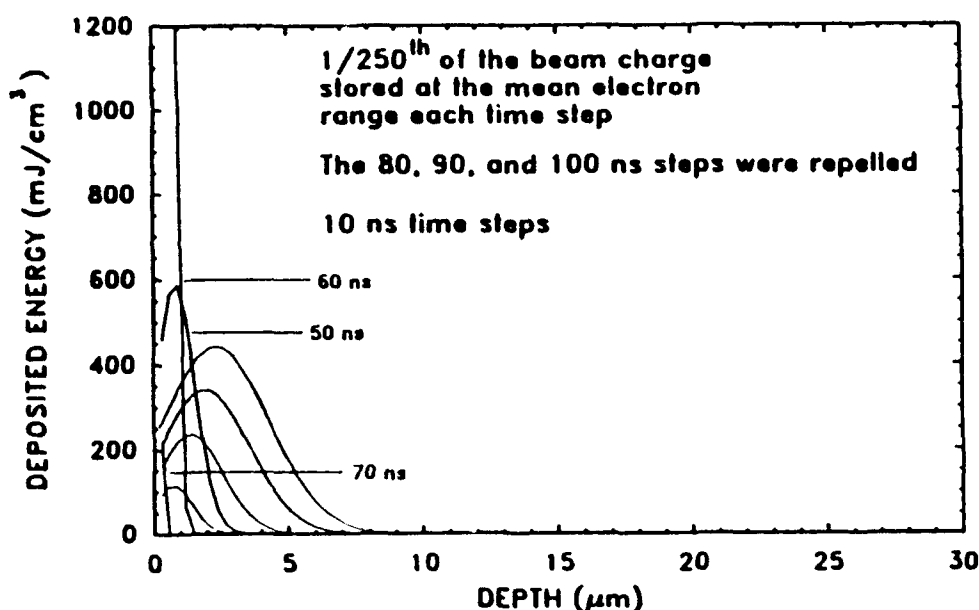
FIGURE 2-11.   DEPTH DOSE PROFILES IN A CHARGED DIELECTRIC SLAB. 0.4% of the total deposited charge is stored at the mean electron range during each time step. The charge is not allowed to dissipate; stored charge is used to compute electric field at the simple front face.

Effect of Radiation Induced Conductivity

The basic computational framework may be extended to allow for radiation induced conductivity. This conductivity allows the accumulated charge to dissipate to the front surface of the dielectric. (Because of the low surface flash-over strength, the front surface is assumed to be grounded.) The model for voltage decay in this problem is a resistor-capacitor circuit. The capacitance of the slab of alumina is $(\varepsilon_o \varepsilon_{area})/z_o$, or $8.8 \times 10^{-11} F$. To find the resistance, the radiation induced conductivity is needed. For each time step, the tabulated radiation induced conductivity is multiplied by the instantaneous dose rate. The instantaneous dose rate, in turn, is given by the depth/dose profile for the previous time step.

The resistivity is inversely proportional to the conductivity and this gives the resistance of the dielectric slab. The resistance and capacitance of the slab lead to a characteristic time constant, RC, for the potential drop across the slab. The actual retarding voltage will be dependent upon the exponential decay resulting from the RC circuit model, $V_r = V_r' e^{-dt/\tau}$. Here V_r' is the retarding voltage calculated with no charge dissipation and τ is the RC time constant. It turns out that in actual calculation the time constant for relaxation is in the order of picoseconds. Because of this, as illustrated in Figure 2-12, the retarding voltage build-up is vanishingly small.

$$RIC = 2.43 \times 10^{-17} \frac{\text{seconds}}{\Omega \text{ cm rad}}$$

$t_c = RxC$ (typically 30 ps)

$V_r = V_r' e^{-t/t_c}$

10 ns time steps

DEPOSITED ENERGY (mJ/cm^3)

DEPTH (μm)
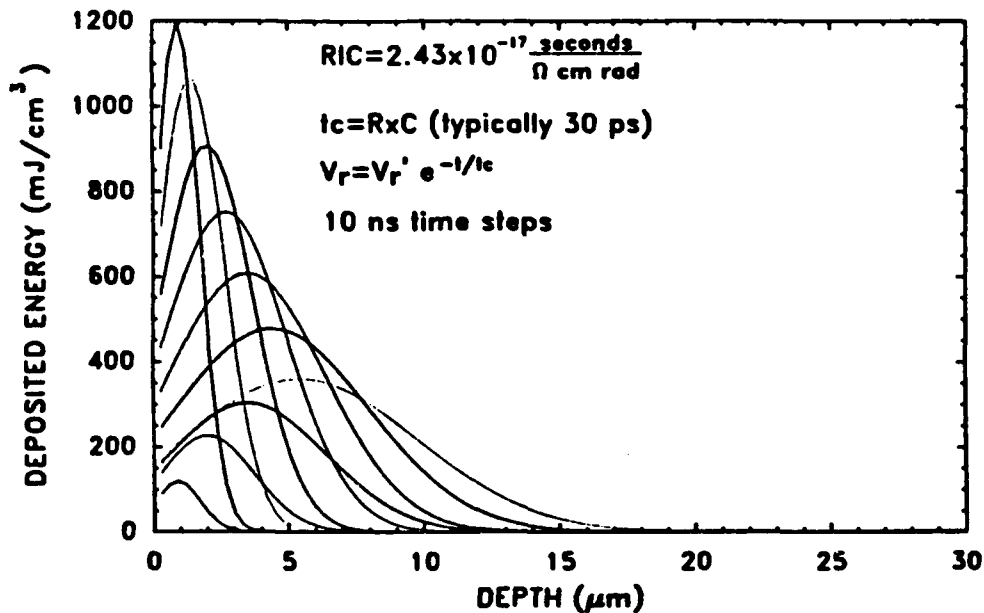
FIGURE 2-12. DEPTH DOSE PROFILES WITH SAMPLE CHARGING AND RADIATION INDUCED CONDUCTIVITY. As described in the text, measured RIC values are used to compute an RC time constant for dissipation of the stored charge after each time step.

2.2.4 Mechanical/Environmental Testing

Vibration Testing Fixture

The operational environment baffles must withstand, consisting of long-term storage, launch, and on-station conditions, is severe. To evaluate effects of launch, a fixture was built for testing small baffle samples in centrifuge and vibration facilities. The fixture was used to obtain data on the production of particles during three axis shake table testing at accelerations to 21g and frequencies to 2000 Hz. Figure 2-13 is an exploded view of the test fixture. Two samples can be mounted, along with a blank to be used as a control.

Atomic Oxygen Exposure

The principal atmospheric species at altitudes from 150 km to about 700 km is neutral atomic oxygen; ionized particle densities are at most a decade less than the neutral O density over this range. Figure 2-14 shows the neutral particle densities as a function of altitude for the extremes of the solar cycle.[1] From this figure we find that the "ram" flux of O atoms on a satellite varies between 8×10^{15} /cm^2/s and 8×10^{12} /cm^2/s at altitudes between 200 km and 500 km. Flights on the Space Shuttle have clearly indicated that interactions between materials and atomic oxygen, the predominant atmospheric species in low earth orbit (LEO), can cause serious technical problems for the Space Station. These interactions are characterized by a "glow" around surfaces exposed to the ram flux of oxygen atoms and, more significantly, accelerated

Vacuum Valve

Exploded View

Assembled View

Silicon Wafer
Catcher Plate Holder

Sample Holder
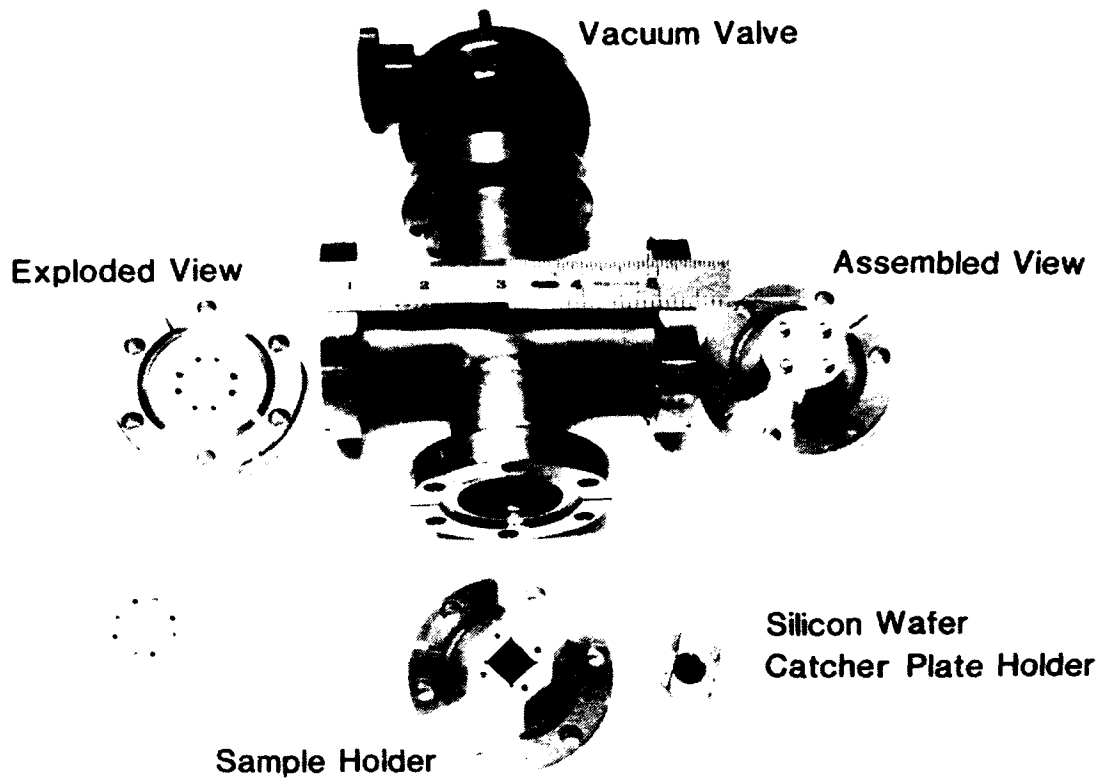
FIGURE 2-13.   EXPLODED VIEW OF VIBRATION TEST FIXTURE.
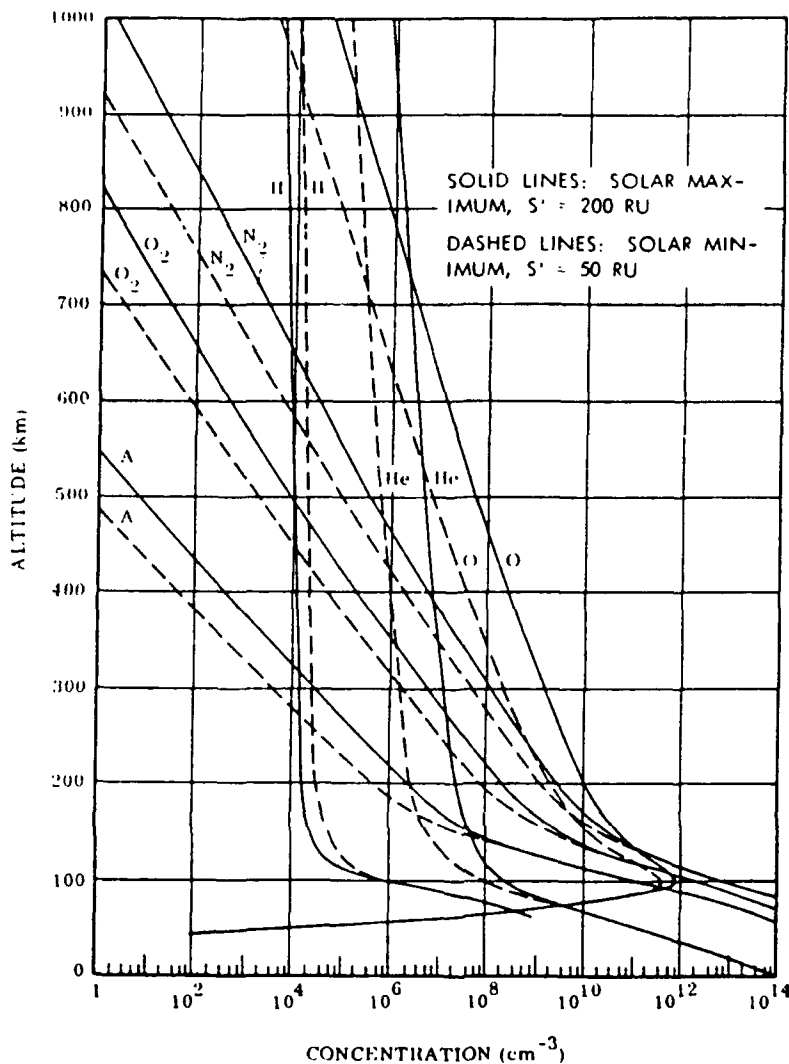
FIGURE 2-14. DISTRIBUTIONS OF MAJOR CONSTITUENTS OF NEUTRAL ATMOS-
PHERE AT EXTREMES OF SOLAR ACTIVITY.[19]

degradation of organic and metal-coated materials. Important space materials including Kapton, aluminum-coated Kapton, Mylar, Kevlar rope, silver strips, carbon-filled epoxies, and paints showed serious surface recession, loss of surface gloss or emissivity, or loss of mechan ical strength during the short Shuttle flights.[13,14] Projections based on the Shuttle flight data and preliminary laboratory experiments[2,15,16,] indicate that this degradation will not be acceptable over the 20 to 30 year lifetime of the Space Station.[17] The work on atomic oxygen erosion of materials pioneered by Banks, Rutledge, et. al. at the Lewis Research Center,[18] Table 2-1, (from reference 18) indicates that for a variety of materials, atomic oxygen erosion is a serious problem.

2 - 15

TABLE 2-1.   EROSION YIELDS OF VARIOUS MATERIALS EXPOSED TO ATOMIC OXYGEN IN LOW-EARTH ORBIT.

Material	Erosion yield, $\times 10^{-24}$ cm^3/atom	Reference
Aluminum (150 Å)	0.0	1
Aluminum–coated Kapton	.01	2
Aluminum–coated Kapton	.1	2
Al$_2$O$_3$	<.025	3
Al$_2$O$_3$ (700 Å) on Kapton H	<.02	4
Apiezon grease 2 mm	>.625	5
Aquadag E (graphite in an aqueous binder)	1.23	6
Carbon	1.2	7, 1, 8, 9
Carbon (various forms)	.9 to 1.7	10
Carbon/Kapton 100XAC37	1.5	11
401-C10 (flat black)	.30	12
Chromium (123 Å)	Partially eroded	14
Chromium (125 Å) on Kapton H	.006	15, 16
Copper (bulk)	0.0	17
Copper (1000 Å) on sapphire	.007	15, 16
Copper (1000 Å)	.0064	14
Diamond	.021	17
Electrodag 402 (silver in a silicone binder)	.057	6
Electrodag 106 (graphite in an epoxy binder)	1.17	6
Epoxy	1.7	10, 16
Fluoropolymers:		
FEP Kapton	.03	18
Kapton F	<.05	6
Teflon, FEP	.037	5
Teflon, FEP	<.05	10
Teflon, TFE	<.05	10, 6
Teflon, FEP and TFE	0.0 and 0.2	15, 19
Teflon, FEP and TFE	.1	15
Teflon	.109	18
Teflon	.5	15
Teflon	.03	15
Teflon	<.03	9
Gold (bulk)	0.0	17
Gold	Appears resistant	20
Graphite epoxy:		
1034 C	2.1	10
528/T300	2.6	10
GSFC green	0.0	1
HOS-875 (bare and preox)	0.0	1, 26
Indium Tin oxide	.002	15, 16
Indium Tin oxide/Kapton (aluminized)	.01	2
Iridium film	.0007	17
Lead	0.0	1, 26
Magnesium	0.0	1, 26
Magnesium fluoride on glass	.0007	15, 16
Molybdenum (1000 Å)	.0056	4
Molybdenum (1000 Å)	.006	15, 16
Molybdenum	0.0	1, 26
Mylar	3.4	10
Mylar	2.3	15, 19
Mylar	3.9	15, 19, 9
Mylar	1.5 to 3.9	15
Mylar A	3.7	18
Mylar A	3.4	21, 6
Mylar A	3.6	6
Mylar D	3.0	6
Mylar D	2.9	21
Mylar with Antiox	Heavily attacked	22

Material	Erosion yield, $\times 10^{-24}$ cm^3/atom	Reference
Nichrome (100 Å)	0.0	1
Nickel film	0.0	17
Nickel	0.0	8, 26
Niobium film	0.0	17, 1
Osmium	.026	10
Osmium	Heavily attacked	20
Osmium (bulk)	.314	17
Parylene, 2.5 mm	Eroded away	22
Platinum	0.0	1, 26
Platinum	Appears resistant	20
Platinum film	0.0	17
Polybenzimidazole	1.5	10, 7
Polycarbonate	6.0	8
Polycarbonate resin	2.9	17
Polyester - 7% Poly-silane/93% Polyimide	.6	10
Polyester	Heavily attacked	10, 22
Polyester with Antiox	Heavily attacked	10, 22
Polyester (Pen-2,6)	2.9	23
Polyethylene	3.7	10, 21, 16, 15
Polyethylene	3.3	18, 6
Polyimides:		
BJPIPSX-9	.28	23
BJPIPSX-9	.071	24
BJPIPSX-11	.56	23
BJPIPSX-11	.15	24
BTDA-Benzidene	3.08	23
BTDA-DAF	2.82	23
BTDA-DAF	.08	24
BTDA-mm-DDS02	2.29	23
BTDA-mm-MDA	3.12	23
BTDA-pp-DABP	2.91	23
BTDA-pp-ODA	3.97	23
I-DAB	1.80	23
Kapton (black)	1.4 to 2.2	15, 12
Kapton (TV blanket)	2.0	15
Kapton (TV blanket)	2.04	19
Kapton (OSS - 1 blanket)	2.55	15
Kapton (OSS - 1 blanket)	2.5	15
Kapton H	3.0	10, 15, 19, 4, 6, 9
Kapton H	2.4	15, 19
Kapton H	2.7	15, 18
Kapton H	1.5 to 2.8	15
Kapton H	2.0	18
Kapton H	3.1	18
Kapton (uncoated)	.1 and .06	2
ODPA-mm-DABP	3.53	23
PEN-2.6	2.90	23
PMDA-pp-DABP	3.82	23
PMDA-pp-MDA	3.17	23, 24
PMDA-pp-ODA	4.66	23
Polymethylmethacrylate	3.1	16
7% Polysilane/93% Polyimide	.6	10
25% Polysiloxane, 75% Polyimide	.3	10
25% Polysiloxane	.3	9
Polystyrene-Polyimide	1.7	10, 16, 9
Polysulfone	2.4	10, 16
Polyvinylidene fluoride	0.6	9
Pyrone: PMDA-DAB	2.5	23

Material	Erosion yield, $\times 10^{-24}$ cm^3/atom	Reference
S-13-GLO, white	0.0	12
SiO$_2$ (650 Å) on Kapton H	<.0008	4
SiO$_2$ (650 Å) with ≤4% PTFE	<.0008	4
SiOx/Kapton (aluminized)	.01	2
Silicones:		
DC1-2577	.055	21
DC1-2755-coated Kapton	.05	15
DC1-2775-coated Kapton	<.5	15
DC6-1104	.0515	20
Grease 60 mm	Intact but oxidized	25
RTV-560	.443	21
RTV-615 (black, conductive)	0.0	20
RTV-615 (clear)	.0625	5
RTV-670	0.0	1
RTV-S695	1.48	11
RTV-3145	.128	1
T-650-coated Kapton	<.5	15
Siloxane polyimide (25% Sx)	.3	7
Siloxane polyimide (7% Sx)	.6	7
Silver	10.5	5
Tantalum	Appears resistant	20
Tedlar	3.2	10
Tedlar (clear)	1.3 and 3.2	15
Tedlar (clear)	3.2	18, 6
Tedlar (white)	.4 and .6	15
Tedlar (white	.05	15
TiO$_2$, (1000 Å)	.0067	5
Trophet 30 (bare and preox)	0.0	1, 26
Tungsten	0.0	8, 26
Tungsten carbide	0.0	8
YB-71 (ZOT)	0.0	7
Z302 (glossy black)	3.9	26

SECTION 3

DEVELOPMENT OF NEW BAFFLE MATERIALS

Extensive testing carried out during the first year of the Advanced Baffle Materials Technology Development Program demonstrated that only one commercially available baffle material is close to the optical performance required for functional technical validation (FTV) programs with FY 90-93 launches.* Unfortunately, this material has highly unsatisfactory vibration and x-ray hardness performance. Because of this, FTV programs require new materials which can survive launch vibration, while maintaining their optical performance, without producing particulate debris and system contamination. Moreover, post-FTV programs will require new materials which can survive in the anticipated threat environment.

3.1 STRATEGIES FOR IDENTIFIED IMPROVED BAFFLE MATERIALS

Critical examination of failure mechanisms in current baffle materials has suggested four approaches for producing superior baffle materials and the Advanced Baffle Materials Technology Development Program is pursuing each of these approaches.

- Hard Ceramic Coatings on Textured Substrates

   The highly textured coatings of the best current baffle materials are quite fragile and contribute to system contamination problems. To overcome this problem, one promising approach is to texture the <u>substrate</u> instead of the coating.

- Over-Coating for Existing Baffle Materials

   This approach would develop hard transparent over coatings which will mitigate particulate debris problems in current baffle materials. Both this and the first approach depend on the adhesion of a hard, dark coating to a textured substrate.

- Hard Transparent Coatings Doped with Absorbers

   Flat attenuating coatings doped with absorbers may offer adequate optical absorption properties without intricate surface texture.

- Specular Baffle Materials

---

* Requirements are described in papers by P.L. Jessen, and by J. Wells and C. Martin, in Proc. Nucl. Hard. Sensor Tech. Symp., 20-22 Feb. 1988, Huntsville, AL.

Specular baffle materials or coatings, which are substantially harder and more immune to particle blow-off than textured surfaces, offer promise for the forward-facing sides of baffle vanes in many telescope configurations.

Hard Ceramic Coatings on Textured Metal Substrates - This approach is illustrated in Figure 3-1. It exploits two proven technologies: ion beam texturing of metal substrates and ion beam assisted deposition of hard faced ceramic coatings.

Hard Ceramic Overcoating

Textured Metal Substrate
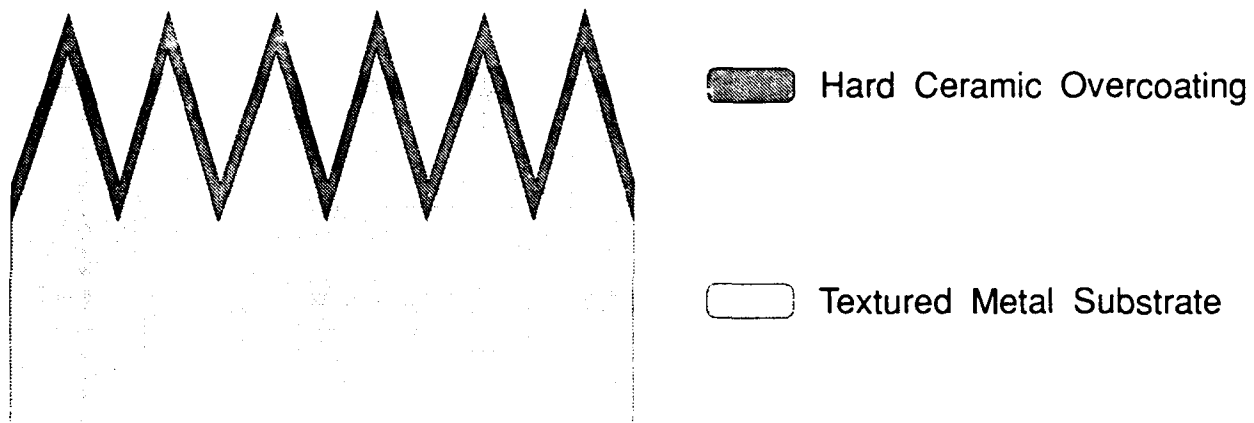
FIGURE 3-1.   HARD CERAMIC COATINGS ON TEXTURED METAL SUBSTRATES.

Advantages

- The texture features are contained in the substrate and not in the coating. These features are tightly bound to the surface.

- The outer coating is a hard and uniform film; this structure is immune to particulate blow-off.

- The optical and radiation resistance properties of this structure may be tuned independently.

Disadvantages

- Unless the substrate and coating are chosen properly, thermal expansion mismatch may still lead to radiation failure at interfaces in this structure.

Status

- Spire has demonstrated ion beam texture-etch technology for graphite, beryllium, aluminum. Spire is the only known source of this technology for metals although one alternate source exists for texturing graphite.

- Plasma and ion beam deposition processes have produced hard ceramic films of diamond-like carbon (DLC), boron carbide (B_4C), silicon carbide (SiC), boron nitride (BN), and silicon nitride (Si_3N_4).

Work Remaining

- Surface texturing technology must be refined in order to reduce required processing times and produce surface structures with lower total hemispherical reflectance. Diamond-like carbon coating technology must be further refined to allow deposition on candidate baffle substrates. Appropriate choice of substrate and coating will reduce thermal expansion mismatch problems, but new technologies such as ion beam mixing and intermediate layer energy-sharing structures may further improve coating adhesion.

Over-coating for Existing Baffle Materials - This approach (Figure 3-2) is perhaps the most straightforward baffle hardening approach.

Hard Ceramic Overcoating

Original Baffle Coating

Metal Substrate

FIGURE 3-2. HARD CERAMIC COATINGS FOR EXISTING BAFFLE MATERIALS.

Advantages

- This approach makes good use of existing baffle technology and of the hard ceramic film technology described above.
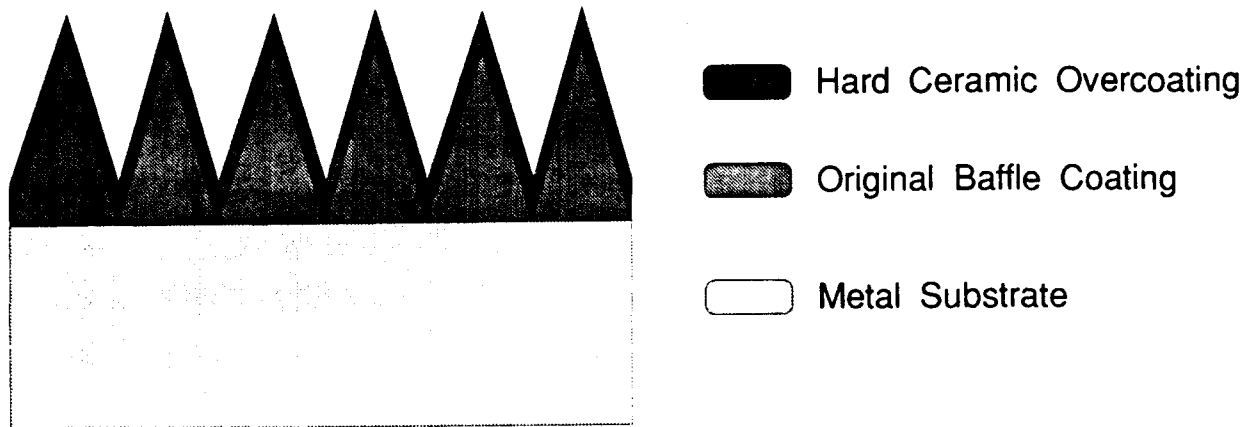
Disadvantages

- Over-coatings do not solve the fundamental problem of current generation baffle materials: adhesion failure between the textured coating and flat substrate. This approach leaves the fragile interface unchanged. In addition, this approach suffers from adhesion problems between the original dark coating and the over-coating.

- Since there are no existing baffle materials which employ radiation proven materials such as beryllium, the ultimate hardness of the flat substrate/textured coating/hard over-coating structure is limited.

Status

- One early attempt to deposit a hard ceramic film on top of an existing baffle material produced a diffuse reflecting surface.

Work Remaining

- Further efforts are in progress at Spire to fabricate extremely thin, uniform over-coatings to overcome this problem. The technology required to implement this approach is substantially the same as the technology to implement the first hardening approach. However, current baffle coatings are insulating and highly textured; they contain large numbers of micron scale particles. Ion beam mixing and other techniques will be required to improve the adhesion hard face coatings to these "difficult" substrates.

Hard Transparent Coating Doped with Absorbers - This approach (Figure 3-3) exploits existing absorber technology, developed for low observable programs throughout the Department of Defense.

Advantages

- This approach allows optical properties to be tuned easily by changing absorber size, shape, and composition.

- This approach has substantial promise for scale-up since many of the hard ceramic coatings can be deposited by inexpensive large-scale processes such as spray-pyrolysis.

Ceramic Coating Doped with Absorbers

Metal Substrate
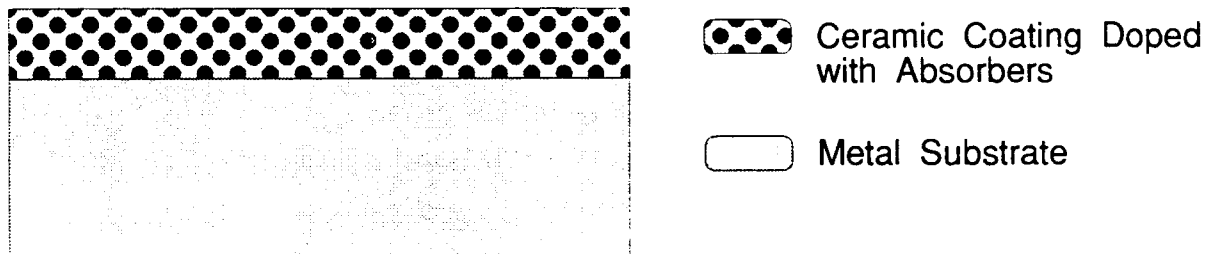
FIGURE 3-3.   HARD TRANSPARENT COATINGS DOPED WITH ABSORBERS.

Disadvantages

- This approach has the problem of high reflectivity at the [flat] front face of the hard ceramic coating.

- Radiation test results on composite materials indicate a substantial concern over thermal expansion mismatch between the absorber particles and the ceramic matrix.

- These structures are best suited for narrow-band absorption applications.

Status

- A first-glance experiment, to evaluate the feasibility of this approach, has been conducted. (The results of this experiment were reported in detail in Spire report MR-10106-09) Absorbing particles (Vulcan CX-72) were dissolved in an organic binder and painted onto graphite felt. The resulting coating was substantially darker than existing organic baffle coatings.

Work Remaining

- Technology must be developed for incorporating these absorbing particles into hard ceramic films without changing the desirable mechanical properties of the films.

Specular Baffle Materials - The most aggressive solution to the baffle materials problem is the use of specular baffle materials, which reflect much of the incident in-band radiation (Figure 3-4).

Hard Ceramic Coating
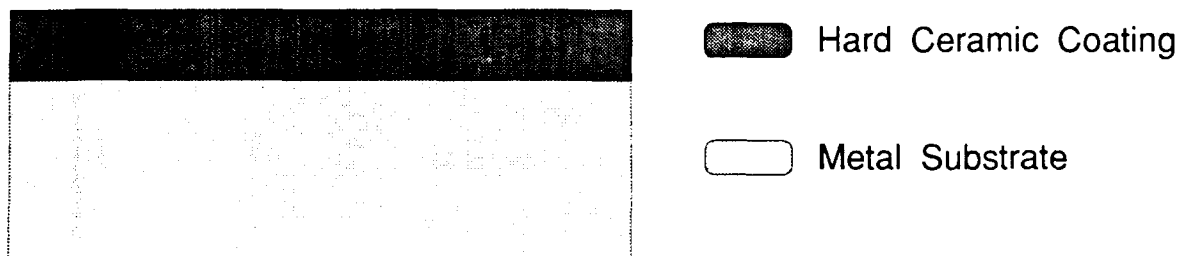
Metal Substrate

FIGURE 3-4.   SPECULAR BAFFLES.

Advantages

- Uniform films are immune to blow-off and contamination problems.

- Hard black specular coatings are applied to a flat metal substrate. These structures are particularly easy to fabricate and manufacture.

- This approach exploits rad-hard beryllium materials which have been developed for a number of aerospace and optical applications.

- This approach may offer significant advantages to the system designer because the specular baffle surfaces reject some of the ambient thermal load from sunlight and other sources. This will help to lower system operating temperatures and reduce thermal noise.

Disadvantages

- Optical design technology for specular baffles remains un-proven in actual telescope systems. The incorporation of specular baffles in place of diffuse absorbing baffles may impose other constraints on the optical train design and will typically require some optical re-design.

Status

- The Army baffle program has developed several processes for fabricating BeO/Be structures which are extremely hard and resistant to mechanical and radiation shock. Similar materials have been produced by other suppliers in the past; none are currently in production.

Work Remaining

- The Breault Research Organization (BRO) is conducting small-scale calculations on optical design modifications (for generic telescope systems) required to accommodate specular baffle materials.

3.2 DEVELOPMENT OF IMPROVED BAFFLE MATERIALS

Because of the apparent failure of all commercially available baffle materials to meet requirements for advanced sensor systems, baffle materials development work began well ahead of the contract schedule. Each of the hardening approaches were investigated, but early development work demonstrated that textured metal substrates had a high probability of success. This section describes progress on the development of this approach and the required materials technologies.

Current commercially available baffle materials shed dangerous levels of particulate debris in vibration tests and in pulsed irradiation tests. Careful examination of the test results has revealed that the dominant failure mechanism in these materials is microscopic fracture at the base of surface texture features. In conventional materials, these features are contained in an oxide layer and the materials suffer from thermal expansion mismatch and acoustic impedance mismatch at small, fragile interfaces between surface oxide and metal substrate. To overcome this problem, Spire has used ion beam texturing technology to produce intricate texture directly on metal surfaces without introducing the fragile interfaces which characterize conventional materials.

Typical ion beam currents for this process are on the order of several mA and typical processing times are 2-8 hours. This produces surface texture feature densities of 0.5-2.0 features per micron. The seed metal, substrate temperature, process gas, ion beam energy, and residual gas pressure govern the size, shape, and density of surface features which can be formed.

This program has developed the use of ion beams to create random microscopic textures on metal surfaces, ranging in size from less than 0.1 to several μm. Driven by the need to develop rugged, broad band light-absorbers for missile guidance, we developed processes to produce a random mixture of larger and smaller features on metal surfaces. Multiple scattering from different size features makes these surfaces relatively broadband absorbers that appear black in the visible and well into the infrared. Figure 3-5 shows typical ion beam textured surfaces: Figure 3-6 shows measured reflectivities.
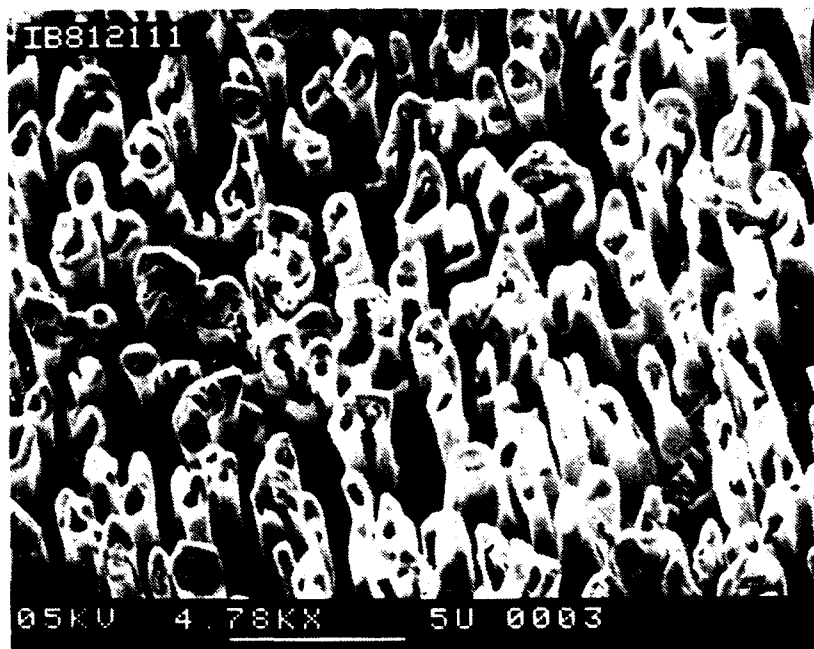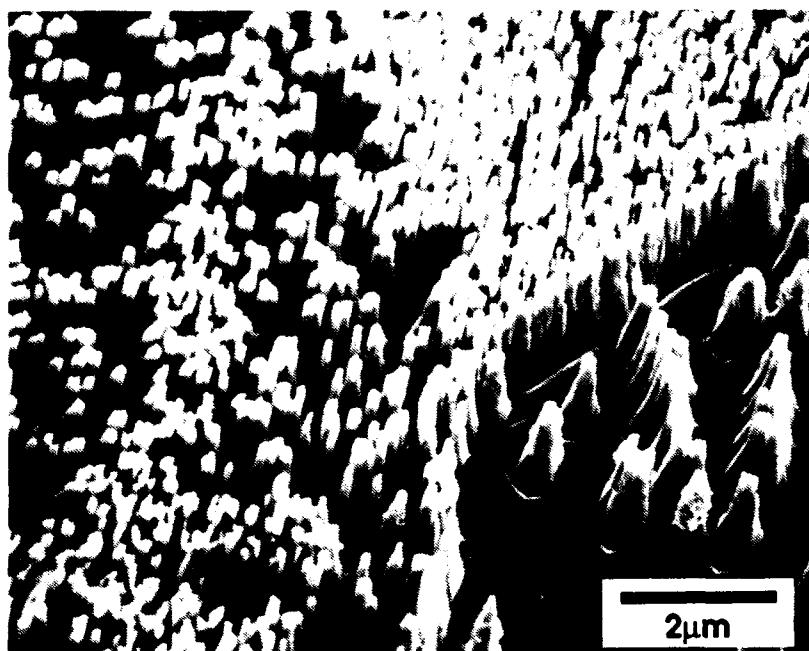
FIGURE 3-5. ION BEAM TEXTURED SURFACES: (A) ALUMINUM AND (B) COPPER.

Ref File: B:B10377-1.REF   02-07-1992 14:56:14
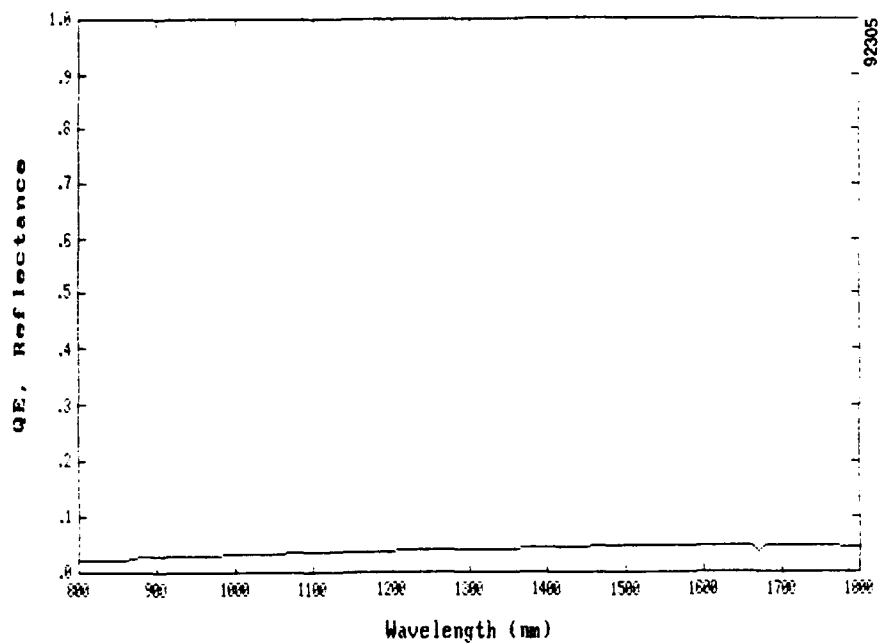
%Transmittance_

OPERATOR: NONAME
SAMPLE: B10377
FORM: IBT AL 3HR 450C
SCANS: 32   RESOLUTION: 4 cm -1   DATE: 1/28/92

%T	A	K-M	WLWN	ASCALE	OVERLY	WINDOW	NOTE	FLIP	GRID
F1	F2	F3	F4	F5	F6	F7	F8	F9	F10

FIGURE 3-6.   MEASURED HEMISPHERICAL REFLECTANCE FOR ION BEAM TEX-
                TURED ALUMINUM SAMPLES.

Ion beam texturing was first described in 1942, before it could be imaged by electron microscopy, based on angular changes in reflectivity of glow-discharge cathodes.[19] Since then, many researchers have studied the ion texturing processes and the physical mechanisms involved have become relatively clear.[20]

Energetic (keV) ions striking a solid surface collide with target atoms and transfer enough kinetic energy to break atomic bonds in the outer surface layers so that surface atoms are sputtered away. Efficiency of the sputtering process depends mostly on kinematic factors, specifically mass and energy of projectile ions and mass of target atoms. Typically, heavier projectile ions sputter more efficiently, and lighter target atoms are removed more easily than heavy atoms. However, target atoms which form strong chemical bonds to their nearest neighbor atoms are more difficult to remove. For each projectile ion/target atom combination, there is an optimum sputtering energy related to the relative speed of the ion and of binding electrons in the solid.

Components of mixed target materials usually sputter at different rates, as do impurities. If sputtering removes an impurity more slowly, islands of this species may shield the underlying target material from sputter erosion and produce pillars on the resulting surface. This natural texture has been observed in many classes of materials: metals, ceramics, and polymers.[21] Similarly, artificially deposited "seed" impurities can enhance this texture. If impurities are not randomly deposited but deliberately placed in regular patterns, this effect may intensify for surface texture lithography.[22]

Other researchers have reported that, for natural texturing, surface temperature governs the size of the texture features formed, apparently through diffusion of impurities away from islands.[23] We have experimentally confirmed this effect and a similar temperature effect for different impurity seed atoms. Residual gasses in the vacuum chamber during ion bombardment also appear to affect feature size.[24] These and other parameters can now enable a deliberate control of feature sizes. Much of the development work in this program was directed at combining a range of feature sizes to broaden the absorption band.

The two boundaries of the apparent absorption (or emission) band include a coherent scattering or long wavelength side and an incoherent or short wavelength side dominated by geometrical optics.[25] The coherent or long wavelength side is typically the steepest (Figure 3-7, after reference 25) due to rapid extinction for coherence as features (or their spacing) become larger than $\lambda/2\pi$. Engineering a process to produce the appropriate surface feature density produced surfaces which were relatively dark over a wide waveband.

Spire uses ion beam sputter etching to produce surface microtexture on samples of aluminum (see Figure 3-5). Current theory predicts that sputter texture etching works because residual gases combine with the seed material to form carbide/oxide islands on the surface of the substrate. These islands have lower sputter yield rates than the substrate.
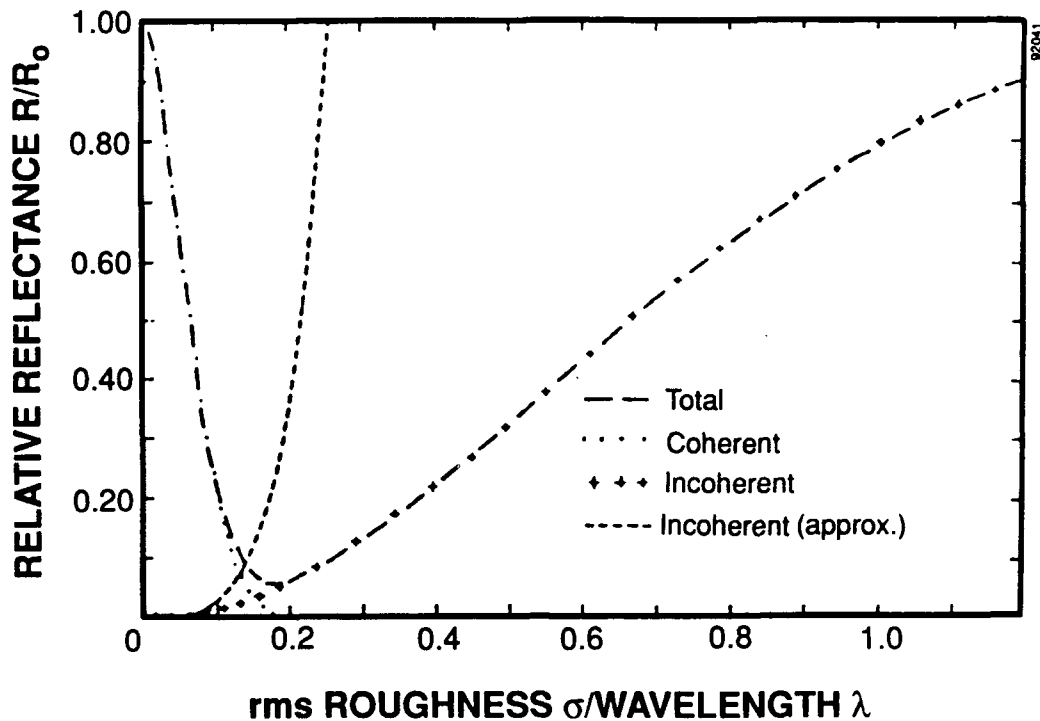
FIGURE 3-7. THEORETICAL SCATTERING FOR A SINGLE-PEAKED GAUSSIAN DIS-TRIBUTION OF FEATURE SIZES.

This yield differential causes features to grow as the surface is sputtered away. The process parameters which control feature growth are:

- Beam Energy
- Process Time
- Sample Temperature
- Ion Species
- Residual Chamber Gases

By creating a multi-dimensional test matrix, these parameters were thoroughly tested for their effects on reflectivity and hardness in order to create the optimal process for reducing reflectivity. A fully factorial experiment was designed and conducted to jointly optimize all five process variables in only 42 process cycles. This experiment design, coupled with tight feedback from sample testing, is responsible for the dramatic improvements in the optical performance and mechanical hardness of textured metal coupons achieved during this program.

During the course of the program, Spire made enormous advances in reducing the reflectivity of textured aluminum. As can be seen in Figure 3-8, the reflectivity of textured aluminum has been reduced from 11% in November 1988 to 1% reflective sample, produced by Spire's SPI-TEXT™ 13-73 AE process, is durable and can withstand normal laboratory handling without damage to its optical properties (see Figure 3-9).
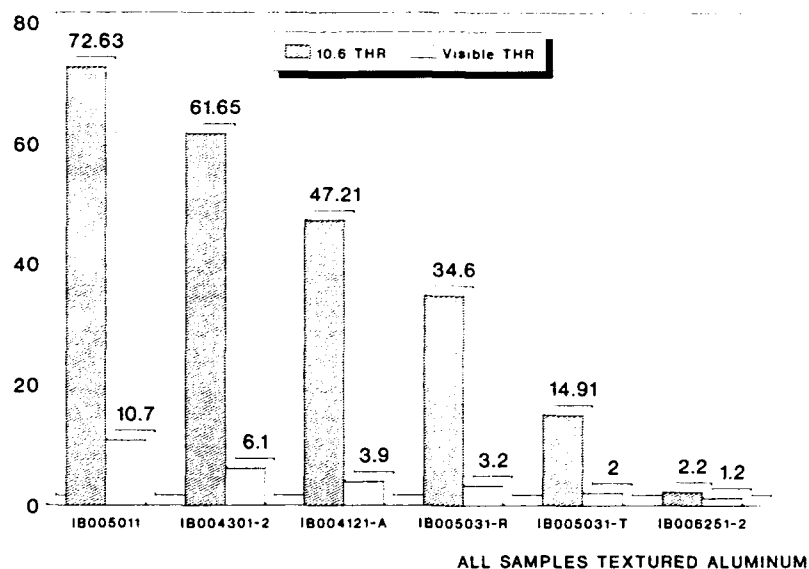
FIGURE 3-8.   PROGRESS MADE IN REDUCING THE REFLECTIVITY OF TEXTURED
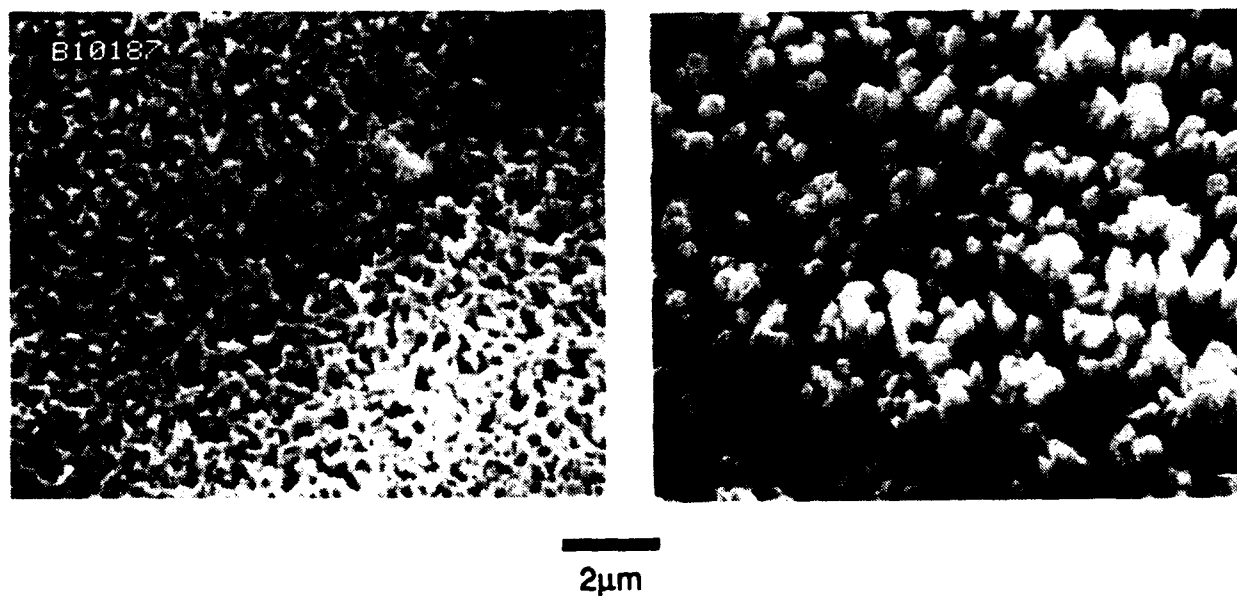ALUMINUM.

FIGURE 3-9   SEM PHOTOS ILLUSTRATE CONTROL OF SURFACE FEATURE SIZE.

This program demonstrated that ion beam texturing technology can produce extremely dark surfaces which are immune to damage from ordinary handling. This technology is particularly promising because it allows control over the size of surface texture features and hence the optical wavelength at which the surface absorbs. Development work during this program has produced dramatic improvements in the reflectance (~ 1%) of ion beam textured aluminum without comprising mechanical hardness. In simulated launch vibration tests, this material produced no detectable contamination on adjacent catcher plates. Ion beam textured metals offer a technological breakthrough for meeting the stray light suppression needs of advanced sensor systems.

3.3   TEST RESULTS ON TEXTURED METAL SAMPLES

As part of an effort to support the Strategic Defense Command's survivable optics community, Spire produced over fifty samples for the Mineral Quarry above ground test (AGT) and underground test (UGT) sequence.

One of the most important and useful features of this technology is the control it offers over surface feature size and, therefore, over the absorption band of the surface. As illustrated in Figure 3-9, process parameters during ion beam texturing can vary the surface feature size by well over an order of magnitude. By exploiting this flexibility, this program has demonstrated textured metal surfaces which are extremely dark in the visible, other surfaces which are extremely dark in the infrared, and still other surfaces with broad-band absorption. Figure 3-10 shows the distribution of scattered light as a function of angle, (BRDF) measured both in the visible and the infrared, for these surfaces.

Shock and vibration tests on coupon size samples of textured aluminum and textured beryllium were performed by Kaman Sciences Corporation for the U.S. Army Strategic Defense Command preparation for the Mineral Quarry underground test. The coupons were glued into a small test cassette adjacent to clean catcher plates. The entire assembly was then shaken to an "ERIS" launch vibration spectrum. After the test, the catcher plates were removed and debris particulates were counted under an optical microscope at Kaman Sciences and then recounted in an electron microscope at Oak Ridge National Laboratory. Figure 3-11 shows the particulates larger than 5 μm diameter counted on catcher plates for a number of samples. Notice that in each case the catcher plates adjacent to textured metal samples contained numbers of particles at or below the background level. This is not surprising since, as noted earlier, the textured metal materials are quite sturdy and are not damaged by routine laboratory handling.

3.4   METAL TEXTURING SPIN-OFF TECHNOLOGY

With the U.S. Army Materials Technology Laboratory, Spire has pursued a vigorous program to advance the state of the art for optical baffle materials. The Key Technologies division of the U.S. Army Strategic Defense Command has supported this work because optical baffles are vital to strategic defense sensor systems. To meet the baffle eeds of advanced sensor systems, Spire has developed SPI-TEXT™ metal texturing technology to produce surfaces which are mechanically sound and optically dark. This technology creates intricate micron-scale texture features on metal surfaces with a dramatic increase in surface area.
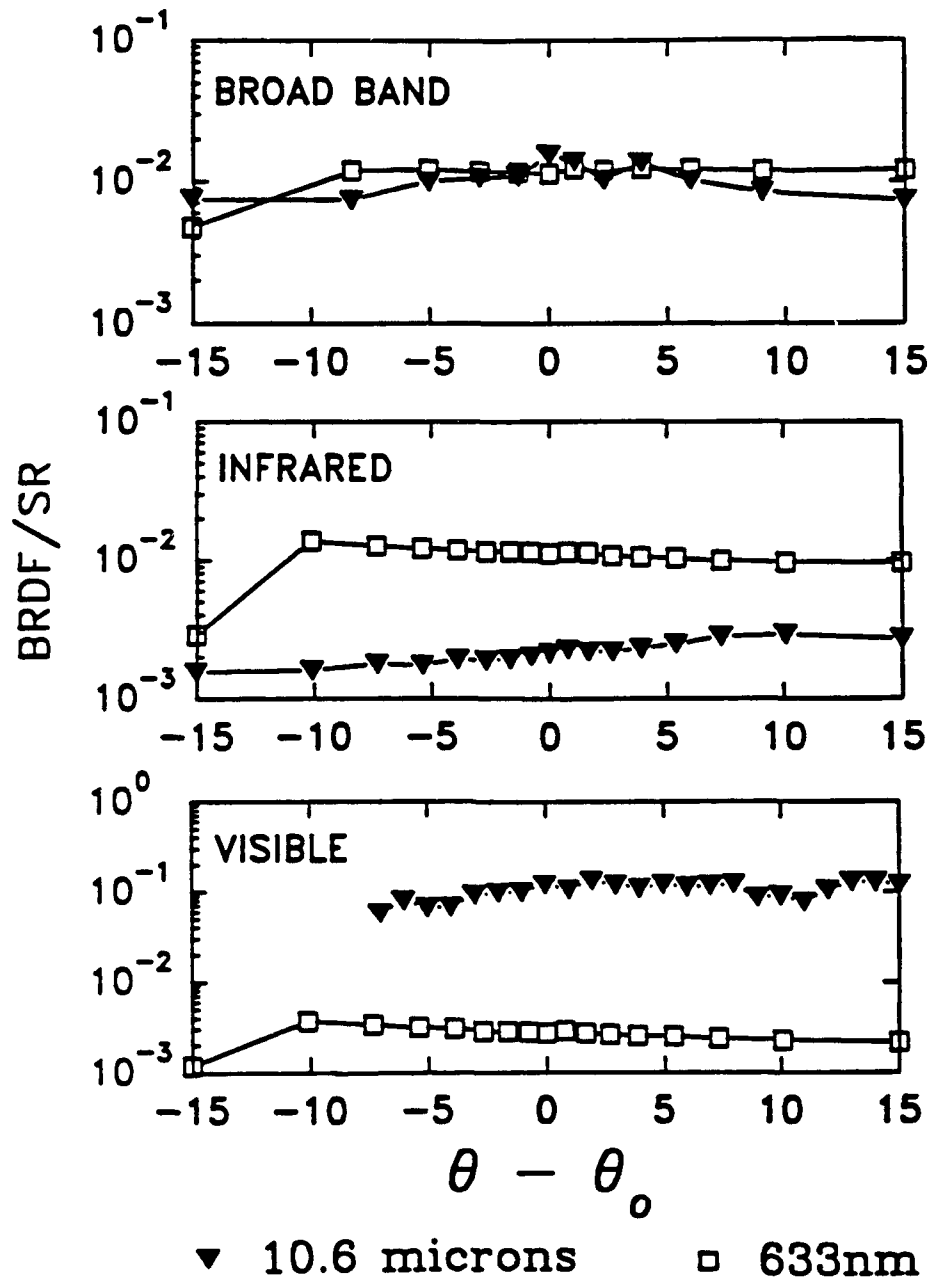
FIGURE 3-10.   SCATTERED LIGHT PERFORMANCE OF ION BEAM TEXTURED
ALUMINUM SURFACES OPTIMIZED FOR ABSORPTION IN THE
VISIBLE AND INFRARED. By processing in different stages and changing
process conditions, it is possible to produce surfaces which absorb over a very
wide waveband.

3 - 14
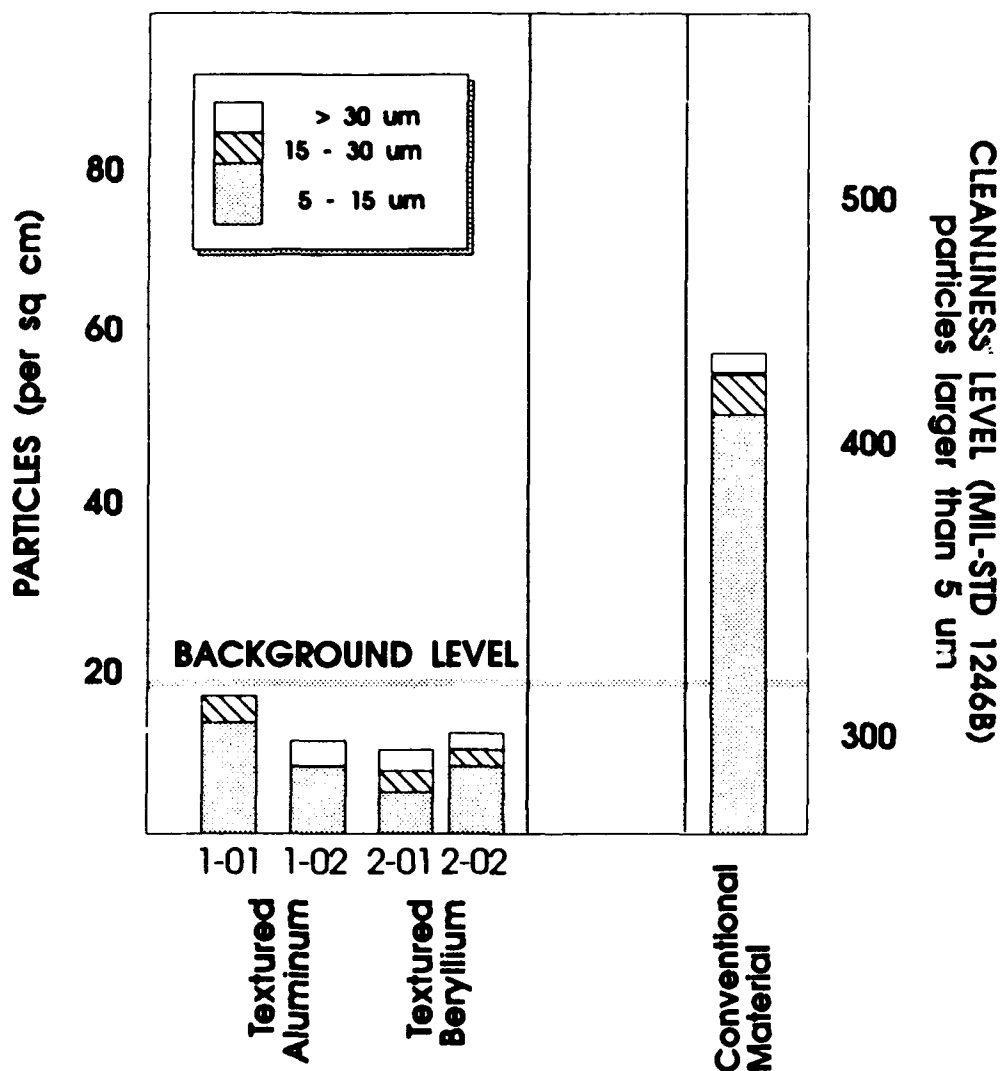
FIGURE 3-11. RESULTS OF MINERAL QUARRY AGT VIBRATION TESTS ON DEVEL-
OPMENTAL BAFFLE MATERIAL COUPONS.

The high surface area of SPI-TEXT™ has led to an important technology spin-off. The performance and service life of implanted cardiac pacemakers is limited by the size and storage of battery cells which power the devices. For conventional pacemaker electrodes, much of the battery's stored charge is spent overcoming contact resistance between the electrode tip and the muscle fibre. Spire has applied the SPI-TEXT™ process to increase the surface area of cardiac pacemaker electrode tips (Figure 3-12) with accompanying improvement in tissue attachment and preliminary in-vivo studies have demonstrated sharp improvements in device performance and battery lifetime for devices treated with SPI-TEXT™. This technical achievement represents an important example of strategic defense technology at work in other fields.

3 - 15

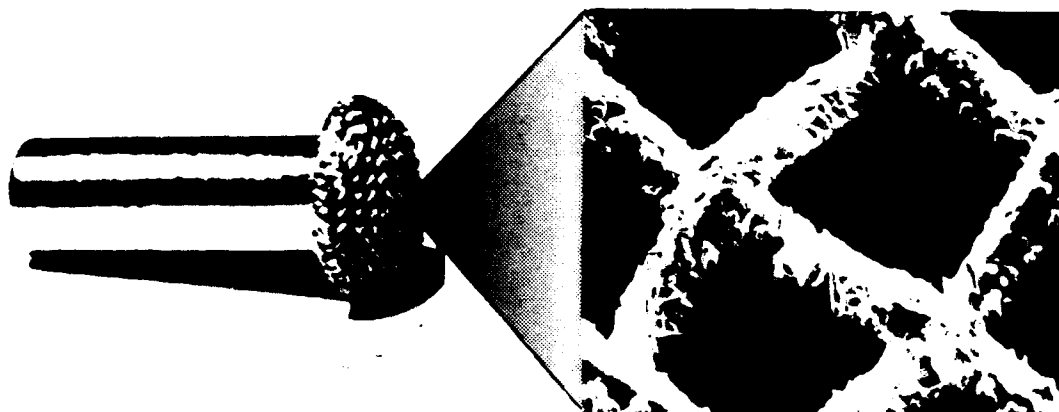FIGURE 3-12.   PHOTOGRAPH OF SPI-TEXT TREATED CARDIAC PACEMAKER
                 ELECTRODE TEXTURING PRODUCES A DRAMTATIC DECREASE
                 IN CONTACT RESISTANCE.

3.5   STATUS AND CONCLUSIONS

Optical sensors comprise an important part of the SDS Phase I architecture. The mission of these sensors requires extreme sensitivity and discrimination. These sensor systems will require optical baffles in order to achieve adequate off-axis stray light rejection and pointing accuracy. To perform their primary mission of rejecting in-band stray light, baffle materials must maintain their optical performance after exposure to both operational and threat environments. In addition, baffle materials must not introduce contamination which would compromise the system signal-to-noise performance and impair the mission readiness of the sensor system.

This program has demonstrated that ion beam texturing technology can produce extremely dark surfaces which are immune to damage from ordinary handling. This technology is particularly promising because it allows control over the size of surface texture features and hence the optical wavelength at which the surface absorbs. Development work during this program has produced dramatic improvements in the reflectance ($\approx 1\%$) of ion beam textured aluminum without compromising mechanical hardness. In simulated launch vibration tests, this material produced no detectable contamination on adjacent catcher plates. Ion beam textured metals offer a technological breakthrough for meeting the stray light suppression needs of advanced sensor systems.

3 - 16

SECTION 4

CONCLUSIONS

The Spire/MTL program for Advanced Baffle Materials Technology Development has produced a critical examination of the optical performance, flight-worthiness, and radiation hardness of current commercially available baffle materials. Of more than fifty materials tested, only a few met optical performance specifications typical of advanced strategic defense sensor systems, and none of the optically qualified materials survived simulated launch and flight vibration. Because of this, Functional Technology Validation (FTV) missions with imminent launch dates have an urgent need for improved baffle materials which are optically dark and mechanically hard. Tactical missions, with somewhat later launch dates, have additional requirements for materials capable of performing their mission in a threat environment.

Careful study of results from testing of current baffle materials has produced a detailed understanding of the fundamental failure mechanisms in these materials. This understanding, in turn, has enabled rapid identification and optimization of processes for producing coupons of superior baffle materials. Spire relies exclusively on processes which are flexible and which allow tailoring of optical properties, mechanical properties, and radiation hardness. Aluminum has been chosen as the vehicle for this process technology development during the initial stages of the program, but Spire has demonstrated that the process for aluminum may be easily transferred to beryllium to form more radiation tolerant baffle materials.

Tight feedback between coupon fabrication and coupon testing coupled with the choice of aluminum as a means of leveraging ion texturing technology to beryllium, promoted this rapid development and allowed these remarkable achievements.

To employ textured metal materials in sensor systems, Spire plans to build on achievements in developing advanced baffle material coupons. Three essential features of this plan are evident in this report:

- Leverage technology developed in coupon-scale work to date
- Identify and meet the baffle needs of sensor project offices
- Maintain close integration between material fabrication and testing

By adhering to these basic principles, Spire and the U.S. Army Materials Technology Laboratory will produce baffle structures and assemblies, quickly and cost-effectively, to meet the needs of strategic defense sensor systems.

SECTION 5

REFERENCES

1. C.L. Hanks and D.J. Hamman, Radiation Effects Information Center, Battelle Memorial Institute, REIC Report No. 46, (June 1969).

2. B. Gross, J. Dow, and S.V. Nablo, J. Appl. Phys. $\underline{44}$, 2459 (1973).

3. G.A. Vorob' ev and V.S. Korolev, Sov. Phys. Tech. Phys. $\underline{21}$, 1222 (1976).

4. J.P. Brainard and D. Jensen, J. Appl. Phys.45, 3260 (1974).

5. A.S. Denholm et al, U.S. Air Force Weapons Laboratory Technical Report, AFWL-TR-72-88 and the wealth of references contained therein.

6. A.R. Frederickson, IEEE Trans. Nucl. Sci., NS-24, 2532 (1977).

7. R.H. Bartlett, G.A. Fulk, R.S. lee, and R.C. Weingart, IEEE Trans. Nucl. Sci., NS-22, 2273 (1975).

8. R.E. Leadon, C.E. Mallon, and B.A. Green, IEEE Trans. Nucl. Sci. NS-20, 126 (1973).

9. Sandia Corp., ELTRAN, One-Dimensional Monte Carlo Electron Transport Code, SC-TM-68-713. RSIC program number CCC-155.

10. J.C. Ashley, C.J. Tung, and R.H. Ritchie, IEEE Trans. Nucl. Sci. NS-22, 2533 (1975).

11. J.B. Cladis, G.T. Davidson, and L.L. Newkirk, editors, The Trapped Radiation Handbook, Report no. DNA 2524H, Defense Nuclear Agency, Washington DC, 1971 (Revised 1977).

12. L.J. Leg, "Oxygen Atom Reaction with Shuttle Materials at Orbital Altitudes," NASA-TM-58246, NASA Johnson Space Center, Houston, TX, 1982.

13. J.T. Visentine, L.J. Leger, J.F. Kuminecz, and I.K. Spiker, "STS-8 Atomic Oxygen Effects Experiment," AIAA Paper 85-0415, Presented at AIAA 23rd Aerospace Sciences Meeting, January 1985, Reno Nevada.

14. R. Hansen, J. Pascale, T. DeBenedictis, and P. Rentzepis, "Effects of Atomic Oxygen on Polymers," J. Polymer Sci. $\underline{3A}$, 2205 (1965).

15. D.C. Ferguson, "Laboratory Degradation of Kapton in Low Energy Oxygen Ion Beam," NASA-TM-83530, NASA Lewis Research Center, Cleveland, OH 1984.

16. L.J. Leger, J.T. Visentine, and J.A. Schliesing, "A Consideration of Atomic Oxygen Interactions with Space Station," AIAA Paper 85-0476 Presented at AIAA 23rd Aerospace Sciences Meeting, January 1985, Reno, Nevada.

17. Bruce A. Banks, Sharon K. Rutledge, Phillip E. Paulsen, Thomas, J. Streuber, "Simulation of the Low Earth Orbital Atomic Oxygen Interaction with Materials by Means of an Oxygen Ion Beam," NASA Technical Memorandum 101971.

18. J.B. Cladis, G.T. Davidson, and L.L. Newkirk, editors, The Trapped Radiation Handbook, Report No. DNA 2524H, Defense Nuclear Agency, Washington, DC, 1971 (Revised 1977).

19. A. Guentherschultze and W. Tollmien, Z. Physik, 119, 685 (1942).

20. O. Auciello and R. Kelly, Ion Bombardment Modifications of Surfaces: Fundamentals and Applications, Elsevier, NY, 1984.

21. O. Auciello, "Ion Interaction with Solids," and "Surface Texturing, Some Bulk Effects and their Possible Applications," J. Vac. Sci. Technol. 19, (No.4), (1981).

22. W.D. Deininger and S.B. Gabriel, "Mandrels for Microtextured Small-Vessel Implants," NASA Tech. Brief, 13, No. 3, Item #142, (1989).

23. S.M. Rossnagel and R.S. Robinson, "Surface Diffusion Activation Energy Determination Using Ion Beam Micro-texturing," J. Vac. Sci. Technol. 20, (No. 2), 195-8 (1982).

24. C.J. Von Benken and E.A. Johnson, "Role of Impurities in the Growth of Surface Features Due to Ion Beam Bombardment," Unpublished, (1989).

25. J.O. Porteus, "Relation Between the Height Distribution of a Rough Surface and the Reflectance at Normal Incidence," J. Opt. Soc. Am 53, 1394 (1963).

APPENDIX A

OPTICAL PERFORMANCE OF CURRENT

BAFFLE MATERIALS

A.1 TOTAL HEMISPHERICAL REFLECTANCE MEASUREMENTS

Preliminary reflectance measurements in the visible and near infrared bands were performed on baffle materials using a Xenon arc lamp, monochromator, and integrating sphere. The set-up is pictured in Figure 2-1. Light from the arc lamp was focused onto the entrance slits of the monochromator; output of the monochromator was then collimated and focused onto the sample by a pair of lenses. The integrating sphere collected all forward scattering light, allowing the detector to measure reflectance.

Reflectivity was obtained by measuring a calibrated standard, then the sample. The wavelength region measured to date extends from 400 to 1200 microns. Representative reflectivity data is shown in Figure A-1. The slight indentation at 850 nanometers exhibited by all of the samples, is an artifact of the system.
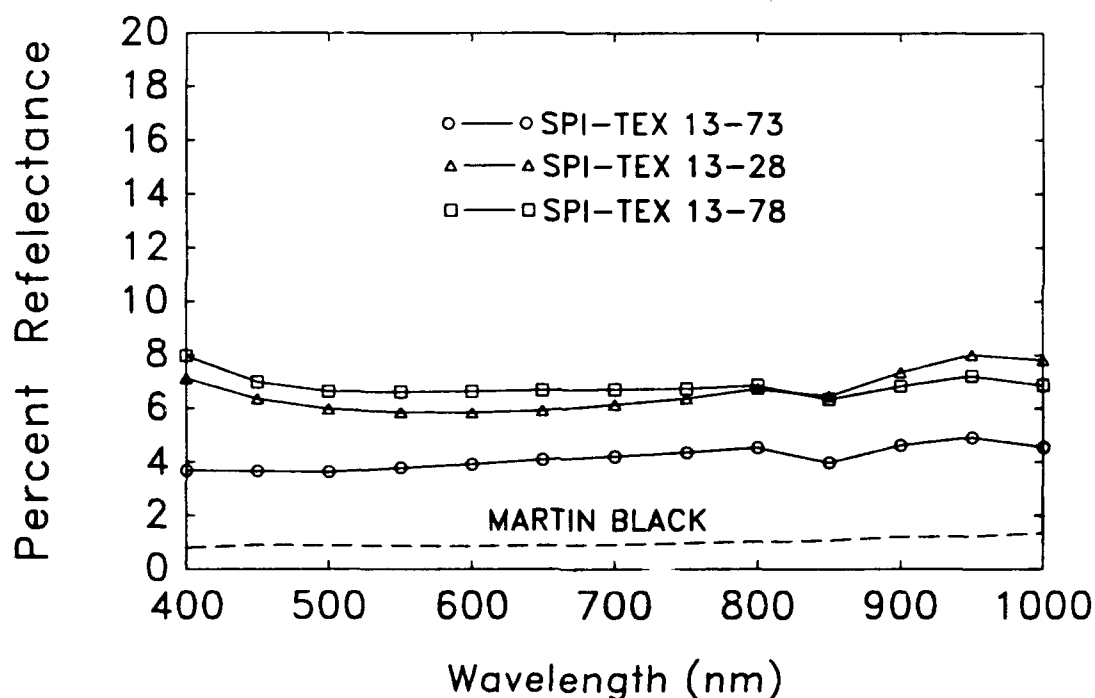

FIGURE A-1.   TOTAL HEMISPHERICAL REFLECTANCE THROUGH THE VISIBLE BAND FOR REPRESENTATIVE BAFFLE MATERIALS.

In addition to the xenon arc lamp, two IR lasers were used to measure baffle optical performance. A 10.6 micron carbon dioxide laser and a 3.39 micron He:Ne laser were used to determine near and mid IR performance. Results for the 20 blackest materials are summarized in Figure A-2.
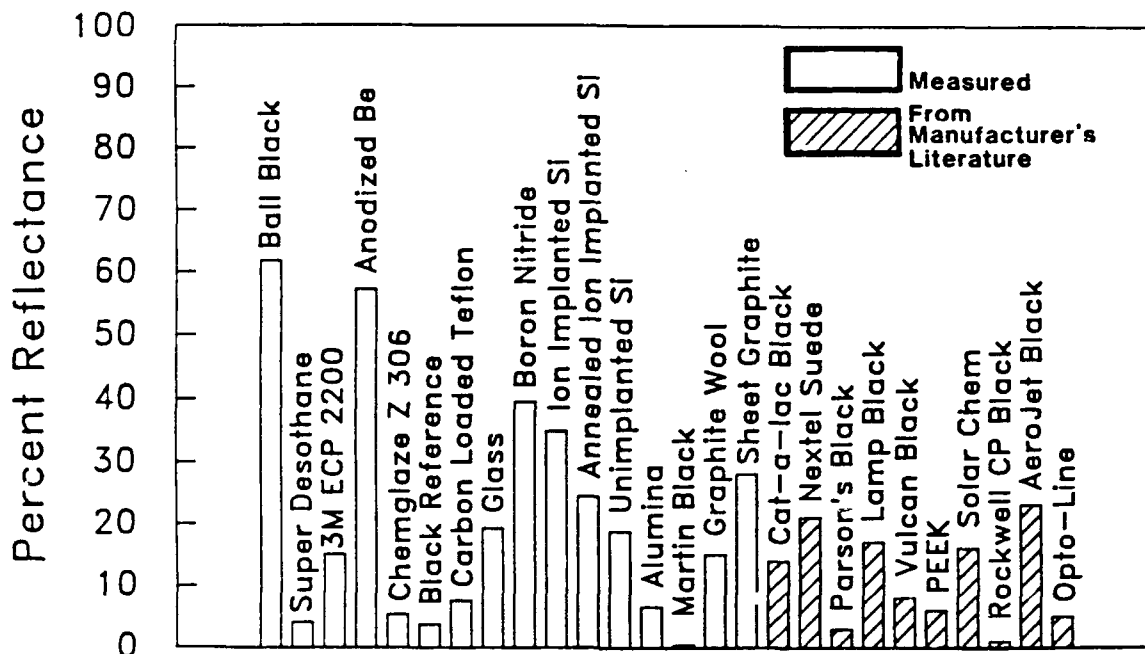
A - 1

Percent Reflectance

100
90
80
70
60
50
40
30
20
10
0

Measured
From Manufacturer's Literature

Ball Black
Super Desothane
3M ECP 2200
Anodized Be
Chemglaze Z 306
Black Reference
Carbon Loaded Teflon
Glass
Boron Nitride
Ion Implanted SI
Annealed Ion Implanted SI
Unimplanted SI
Alumina
Martin Black
Graphite Wool
Sheet Graphite
Cat-a-lac Black
Nextel Suede
Parsor's Black
Lamp Black
Vulcan Black
PEEK
Solar Chem
Rockwell CP Black
AeroJet Black
Opto-Line

FIGURE A-2.   TOTAL HEMISPHERICAL REFLECTANCE DATA FOR BAFFLE MATE-
RIALS AT 10.6 µm. Notice that the shaded measurements are from manu-
facturers' literature and have not been independently confirmed.

Data for sheet graphite and graphite wool demonstrate the dependence of reflectivity on surface structure, sheet being relatively smooth and wool very "rough"; reflectivity of sheet graphite was roughly double that of the wool at both wavelengths.

Many hard anodized aluminum finishes are commercially available; the one evaluated here was part of a Newport Corporation (Fountain Valley, California) "low luster" optical mount. Its reflectivity was 11.6 percent at 3.39 microns and 3.4 percent at 10.6. Comparison of these figures with characteristics of Martin Black, produced in an anodization process which also results in a textured surface, show that the optical benefit obtained by texturing is a twofold reduction in reflectivity at 3.39 microns, and a seven-fold reduction at 10.6.

Figure A-3 shows the total hemispherical reflectance recorded through the visible band for Martin Black and Ball Black baffle materials after irradiation to an electron energy fluence of 0.6 cal/cm^2. Both irradiations were performed with 60 nsec electron pulses of 30 keV mean energy in the SPI-PULSE 300 electron accelerator (Section 2.2.2).

BEFORE and AFTER 0.6 cal/cm^2 IRRADIATION
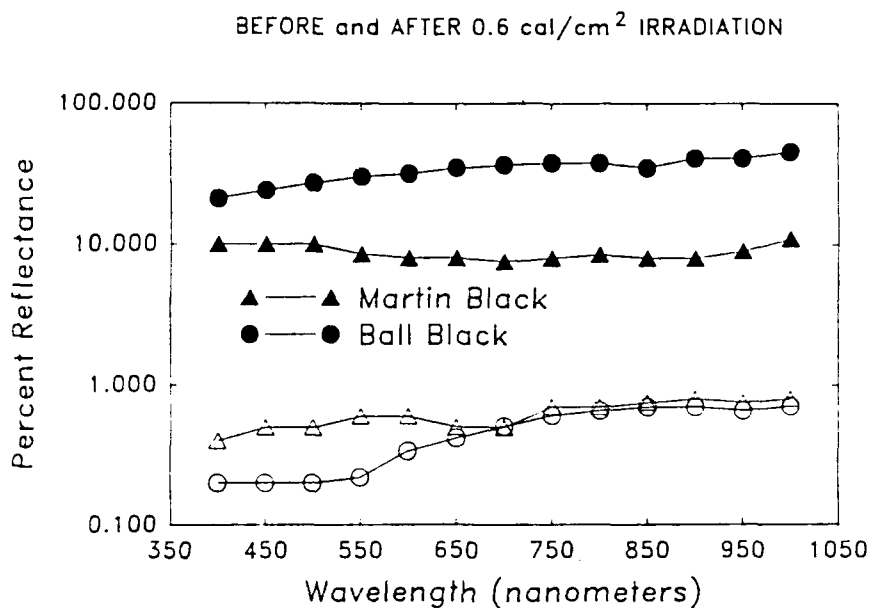
FIGURE A-3. TOTAL HEMISPHERICAL REFLECTANCE FOR MARTIN BLACK AND BALL BLACK BEFORE AND AFTER ELECTRON BEAM IRRADIATION. Note the log scale on the y axis.

The second step in optical screening of baffle materials is the measurement of a scattered light profile, or BRDF. This consisted of visible (633 nm) BRDF on virgin and irradiated baffle material samples. Later, the BRO scatterometer was used to measure the optical performance at 10.6 microns of baffle materials. Results are shown in Figures A-4 and A-5. From these plots, it is evident that pulsed electron irradiation converts the Martin Black and Ball Black materials from diffuse absorbers into weak specular reflectors. As an example of the data generated during this study, we present the 10.6-micron measurement for Martin Black, the hardest and least reflective material tested.
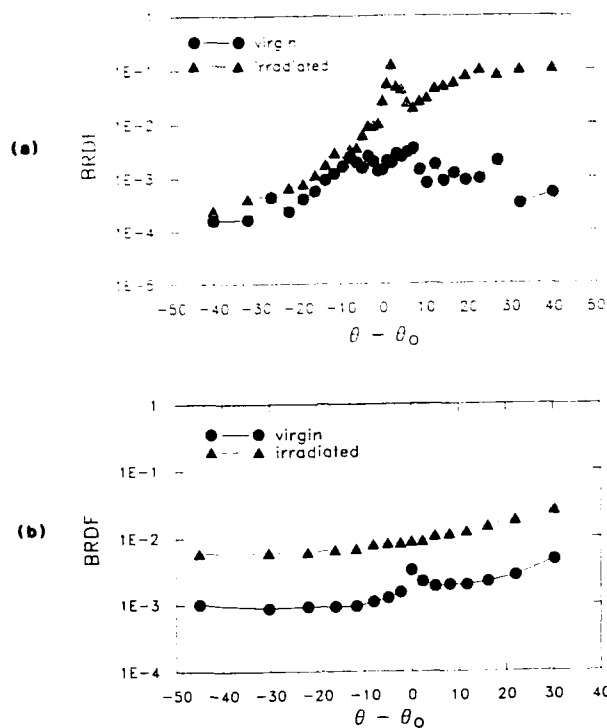
A - 3

FIGURE A-4. BRDF OF MARTIN BLACK BEFORE AND AFTER 0.6 cal/cm^2 ELEC-
TRON IRRADIATION. a) Measurement was made on the BRO FASCAT
instrument at a wavelength of 10.6 microns. b) Measurement was made on
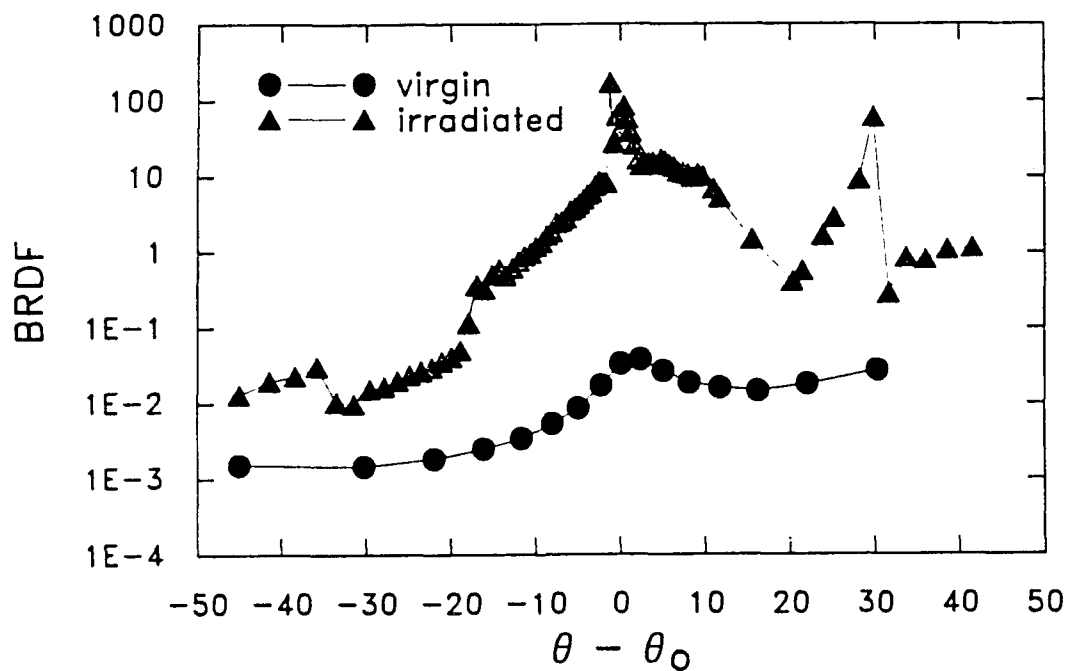the BRO FASCAT instrument at a wavelength of 633 nm.

FIGURE A-5. BRDF OF BALL BLACK BEFORE AND AFTER 0.6 cal/cm^2 ELECTRON
IRRADIATION. Measurement was made on the BRO FASCAT instrument
at a wavelength of 633 nm.

APPENDIX B

RADIATION TESTING OF CURRENT

BAFFLE MATERIALS

B.1 DELAMINATION AND COATING REMOVAL MEASUREMENTS

Because of their intricate textured structure, baffle materials are vulnerable to radiation damage at relatively modest energy fluences. Threshold fluences for optical damage in these materials can only be established in terms of specific damage mechanisms, and these mechanisms are not well understood. Several phenomena are reported in the literature at fairly low energy fluences. Brittle materials chip and crack because of the rapid thermal stresses, and coatings delaminate because of thermal mismatch at substrate interfaces. In addition, particle blow-off from baffle surfaces can foul nearby mirrors and other optical components, while melt and glassy phase formation may increase reflectivity so that the baffles are unserviceable as diffuse absorbers.

A "first look" irradiation test was performed on baffle material coupons in the Spire E-Beam/LWIR Scatterometer mirror testing facility. Prior to irradiation, baffle samples were photomicrographed at the site to be pulsed, then placed in the scatterometer/electron beam chamber presently in use for mirror testing. The chamber was evacuated to 5E-6 millibar or better, and BRDF (Bidirectional Reflectance Distribution Function) was at 10.6 microns, 30° angle of incidence, over a 10° range. Samples were then rotated and translated into position to be pulsed, irradiated with a T=1 beam at 0.2 cal/cm^2, and returned to their original orientation for a second BRDF measurement. The entire process was then repeated at a second site, where samples were subjected to 0.5 cal/cm^2. Targets were maintained at room temperature throughout.

At the completion of testing, scanning electron micrographs (SEMs) were taken at three locations on each target; one unirradiated spot characteristic of the virgin material, and both irradiated regions. Energy dispersive spectroscopy (EDS) was performed at the site of each SEM to determine elements present at the surface. Using a windowless detector, detection of constituents as low in atomic number as carbon (282 eV K-alpha X rays) was possible.

All three baffle materials showed damage at 0.5 cal/cm^2 which was visible to the naked eye. Although mass loss was not measured directly in these experiments, there were indications of "blow off" at 0.2 cal cm^2 as evidenced by collection of particulates on the fluence attenuating screens, as shown in Figure B-1. The E-beam/LWIR Scatter- ometer mirror test facility is dedicated to full time mirror testing, and this level of particulate debris in the chamber could limit mirror testing throughput. Because of this, the smaller SPI-PULSE 300 accelerator was placed in service and this accelerator was used for subsequent radiation tests.

The change in surface specular reflectivity versus electron energy fluence of Martin Black, Chemglaze Z306, Ball Black, Super Desothane and Anodized Beryllium were measured. For most materials, the delamination threshold of a material is indicated by a measurable change in specular reflectivity.

The measurement apparatus (shown in Figure B-2) includes a Helium-Neon laser with a converging lens which gives a beam diameter on the sample of 0.4 mm. The sample is mounted on a translate stage at an angle of 45° from the axis of the incident beam. The part of the beam
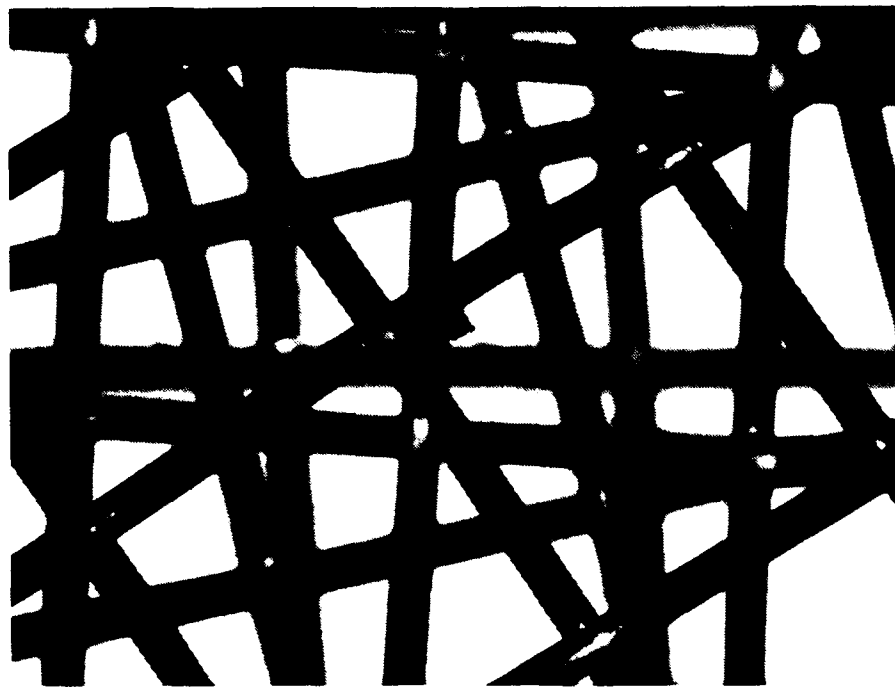
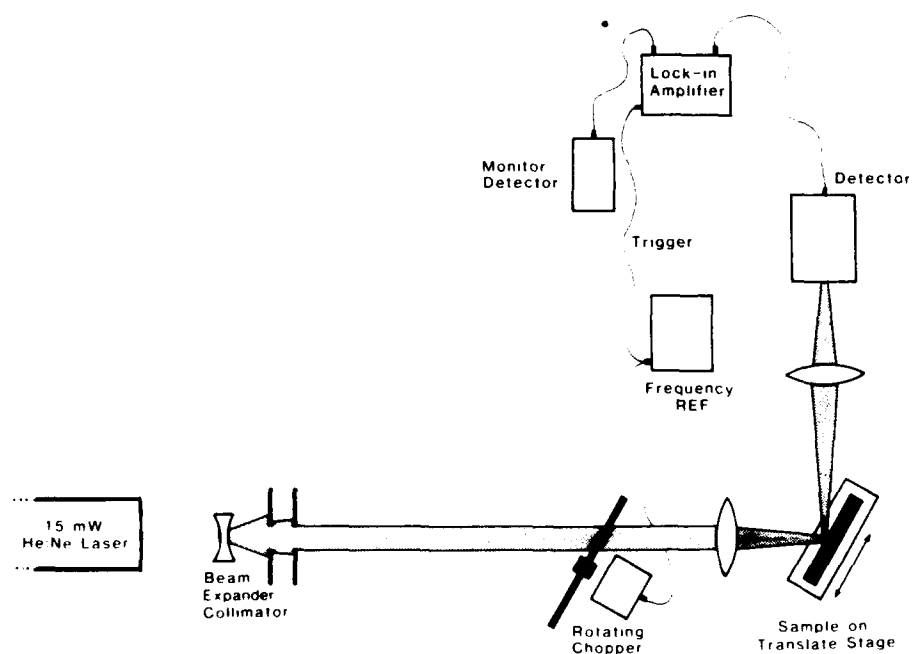FIGURE B-1.   PARTICLE COLLECTED BY FLUENCE ATTENUATING SCREENS.

FIGURE B-2.   SCHEMATIC DIAGRAM OF SURFACE REFLECTIVITY MAPPING
APPARATUS.

B - 2

reflected specularly by the sample passes through a second converging lens, which focuses the beam on a pyroelectric detector. In order to determine absolute reflectivity, a 99+% reflecting mirror was positioned in the sample holder and the resulting power output of the detector was measured. Subsequent measured data was normalized to this power output. To date, all tested baffle materials have shown some reflectivity change as a result of moderate levels of pulsed electron bombardment.

A typical plot of reflectivity versus position is shown in Figure B-3. By cross plotting reflectivity vs position with fluence vs. position, plots of reflectivity vs. fluence can be made. These measurements are shown in Figures B-4 through B-8 and show a substantial increase in reflectivity in the irradiated area in samples of Martin Black, Ball Black, and Anodized Be. Results show a slight change in reflectivity in Super Desothane and an improvement in reflectivity in Chemglaze. With this data, it was possible to make direct delamination threshold measurements. Figure B-9 shows the delamination thresholds for five materials. Figure B-10 shows a delamination site on Martin Black. The two SEM photographs clearly show the loss of surface texture following 0.6 cal/cm^2 electron irradiation.
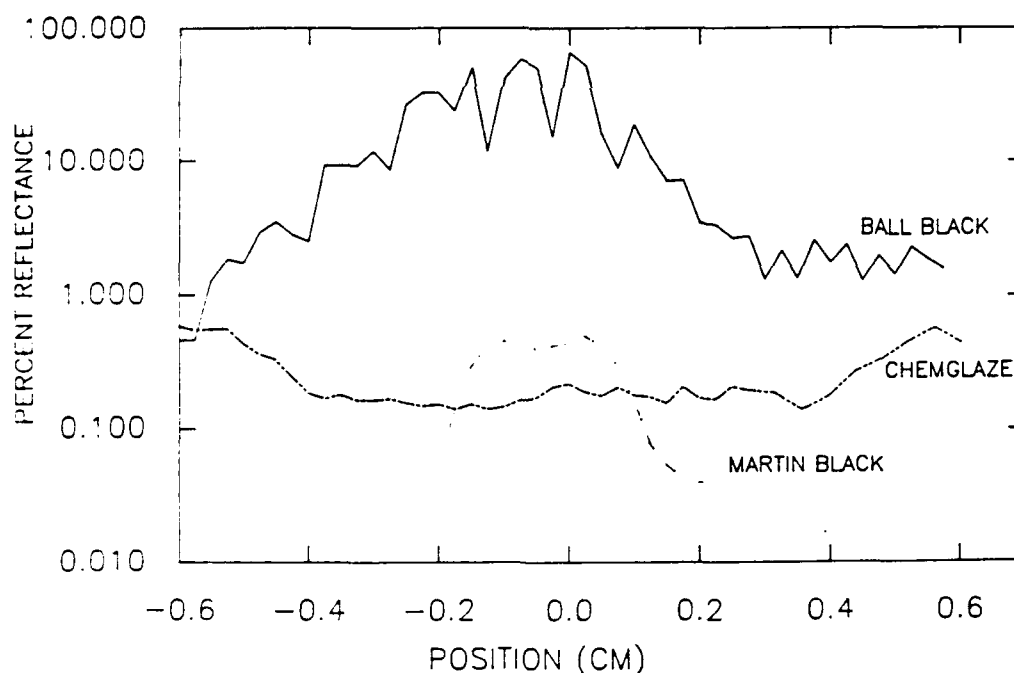

FIGURE B-3.   REFLECTIVITY MAP FOR IRRADIATION SITES IN CURRENT
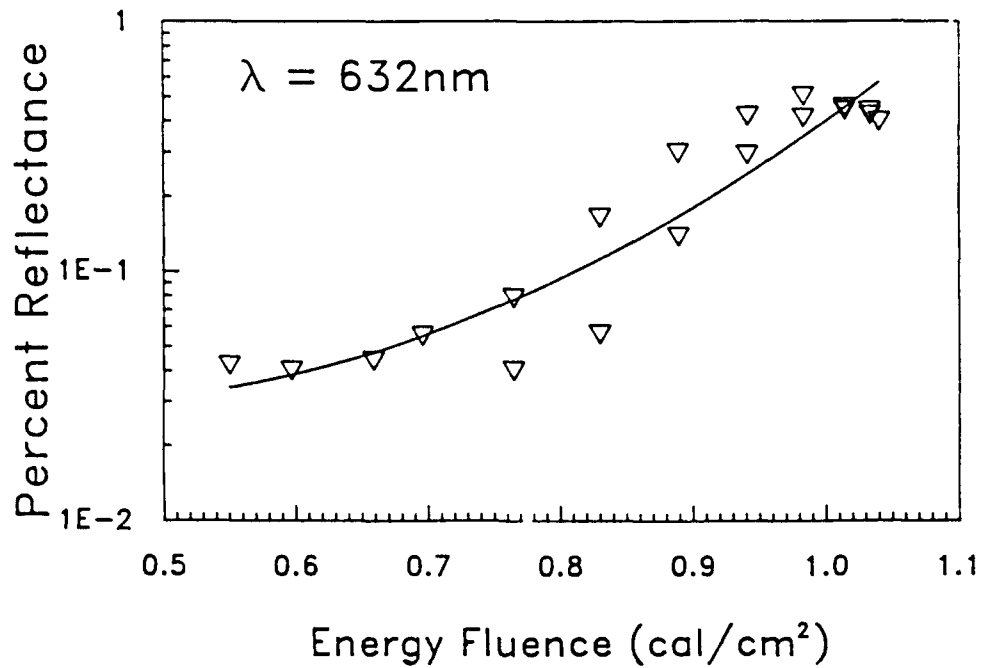COMMERCIAL BAFFLE MATERIALS.

B - 3

FIGURE B-4.   REFLECTIVITY VS. FLUENCE FOR MARTIN BLACK.
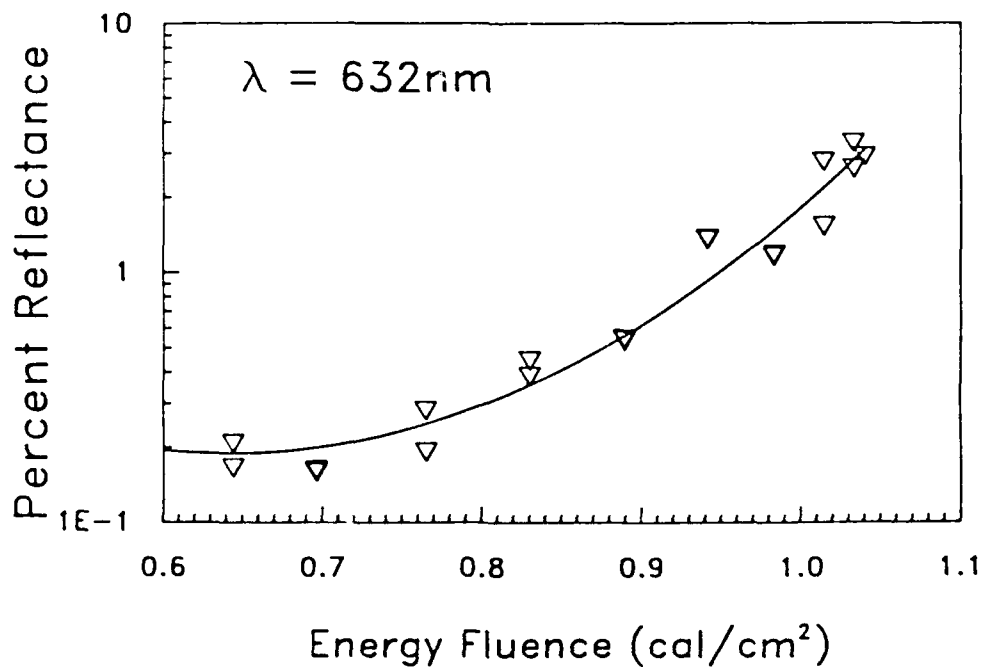

FIGURE B-5.   REFLECTIVITY VS. FLUENCE FOR BeO/Be.
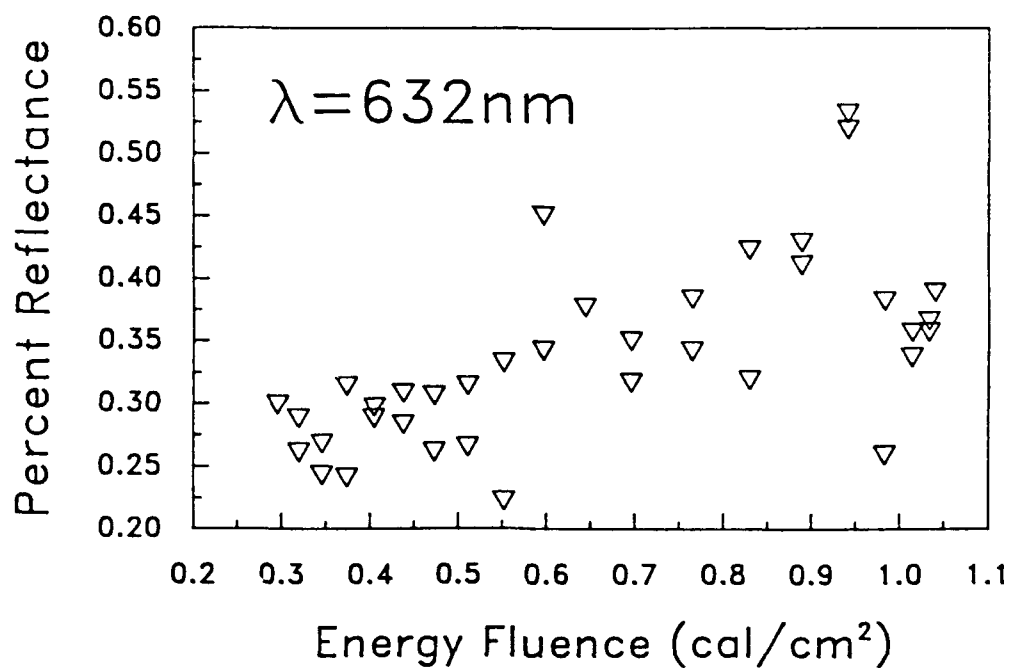
B - 4

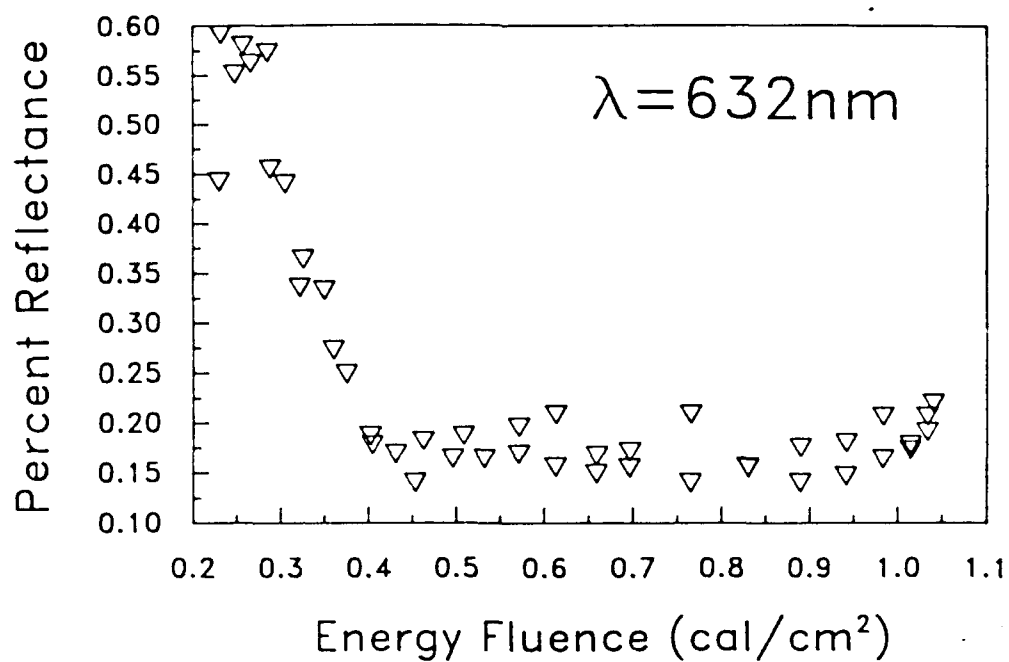FIGURE B-6. REFLECTIVITY VS. FLUENCE FOR SUPER DESOTHANE.

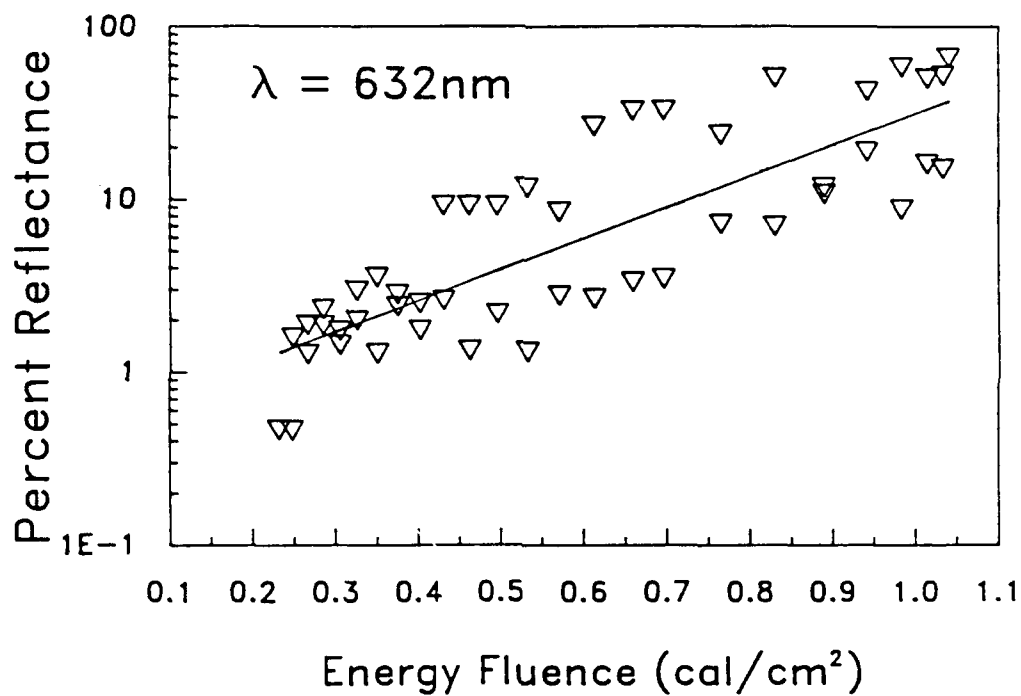FIGURE B-7. REFLECTIVITY VS. FLUENCE FOR CHEMGLAZE Z306.

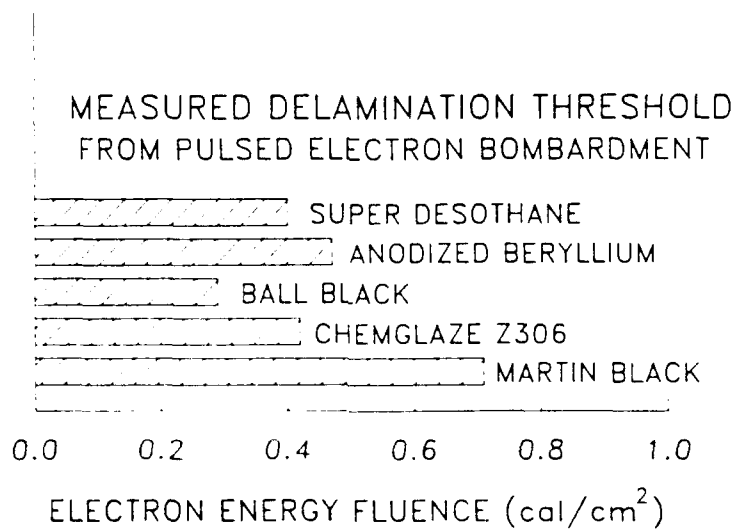FIGURE B-8. REFLECTIVITY VS. FLUENCE FOR BALL BLACK.

FIGURE B-9. COMPARISON OF DELAMINATION THRESHOLDS FOR CURRENT BAFFLE MATERIALS SUBJECTED TO PULSED ELECTRON IRRADIATION.
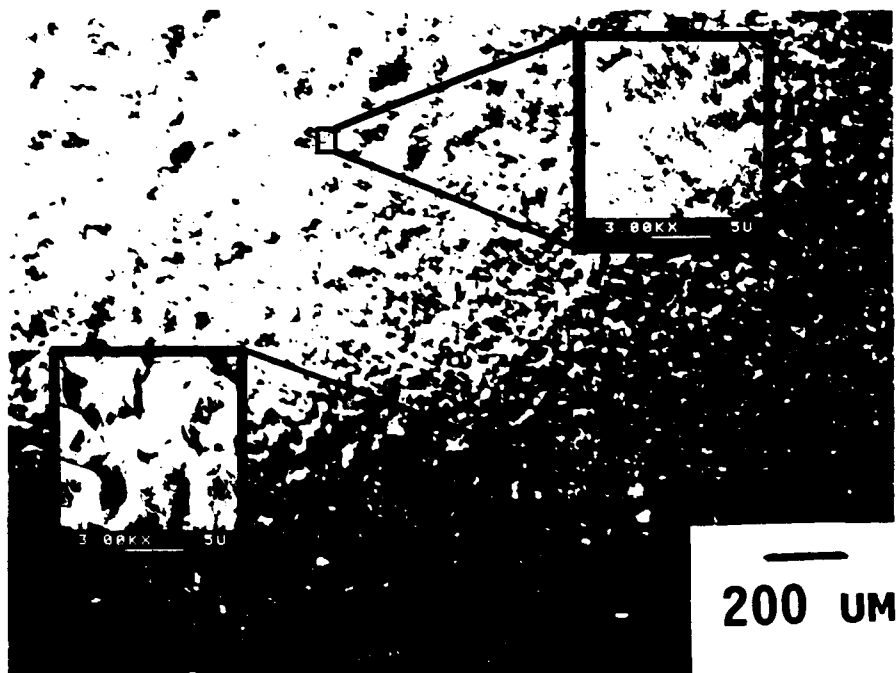
FIGURE B-10.   SEM PHOTOGRAPHS OF MARTIN BLACK BEFORE AND AFTER
PULSED ELECTRON IRRADIATION.

Particle Blow-Off After Irradiation

One damage mechanism which has caused particular concern in baffle materials is particulate blow-off. This is an important consideration in the design of hardened optical systems since particles ejected from the surface of a baffle may foul nearby mirrors, sensors, and other optical components. To assess the extent of blow-off and to design optical systems which are immune to this problem, it is important to know the number of particles ejected as well as their size, direction, and speed.

Catcher Plate Measurements

Experimental data on the distribution of particles ejected from baffle surfaces is scarce, but a crude preliminary experiment with a commercial baffle material was conducted to evaluate this problem's significance.

In this simple experiment, an intense electron pulse passed through an annular metal plate before striking the dielectric target surface. Particles ejected from the surface struck the metal plate and some of them stuck. Figure B-11 shows a schematic diagram of the experimental arrangement. The top half of Figure B-12 shows a polarized light micrograph of particles collected after irradiation of a Chemglaze Z-306 sample with an electron fluence of roughly 1 cal/cm^2. Particles appear in the photograph as dark irregular objects. In this analysis, particle size is defined to be the radius of a circle with an area equal to the particles projected area. Figures B-13 and B-14 are for Ball Black and Martin Black respectively.
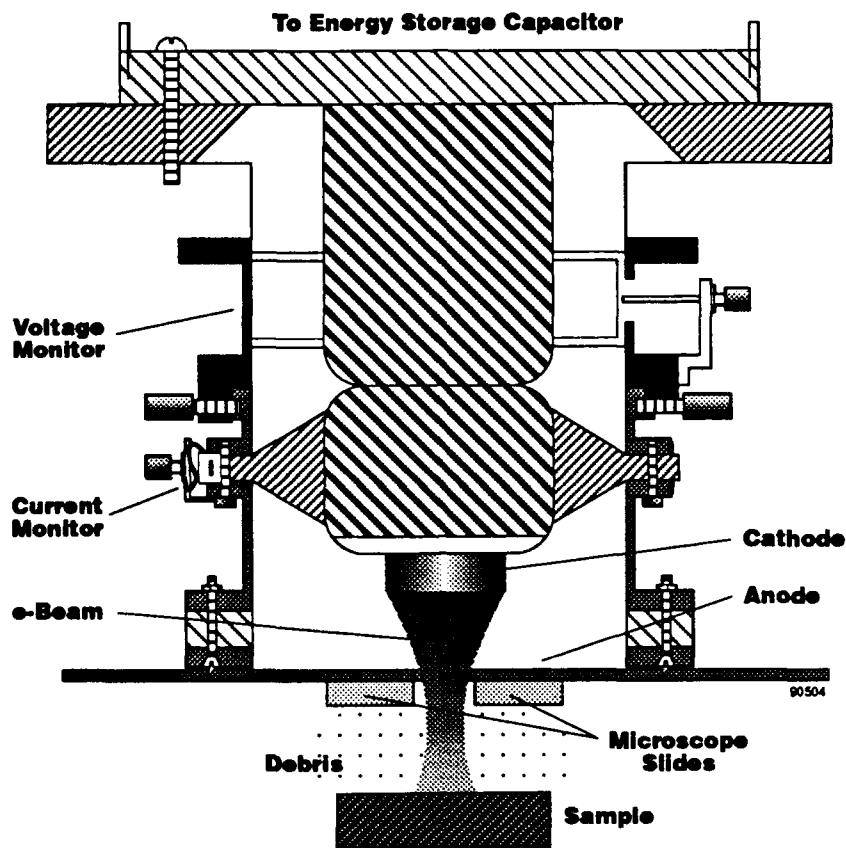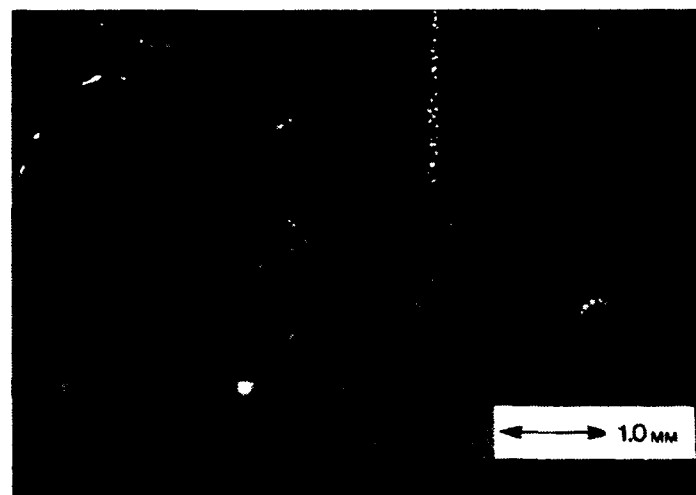
B - 7

FIGURE B-11.   SCHEMATIC OF SPI-PULSE 300 FIELD EMISSION DIODE WITH
CATCHER PLATE EXPERIMENT INSTALLED.

FROM CHEMGLAZE Z306 AT 0.6 cal/cm2

Particle Size Distribution

FIGURE B-12.   PARTICULATE DEBRIS GENERATION FROM BLOW-OFF BY
CHEMGLAZE Z306.

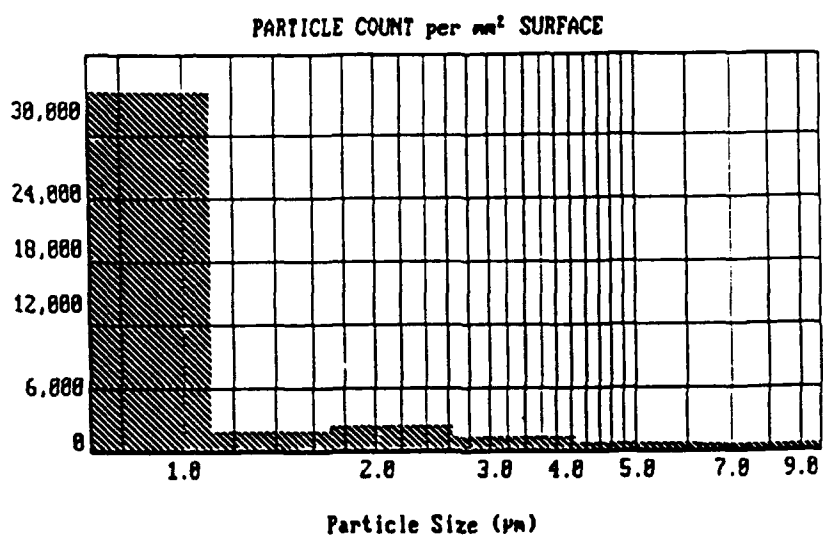PARTICLE COUNT per mm² SURFACE

FIGURE B-13.   PARTICULATE DEBRIS GENERATION FROM BLOW-OFF BY BALL
                BLACK.
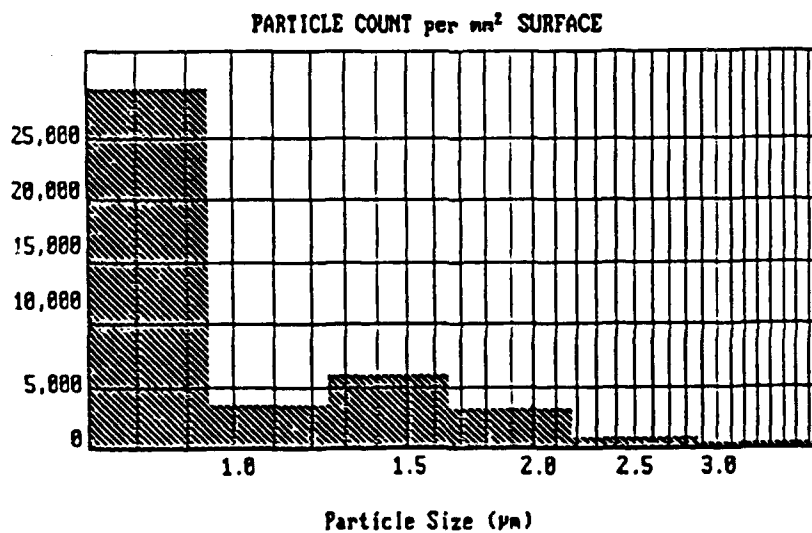
PARTICLE COUNT per mm² SURFACE

FIGURE B-14.   PARTICULATE DEBRIS PRODUCTION FROM BLOW-OFF BY MARTIN
                BLACK.

For Chemglaze Z 306, a plot of particle sizes measured shows that the sizes ranged from less than a micron to roughly 50 microns. The mean size, skewed somewhat by the larger observations, is 6.8 microns and the median size is 2.4 microns. The counts indicated in the histogram are normalized to a 1 mm² baffle surface area.

Ball Black showed a much greater number of particles, 43,500/mm² with a mean size of 1.1 microns. The effective contamination level (MIL-STD-1246A) was 1500.

Similarly Martin Black produced prodigious amounts of dust; 42,700/mm² with a mean of 1.0 microns and a resultant contamination level of 1400. The mean particle size and high number, when compared with sintered alumina suggests that texture governs the amount and size of the particles produced.

For smooth (untextured) surfaces it is believed that the size of particles is governed by the enthalpy to melt. This model works well for smooth alumina disks and appears reasonable for smooth painted Chemglaze surfaces. This model cannot explain the measured particle distributions from the textured baffle samples and a more involved model which incorporates surface texture will be required. In addition, this will require additional experimental evidence; perhaps by making and pulsing textured and smooth surfaces of different materials.

APPENDIX C

ENVIRONMENTAL EFFECTS TESTING

Thermal cycling under vacuum can cause mechanical damage to baffle materials such as brittle fracture, spalling and layer delamination because of thermal mismatches and trapped gases or liquids. The capability of performing accelerated thermal cycle testing under vacuum on baffle material samples is very important. Storage in poor vacuum or periodic exposure to water and other vapors can lead to cryodeposition on and in porous baffle materials. The cryodeposits can change optical properties of surfaces and enhance damage effects. Composition and deposition rate are key issues in the effects of cryodeposits on the baffle material and on system optical performance.

During launch, the sensor system will be subjected to high acceleration and vibration levels which could cause damage to baffle materials and structures. The ability to survive the launch environment without significant optical or dimensional changes is a critical issue for baffle materials. The adhesion of the baffle coating to its substrate must be tested against vibrational and acceleration stresses similar to those anticipated during launch. The coatings must also withstand many thermal cycles between room and cryogenic temperatures.

Thermal Cycling Test

A thermal cycling chamber[1,2] was constructed and initial tests were performed on commercially-available baffle materials. The apparatus, shown in Figure C-1, works by clamping a baffle material sample to a heavy copper plate inside an evacuated tube. The apparatus was immersed in liquid nitrogen and held there until the nitrogen ceased to boil. It was then removed and gently brought back to room temperature with a heat lamp. The sample was then removed and examined for delamination, cracking, or deformation. Some samples were also held at LN_2 temperature for periods up to two hours. In addition, some samples were dropped directly into the LN_2 to test the effect of quenching rate on coating delamination.

Chemglaze Z306, Super Desothane, and 3M ECP 2200 were chosen for testing because they are organic paints which are apt to fail under thermal stress. Samples of both were cycled repeatedly (up to four times) and directly dunked into LN_2. No samples showed any visible delamination.

Simulated Launch Vibration Test

One damage mechanism which had caused concern for the integrity of optical baffle material is particulate debris production due to launch vibration. To assess the extent of this problem, we have conducted an experiment with several commercially available baffle materials.

In this experiment, two commercially available baffle materials were mounted in separate fixtures, with each held opposite a silicon wafer catcher plate. The fixtures were mounted into an MDC vacuum cross along with a control blank. The assembly was evacuated and taken to a vibration test facility. The specifications to simulate launch vibration from a solid rocket booster, as given by USASDC/Teledyne Brown Engineering:
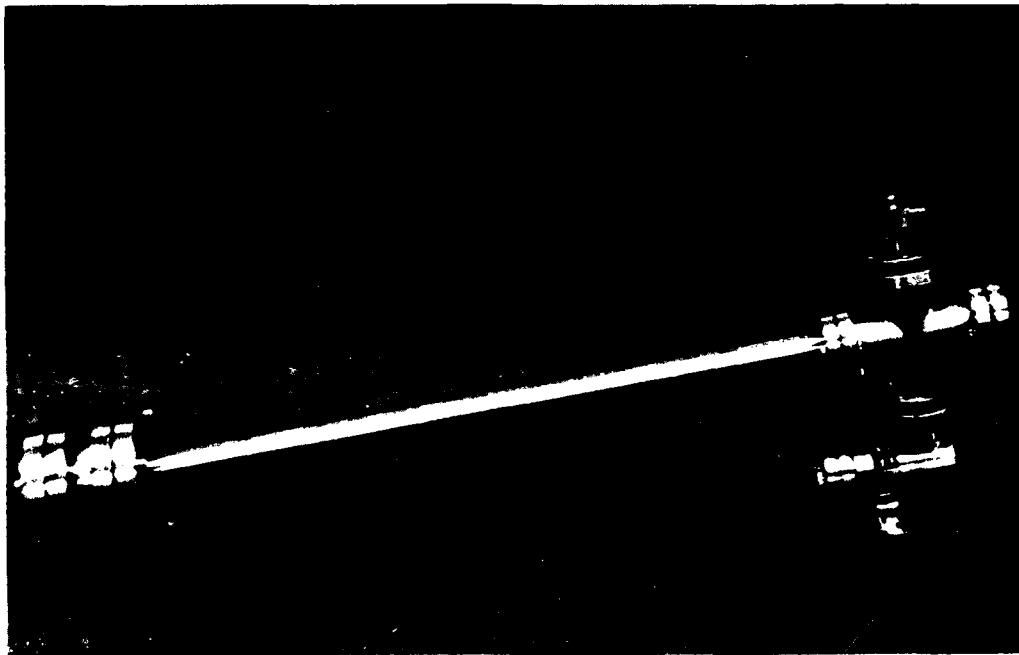
FIGURE C-1. PHOTOGRAPH OF THE THERMAL CYCLING TEST CHAMBER FOR
EVALUATING DELAMINATION AND OTHER POTENTIAL PROBLEMS
IN BAFFLE MATERIALS.

$$40g \quad 40\text{-}2000 \text{ Hz}$$
$$20g \quad 20 \text{ Hz}$$

for ten seconds to simulated launch tube shock, and:

$$0.003 \text{ g}^2/\text{Hz} 20\text{-}2000 \text{ Hz}$$

white noise spectrum power spectral density to simulate in-flight vibration. Due to the limitations of the shake table at Textron Defense Systems, it was not possible to duplicate this spectrum. The three-axis-vibration PSD used in the test is shown in Figure C-2. The integral under the upper curve (launch tube shock) corresponds to an RMS value of 20.64 g and the integral under the lower curve (in-flight vibration) corresponds to an RMS value of 2.52 g.

The two materials tested were Martin Black, which uses an electrochemical process to apply an anodic black dye to aluminum, and Ball Black, a chemically etch-blackened electroless nickel coating. Following the vibration test, the assembly was dismantled in a class 100 environment and the silicon catcher plates removed for analysis under the microscope. The two histograms in Figure C-3 show the results of the test. Both materials produced noticeable quantities of debris. The catcher plate opposite the control blank was actually cleaner after the test, indicating that the particle counts on the other two catcher plates could be low.
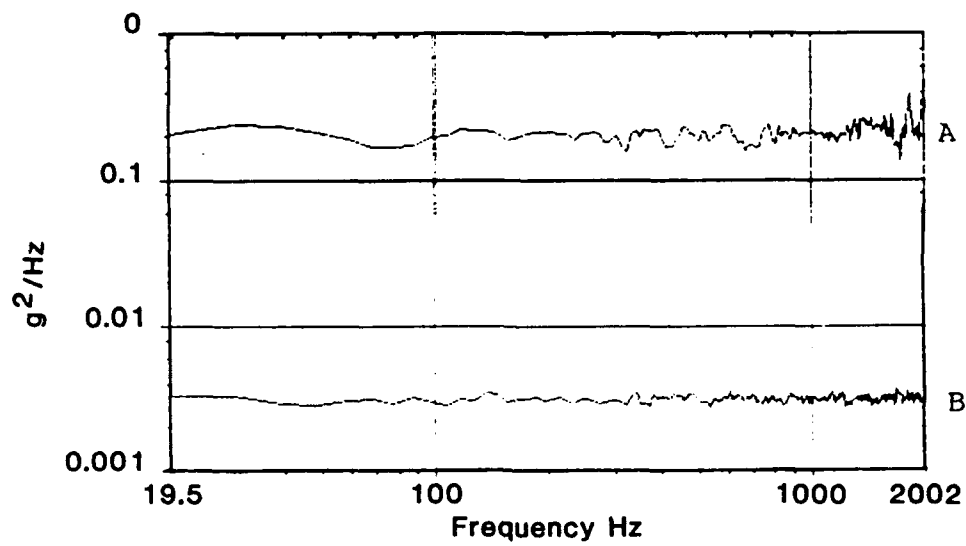
FIGURE C-2.   POWER SPECTRAL DENSITY a) LAUNCH TUBE SHOCK, b) IN-FLIGHT
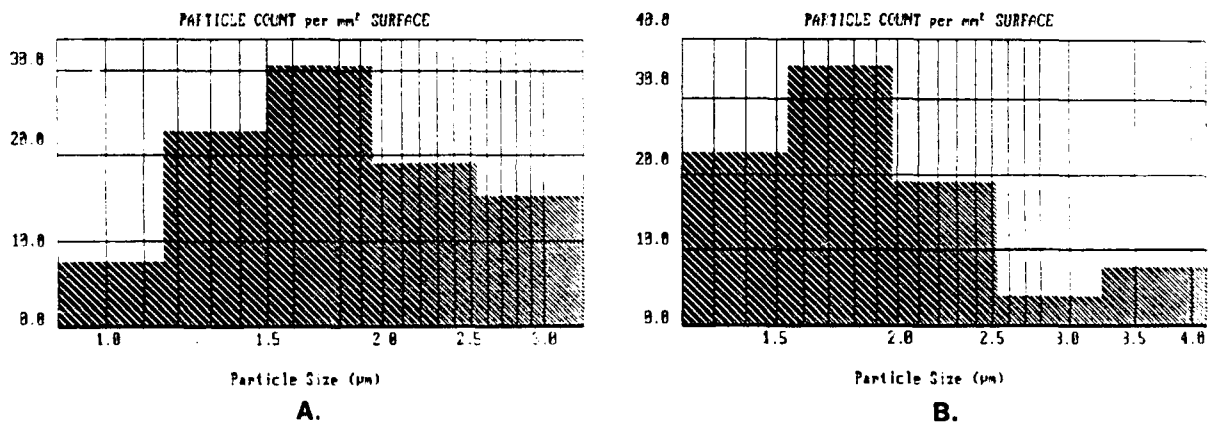   VIBRATION.

A.   B.

FIGURE C-3.   PARTICULATE DEBRIS PRODUCTION a) MARTIN BLACK b) BALL
                BLACK.

C - 3

Atomic Oxygen Exposure Test

The SDI Delta Star satellite has on board a Spire designed experiment which is measuring the erosion rates of materials exposed to the space environment. Erosion is measured in two ways, with a quartz crystal microbalance and with an actinometer bridge. The microbalance has a film deposited on it and measures the erosion rate by relating the change in resonant frequency to mass loss. This device is similar to those used to measure film growth in IBAD and other thin film processes. In this application, however, it is being used to measure film erosion, not growth. The actinometer bridge has two film coated silver strips. When the film erodes away, the atomic oxygen reacts with the silver to produce a dramatic change in resistivity. By knowing the film thickness, and measuring the elapsed time between breakthroughs, an erosion rate can be calculated. Telemetry from the microbalances indicates that a Spire boron nitride film, exposed to an average atomic oxygen flux of 4.7461 x 10^{13} $O/cm^2/s$ is relatively unaffected by it (Figure C-4), while a parylene film eroded away in about 168 hours.
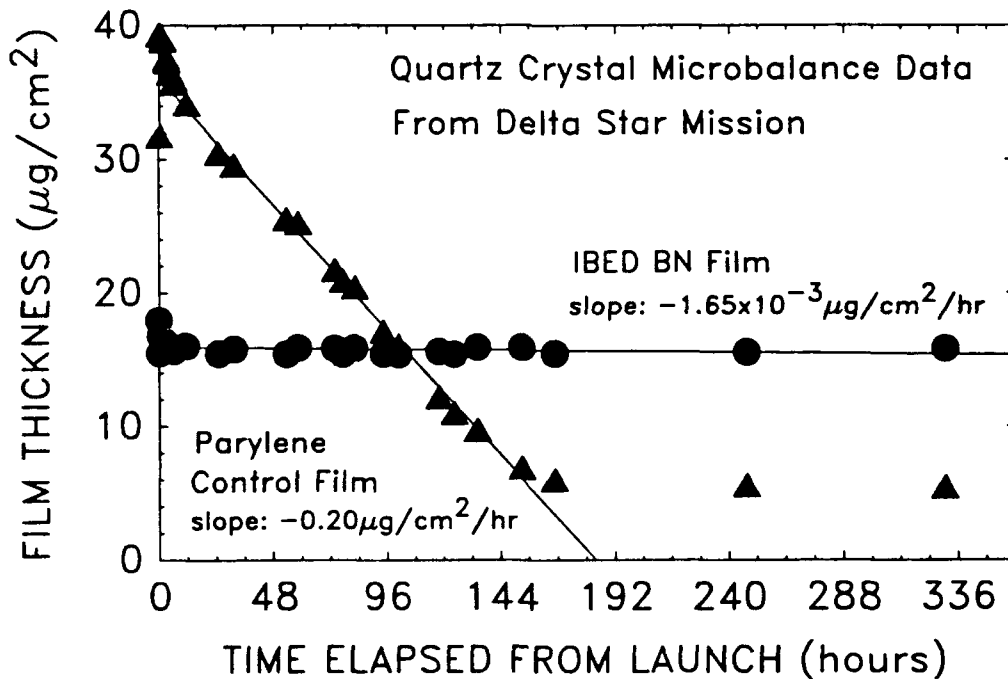

FIGURE C-4.   FILM THICKNESS VS. EXPOSURE TIME FOR FILMS EXPOSED TO LEO OXYGEN RAM FLUX.

Another experiment prepared for the Delta Star mission consists of a passive panel (Figure C-5) containing coupons of several different materials. But this panel was not launched. However, the data retrieved from NASA's Long Duration Exposure Facility, should provide much data on the long term affects of space exposure on materials.
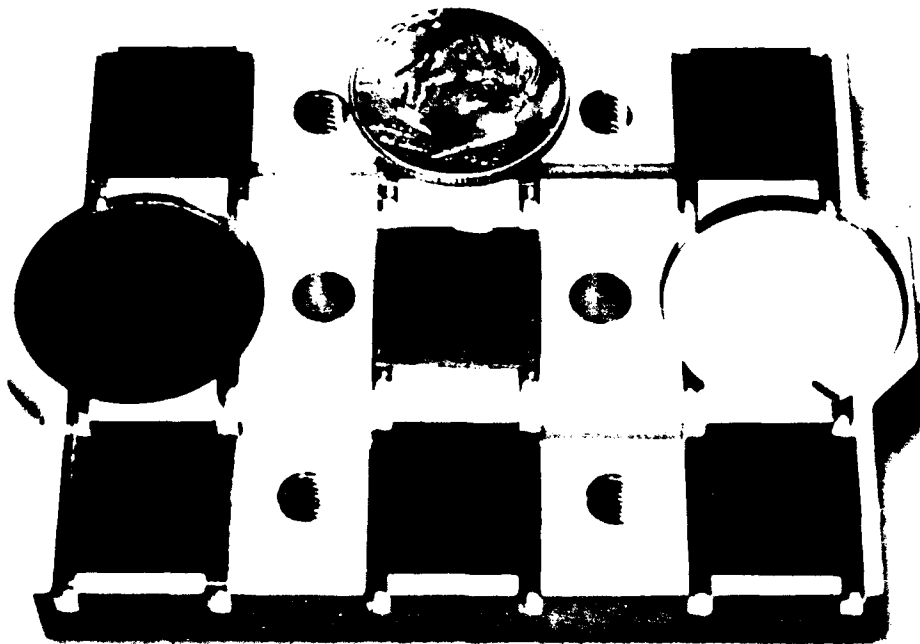

FIGURE C-5. PHOTOGRAPH OF THE SPIRE PASSIVE PANEL EXPERIMENT.

1. S.M. Pompea, D.W. Bergener, D.F. Shepard, K.S. Williams, SPIE Proceedings, 511, 24 (1984).

2. J.T. Visentine, L.J. Leger, J.F. Kuminecz, and I.K. Spiker, AIAA Paper 85-0415, AIAA 23rd Aero. Sci. Mtg., Jan. 1985, Reno, NV

APPENDIX D

ADVANCED MODELING OF BAFFLE

MATERIAL PERFORMANCE

The mechanisms and criteria for damage are critical issues for radiation hardened optical baffle material development. The important damage types are those which can cause changes of the bidirectional reflectance distribution function (BRDF) of the baffle surface, those which can generate particulate debris, or both simultaneously. BRDF changes can increase the diffuse and/or specular reflectance of the baffle material. Particulate debris can be transported inside the telescope and lodge on surfaces such as mirrors, windows, and lenses. Both effects can cause extreme increases of off-axis stray light transmission in a modern telescope.

Damage mechanisms which can degrade BRDF include surface melting, vaporization, spalling or brittle fracture. The removal of a cryodeposit layer can also cause BRDF changes at optical wavelengths where the cryolayer is strongly absorbing or strongly reflective. Vaporization and melting of surface material can also generate particulates or, in the case of cryodeposits, redeposited cryolayers on cooled surfaces.

Energy deposition in the baffle material can cause immediate damage by melting and vaporization as well as stress-induced damage. Stress waves propagating into the bulk material can induce fracture and spalling at interfaces between coatings, laminations, and at free surfaces. The stresses can be generated by thermal response of the material or by blow-off impulse. Heating by direct X-ray energy deposition or thermal conduction can change mechanical strength and generate stresses by thermal expansion mismatch. All of these effects can cause baffle material damage and failure, and, at the beginning of this program, it was not known which mechanisms are the most dangerous for specific materials.

A weapon detonated in space emits a variety of radiations, including gamma rays, electrons, ions, neutrons, X-rays, thermal pulse, and debris. Most of these pose no significant threat to baffle materials, because they either carry a minor fraction of the total yield, are not strongly absorbed, or are emitted over a long enough time for their effects to be internally dissipated. In this category fall prompt and delayed neutrons and gamma rays, electrons, and ions. Preliminary calculations indicate that, at ranges where X-ray damage can be inflicted on baffle materials, debris will not coat surfaces to a depth sufficient for alterations of optical absorption or reflection. Characteristics of exoatmospheric thermal pulse are not well known; radiating time is thought to be relatively long and integrated energy small, suggesting that it represents a second order threat. X rays, therefore, are the major concern for baffle damage.

Roughly 80 percent of the energy released in a nuclear burst appears as soft X rays, which are strongly absorbed in materials with medium to high atomic number (Z). X rays, because they represent most of the weapon output and interact more strongly than neutrons or gammas, generally represent the greatest threat to optical baffles. X-ray emission energy is distributed approximately as a blackbody. In practice, the spectrum may deviate significantly from pure blackbody behavior, exhibiting time dependence as well as non-blackbody photon distribution. While the blackbody assumption may be adequate for many problems involving relatively thick-walled structures, dose in thin surface layers can be seriously misrepresented if the actual spectrum contains more low energy photons than predicted by a blackbody. Late time plasma cooling can be expected to produce a low energy, non-blackbody "tail" which will be absorbed in the outermost few microns of surfaces in the X-ray line-of-sight. This may dramatically increase surface dose and lower the threshold for damage related to alteration of surface quality; the effect on cryodeposits is likely to be particularly important.

Damage mechanisms in the baffle material are dependent on the details of the X-ray spectrum and its temporal development. Correlations between damage types and incident threats need further exposition through improved analytical and computational models of X-ray absorption and the response of the absorbing media, whether it be surface cryodeposits or the underlying baffle materials. Thermal pulse threat should be studied further so that its possible relation to baffle damage can be determined with high confidence.

Comparison of an Ideal Blackbody and "Holland Tail" Radiation Sources

Spire's PUFF-like PC-compatible deposition code "XRAYDEPO" was modified to incorporate a "Holland Tail" employing parameters scaled from data presented by MRC at the July 18, 1987 program kickoff. Shape of the resulting normalized "Holland-body" is compared to a standard blackbody in Figure D-1, where it can be seen that the former
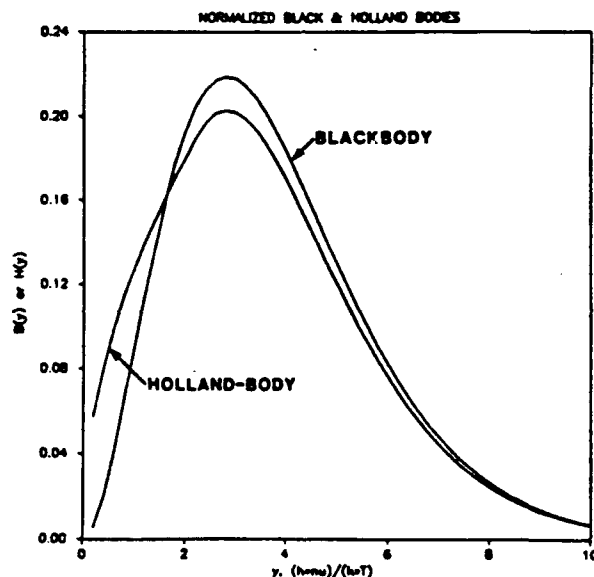

FIGURE D-1.   NORMALIZED SPECTRAL DISTRIBUTIONS OF BLACK-BODY AND HOLLAND-BODY RADIATION SOURCES.

represents a significant shift toward lower values of energy (Figure D-1 employs dimensionless photon energy, "y", dependant on source temperature source energy in keV). The extent of this shift can be determined by plotting and comparing cumulative integrals for black- and Holland-bodies, as has been done in Figure D-2. For a given value of "y", the curves give the fraction of total energy lying below y; because both black- and Holland-bodies are normalized, their integrals approach unity at large values of y. Reading from Figure D-2, approximately 10% of the Holland-body lies below y = 1, more than twice the low energy content of a standard blackbody; at y = 2 the corresponding values are 22 and 18% respectively. Above y = 3, the curves converge.
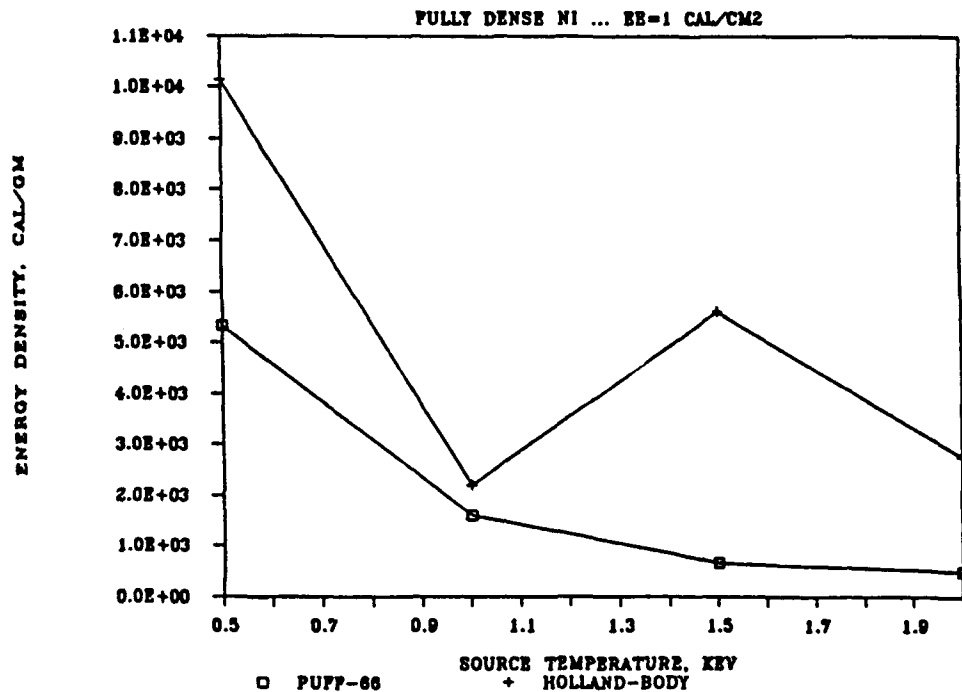
FULLY DENSE NI ... EE=1 CAL/CM2

FIGURE D-2.   NORMALIZED CUMULATIVE INTEGRAL FUNCTIONS FOR BLACK
AND HOLLAND BODIES.

The effect of employing the two spectral descriptions in front surface dose calculations for fully dense nickel, representing Ball Black, is shown in Figure D-3; coordinates are energy density and source temperature. The upper curve results from assuming a Holland-body, the lower from a standard blackbody. Because it is softer, the Holland-body results in greater surface deposition, as expected. However, because of its enhanced low energy component, the nickel L-edges (centered on 0.86 keV) have a profound effect on Holland-body dose, causing the irregular behavior seen in Figure D-3; whereas the ratio Holland-body/blackbody is about 2 for 0.5 keV spectra, at 1.0 keV it drops to 1.3, then rises to about 8 at 1.5 keV. The importance of a good threat description and of accurate low energy absorption cross sections is underscored by this figure.

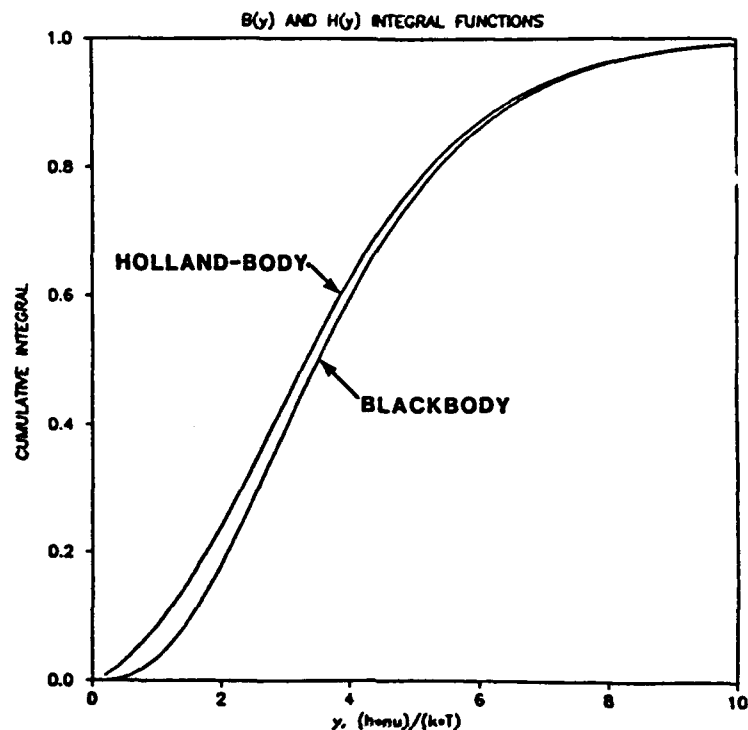D - 3

B(y) AND H(y) INTEGRAL FUNCTIONS

FIGURE D-3   FRONT SURFACE DOSE VS. BLACKBODY SOURCE TEMPERATURE FOR BALL BLACK. Upper curve, Holland body source. Lower curve, Black body sourced. Incident energy fluence is 1 cal/cm^2.

Radiation Effects on Coatings

   To complement the optical performance calculations performed by BRO using Martin Black, NBS/Ball Black, and Chemglaze Z-306 as representative present-day baffle coatings, XTDEPO was employed to estimate surface dose, depth of incipient melting, and blow-off impulse for these same materials. Martin and Ball blacks were assumed to be composed of alumina and nickel respectively, ignoring the possible presence of high atomic number contaminants; Chemglaze was treated as a silica-filled urethane. Representative results of melt depth calculations (based upon incipient melting) for Martin Black are shown in Figure D-4. Standard blackbody spectra were assumed and energy redistribution was neglected in deriving these figures. Blow-off impulse estimates made using modified BBAY theory are shown in Figure D-5 for Martin Black.
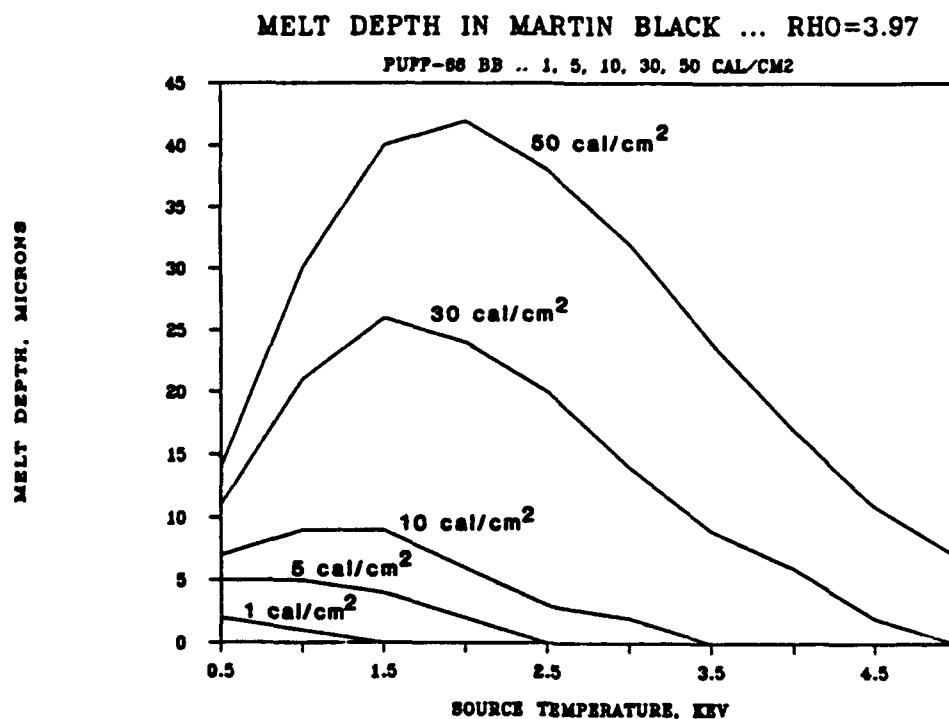
MELT DEPTH IN MARTIN BLACK ... RHO=3.97

MELT DEPTH, MICRONS

50 cal/cm^2

30 cal/cm^2

10 cal/cm^2

5 cal/cm^2

1 cal/cm^2

SOURCE TEMPERATURE, KEV

FIGURE D-4.   MELT DEPTH VS. BLACKBODY SOURCE TEMPERATURE FOR MARTIN BLACK.

MARTIN BLACK (ALUMINA) ... RHO=1.0

MBBAY ... 1, 5, 10, 30, 50 CAL/CM2

BLOWOFF IMPULSE, TAPS

50 cal/cm^2

30 cal/cm^2

10 cal/cm^2

5

1

SOURCE TEMPERATURE, KEV
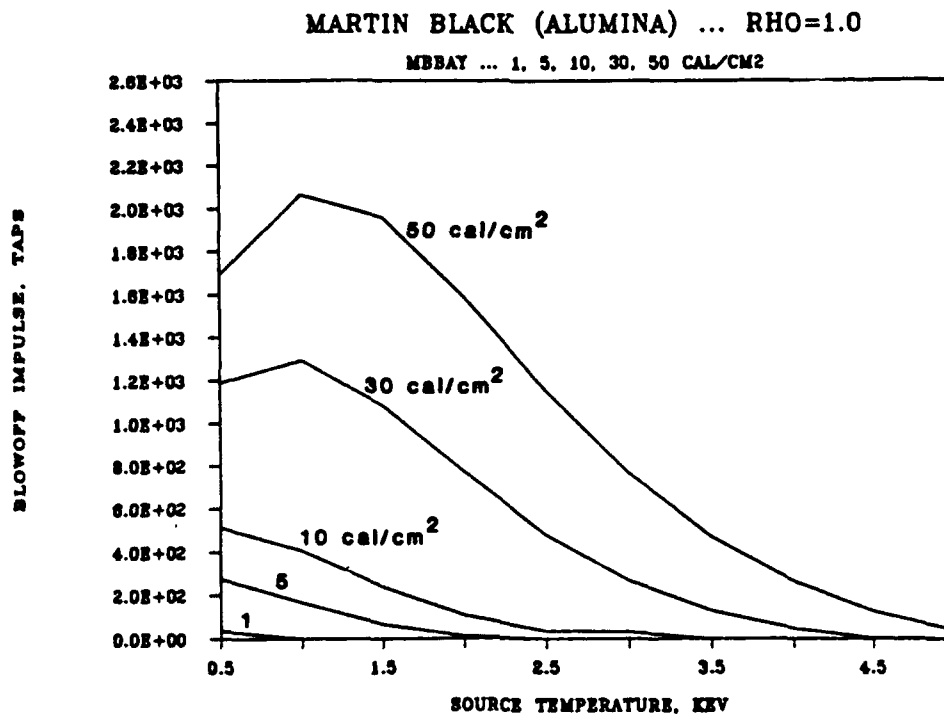
FIGURE D-5.   BLOWOFF IMPULSE FROM MARTIN BLACK RHO = 1.0 g/cm^3.

D - 5

Modeling of Porous Surfaces

X-ray absorption calculations often assume that photon energy is completely converted to thermal energy at the site of the first scattering or photoelectric absorption event. This local thermalization allows convenient synthesis of depth/dose profiles, in terms of tabulated absorption cross sections, either by transport equation methods (e.g., PUFF-TFT and FSCATT) or by Monte Carlo methods (e.g., TIGER and $(MC)^2$). Often, this assumption is physically reasonable since the range of photoelectrons at energies of a few keV or less is quite small (dozens to hundreds of angstroms) compared to dimensions of interest in most calculations. In baffle materials, on the other hand, photoelectrons as well as X rays from second and higher order processes may escape to vacuum (either pores or space between adjacent columns) where their range is appreciable compared to the coating thickness and other dimensions of interest. Because of this, complete local thermalization of absorbed X rays is unlikely for baffle materials.

Since porous baffle materials are not fully dense, the top-most surface layers do not completely shield sub-surface layers from incident radiation: X rays (and charged particles) can "shine down" into vacant spaces and strike the material deep below the outer surface. After inelastic scattering events have occurred, energy carried away by photoelectrons as well as second and higher order radiation processes may also "shine down" into vacant spaces. Both of these effects deepen the depth/dose profile for X-ray energy deposition in textured baffle surfaces.

Electrons and photons in a textured sample of a given material are apt to travel in vacuum some fraction of the time. Thus the density and mobility of charge carriers (or virtual charge carriers such as photons which may travel some distance and stop in a photoionization event) is sensibly different than in a uniform, fully dense slab of the same material. Because of this, dielectric functions which describe the response of the medium to transient forcing functions must be modified to account for texture effects.

In addition, mechanical response of a textured specimen to a sudden thermal shock is likely to be quite different than the response of a uniform, fully dense specimen. In the case of porous materials, the thin walls separating adjacent pores may deform under rapid thermal loading or under radiation pressure at extreme fluences. Columnar materials with individual dendrites normal to the surface may offer little lateral support against the thermal expansion of an individual dendrite and may show substantially less lateral shear strength than fully dense materials.

Finally, the optical properties of baffle materials depend strongly on surface texture. Changes in surface texture, such as near-surface melt and re-solidification, or the crumbling and re-distribution of solid material will lead to significant changes in optical properties. Even without incident radiation, highly textured materials should cryotrap gaseous species more efficiently than perfectly flat surfaces. The resulting cryodeposits may change the surface texture, by closing pores for instance, and influence optical performance of the baffle.

There are two categories of computational methods for dealing with the complexities of random textured surfaces. Broadly, methods in the first category endeavor to solve the problem all at once. They rely on large, accurate computer programs for finding numerical solutions to

methods (and the bulk of the work in the methods) stems from efforts to specify the material in great detail and with exceeding accuracy. This is crucial to the success of these methods since discrepancies between the model and the actual material govern quality of the final solution. These methods are not necessarily crude: there are a number of elegant analytical approaches based on the fractal geometry of textured surfaces, for instance.

Generally, the difficulty with methods which attempt to solve the problem all at once is that these methods often do not illuminate the fundamental physics of the problem. Because of this, changes in design or material properties require an entirely new solution. Solutions of this sort do not provide much information on ways to make incremental changes to a material which will improve its suitability for a given application: exclusive reliance on them makes material design a trial and error operation.

Methods in the second category involve the solution of a number of smaller and simpler problems which resemble the larger problem. This permits introduction of complexity and texture in a controlled way so that the fundamental physics of the problem is constantly visible. Small regions of the problem may be readily examined in greater detail; this allows and encourages recognition of effects which are important and identification of those which are not. These methods, which allow incremental learning about the problem, provide a body of design information for evaluating the impact of various changes. Incremental solutions which are not necessarily analytical and incremental approaches are also frequently used in numerical work (e.g., the automatic sub-zoning supported by most main-frame finite element codes).

For baffle hardness calculations, an incremental computational approach is an important adjunct to large-scale computer solutions of the complete problem. This approach will be implemented by using the SPIRE Hexagonal Fiber Bundle (HFB) model to introduce porosity into the problem in a controlled and understandable way.

This model (Figure D-6) takes texture into account by representing a complex surface as a tightly packed bundle of right circular cylinders. In the model, these cylinders may be either hollow or filled (in which case the matrix is hollow). The diameter, center-to-center spacing, and aspect ratio (length:diameter) may be separately specified. As Figure D-7 demonstrates, this model is not an unreasonable approximation for some commercial baffle materials. The top portion of Figure D-7 shows an electron micrograph of Ball Black (electroless nickel) while the bottom section shows electron micrographs of two hexagonal arrays of glass fibers. Hollow cylinders are on the left and solid cylinders on the right; these are photographs of micro-channel plate electron multipliers in different stages of manufacture.

The advantage of assuming this regular arrangement is that the symmetry allows the use of many simplifications familiar from solid state physics. In addition, it exploits existing computational technology developed for analyzing other related problems. In particular, the Spire HOT-ROD code which was originally developed for analyzing heat flow problems in micro-channel plate structures can be readily adapted to baffle calculations. HOT-ROD is particularly suitable for this analysis since it allows the user to specify arbitrary heat deposition profiles as a function of time.
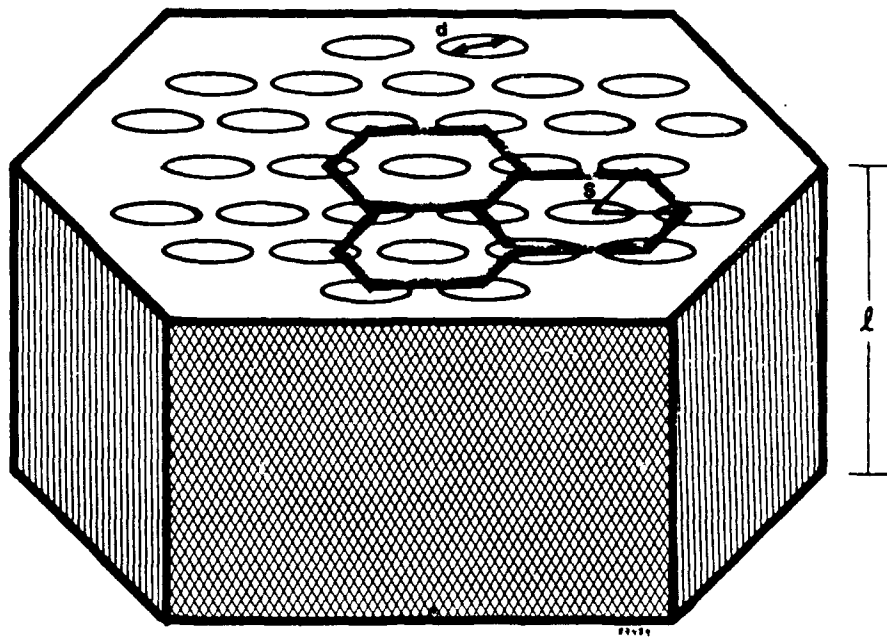
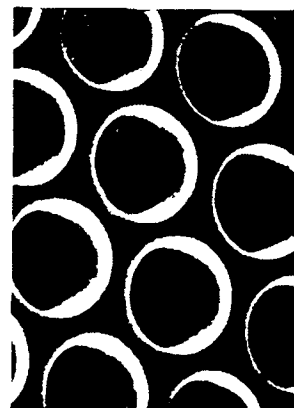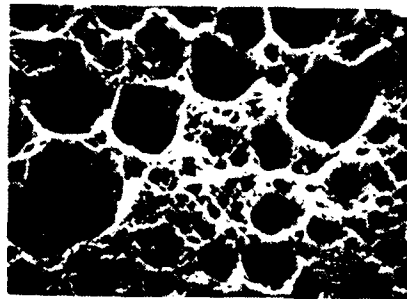FIGURE D-6.   HEXAGONAL FIBER BUNDLE MODEL OF A BAFFLE MATERIAL.

FIGURE D-7.   PHOTOGRAPH OF BALL BLACK AND REGULAR DRILLED ARRAYS
                OF VARYING ASPECT RATION.

<u>Hotrod</u>

Our studies of charge build-up and decay required only approximate values for electron range and straggle because of the large uncertainties in measured values of conductivity and capacitance during intense irradiation. Micron-scale studies of temperature profiles during and after electron bombardment impose much more stringent requirements on the accuracy of electron range calculations. However, because of the computational speed and convenience of the simple model described above, we sought to refine this model so that it could be used in thermal calculations.

The first issue in the thermal calculations is one of scale. How do times and distances of interest (pulse length and layer thickness) relate to characteristic times and distances for thermal diffusion? In particular, if there is appreciable heat conduction during the electron pulse, then the electron energy deposition problem cannot realistically be de-coupled from the heat-flow problem. Heat flow is governed by the thermal diffusivity of the material, $D = k/ C$. Here, k is the thermal conductivity, the density of the material, and C the specific heat. Measured room-temperature values of these material constants for alumina[1] give a value, $D = 0.09309$ cm^2/sec. The characteristic diffusion distance is given by $d = (2Dt)^{1/2}$ where t is the time of interest. For temperature profile calculations with 1 micron depth resolution, then, a characteristic time for heat flow is 53 nsec. Since this time is comparable to the pulse length of the SPIRE T=1 electron beam, thermal calculations require a time dependent model which accounts for heat flow and depth/dose profile changes during the electron pulse.

Time dependent thermal calculations require instantaneous electron depth/dose energy deposition profiles at many different times during the electron pulse. For this purpose, Monte Carlo simulations of electron energy deposition are quite unwieldy since the computation for each time step requires tracking the histories of several thousand mono-energetic electrons. Clearly, a better procedure would be to find an analytic form for electron depth/dose profiles as a function of incident electron energy for various materials. Fortunately, interest in electron microscopy and electron beam microanalysis has spurred a great deal of work in this field. In this report, we examine some of the models from the literature and explore their application to the temperature profiling problem.

Immediately as energetic electrons strike a solid surface, some of the electrons are elastically back-scattered by low impact parameter collisions with surface atomic nuclei. The first issue in calculating electron energy deposition, then, is to find the fraction of electrons reflected from the surface. Empirically, the fraction of energy reflected is small, is insensitive to the phase of the target surface, and has only a weak dependence on the incident electron energy. However, the fraction of energy reflected is a strong function of the target atomic number(s), Z, and on the electron incidence angle.[2] The incidence-angle dependence is an important consideration for electrons striking a textured surface and this issue must be addressed as better computational models for baffle materials are developed.[3] Figure D-8 illustrates the Z dependence of the reflected energy fraction.[4] For the predominately low-Z baffle materials, the fraction of energy reflected is quite small, 5%, and is ignored for the moment.
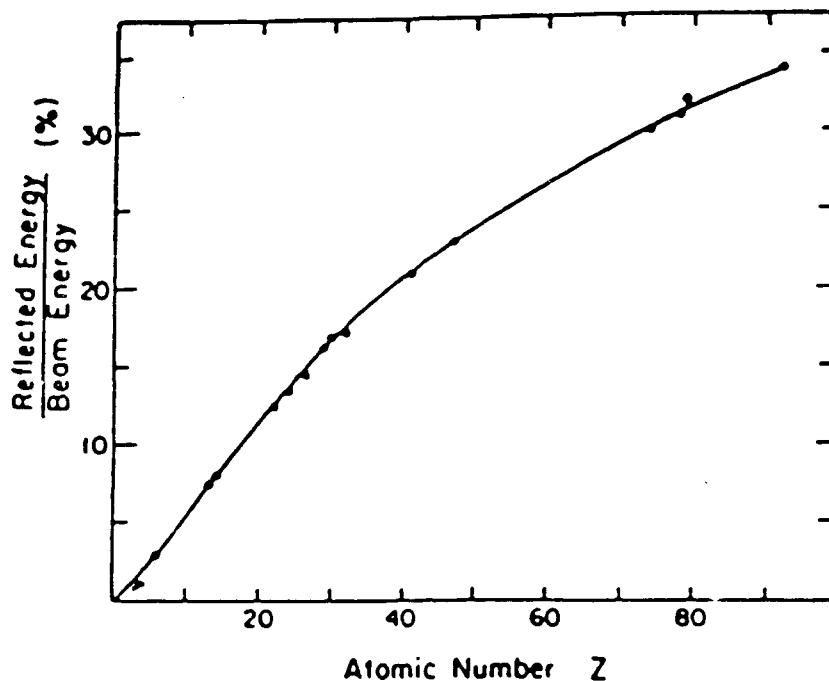
FIGURE D-8.   FRACTION OF ELECTRON ENERGY REFLECTED FOR 30 keV
ELECTRON INCIDENT ON DIFFERENT ELEMENTAL MATERIALS.

Having penetrated the surface, the interaction between energetic electrons and matter is characterized by three different types of collisions: close elastic, distant inelastic, and close inelastic. Because they are much heavier than electrons, target nuclei cannot absorb appreciable recoil momentum in close collisions. Thus, when a projectile electron approaches a target nucleus, the collision is essentially elastic, changing the electron's direction but not its speed.

In addition, projectile electrons have a long-range essentially inelastic interaction with the electronic structure of the target. This interaction occurs through collective target electron excitations, plasmons, and through excitations (or even ionizations) of target atoms. Since the energy transfer in each of these inelastic events is miniscule compared to the impinging electron's kinetic energy, their contribution is generally viewed as a continuous drag on the projectile electrons. In this 'Continuous Slowing-Down Approximation,' electrons deposit energy incrementally as they ricochet through the target under the influence of elastic collisions with target nuclei.[5] This is the basis of most of the analytic models of electron energy deposition as well as the Monte Carlo simulations.

Occasionally, projectile electrons are involved in catastrophic energy-loss events, such as knock-on collisions with single electrons in the target. The stochastic nature of these collisions broadens the depth profile of electron energy deposition and gives it a nearly gaussian shape. The collective phenomena are called energy straggling.

The consequence of these three interaction mechanisms is that the functional form of the electron energy deposition profile is fairly simple. The actual range of the electrons, that is the electrons' ultimate path length, and the energy deposited in the target is governed by the strength of the interaction between projectile electrons and states of target atoms. This is quantified in terms of atomic oscillator strengths, dipole matrix elements coupling 'before' and 'after' atomic states through the momentum of a plane-wave projectile electron state. Fortunately, for alumina, excellent tabulated atomic oscillator strengths are available.[6]

Since projectile electrons do not travel in a straight line, the mean-free path between elastic collisions controls the depth that the electrons penetrate beneath the surface. (We prefer "depth" to "projected range," sometimes found in the literature, because it avoids confusion with actual range.) Finally, the nature and frequency of energy straggling events determine the width of the final electron energy deposition depth distribution. The attraction of Monte Carlo simulations for this problem is in the natural way that these random events are included.[7]

To illustrate these concepts, Figure D-9 compare energy deposition calculations for 50 keV electrons incident on alumina. The 'SPIRE gaussian' curve is based on tabulated oscillator strengths which are available for alumina but are not available for most materials. The agreement with the public-domain ELTRAN[8] code is quite good.

30 μm ALUMINA
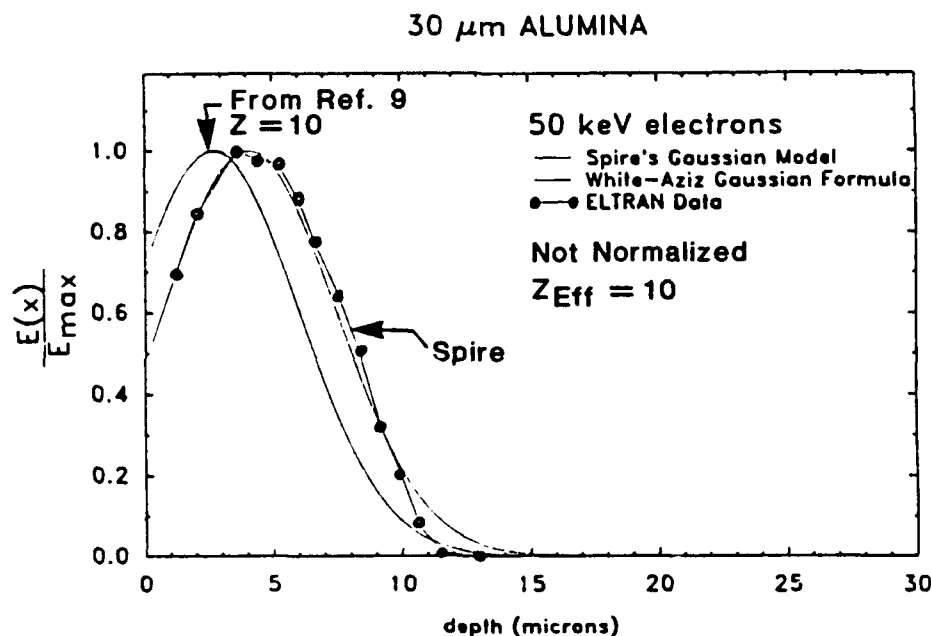
FIGURE D-9.   COMPARISON OF DIFFERENT E-BEAM MODELS.

D - 11

The curve labelled 'White-Aziz model' (cited in ref. 26, but originally from ref. 35) is a more general expression valid for electrons from 10 - 100 keV incident on elemental materials with atomic numbers from Z = 6 to Z = 50. In this model, the material is described only in terms of its atomic number and a simple empirical formula gives the electron range.[9] As indicated on the plot, the mean atomic number for Al_2O_3, Z = 10, was used for this calculation. Inspection reveals that both the depth and width of the distribution are too small.

Because of the convenience of this general formula, which is valid for many target materials, we made an effort to understand the discrepancy between the two gaussian models. One suggestion was that the volume density of electrons (# electrons/cm³) in the material was the crucial factor in determining the range of the electrons. Physically, this is reasonable since the volume density of electrons multiplies the result of the atomic oscillator strength calculation.[10] (For limitations on this approximation, consult ref. 10) Also, for elemental materials of roughly the same weight density, this effect would not have been noticed since the volume density of electrons scales as the atomic number.

To test this hypothesis, we define a Zeff to be Z for the heavier element in the compound times the ratio of the volume density of electrons in the compound to the volume density of electrons in the pure form of the heavy element. For the compound, the volume density of electrons is

$$\frac{Av \cdot \sum (Z)}{\rho \sum (m)}$$

Where Av is Avogadro's number. Evaluating this expression for alumina gives the result:

$$Z_{eff} = \left(\frac{Av \cdot \sum (z)}{\rho \sum (m)} \right) \left(\frac{\rho m}{Av z} \right) = 18.4$$

Figure D-10 shows the improved agreement with Zeff used in place of Z in the general model.

Programming was initiated to solve several problems with the existing procedure for computing temperature profiles for materials during pulsed electron bombardment. The previous method involved three separate programs (EBSPEC, ELTRAN, and VXTEMP) in three steps. This method was quite tedious and subject to innacuracies because of the manual data entry involved.

The HOTROD code was augmented to solve these problems. HOTROD runs on a PC, it accounts for heat flow during irradiation, it allows a changing energy spectrum, it allows access to temperature versus depth at any time and temperature versus time at any flagged depth, and
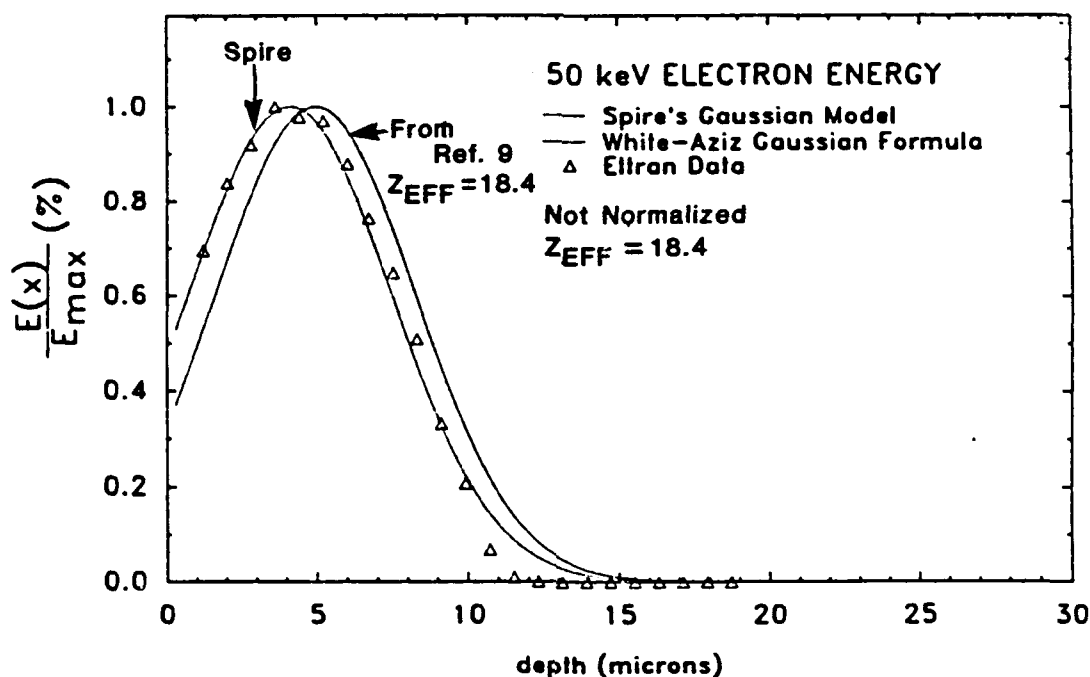
30 μm ALUMINA

FIGURE D-10. COMPARISON OF E-BEAM MODELS.

it allows the user to easily make changes to how it handles various variables (such as thermal conductivity and surface radiation) to see what variables make the biggest impact on the problem. Because the program is fast and easy to use; it interacts with the user primarily in terms of on-screen graphs. This makes the physics of the problem easier to see and understand. The program has been instrumental in tuning the SPI-PULSE 300 beam.

HOTROD first calculates energy deposition profiles from current and voltage traces according to user-selected time steps. At each time step, HOTROD interpolates between two measured voltage values and two measured current values to find the instantaneous current and voltage. The instantaneous voltage determines the depth and width of the electron energy depth/dose profile for that time step. The height of the depth/dose profile is normalized so that the integral under the depth/dose curve, $Q(z)dz$, is equal to the total energy deposited during the time step, $V(t)I(t)dt$.

HOTROD computes a depth/dose profile from instantaneous voltage values using an analytical gaussian function to represent the shape of the curve. This method has been documented extensively by researchers interested in electron energy loss for surface annealing with electron beams. This calculation proceeds as described above, and the results provide quantitative agreement with results from Monte Carlo calculations.

D - 13

The current-voltage trace from a 90 kV shot of the SPI-PULSE 300 is shown in Figure D-11. Figure D-12 shows the total depth/dose profile. The two numbers in the upper right corner represent the total fluence, the top in units of milliJoules/cm^2 and the bottom in calories*cm/grams. This computed total fluence allows the current and voltage traces to be compared with actual calorimeter readings.
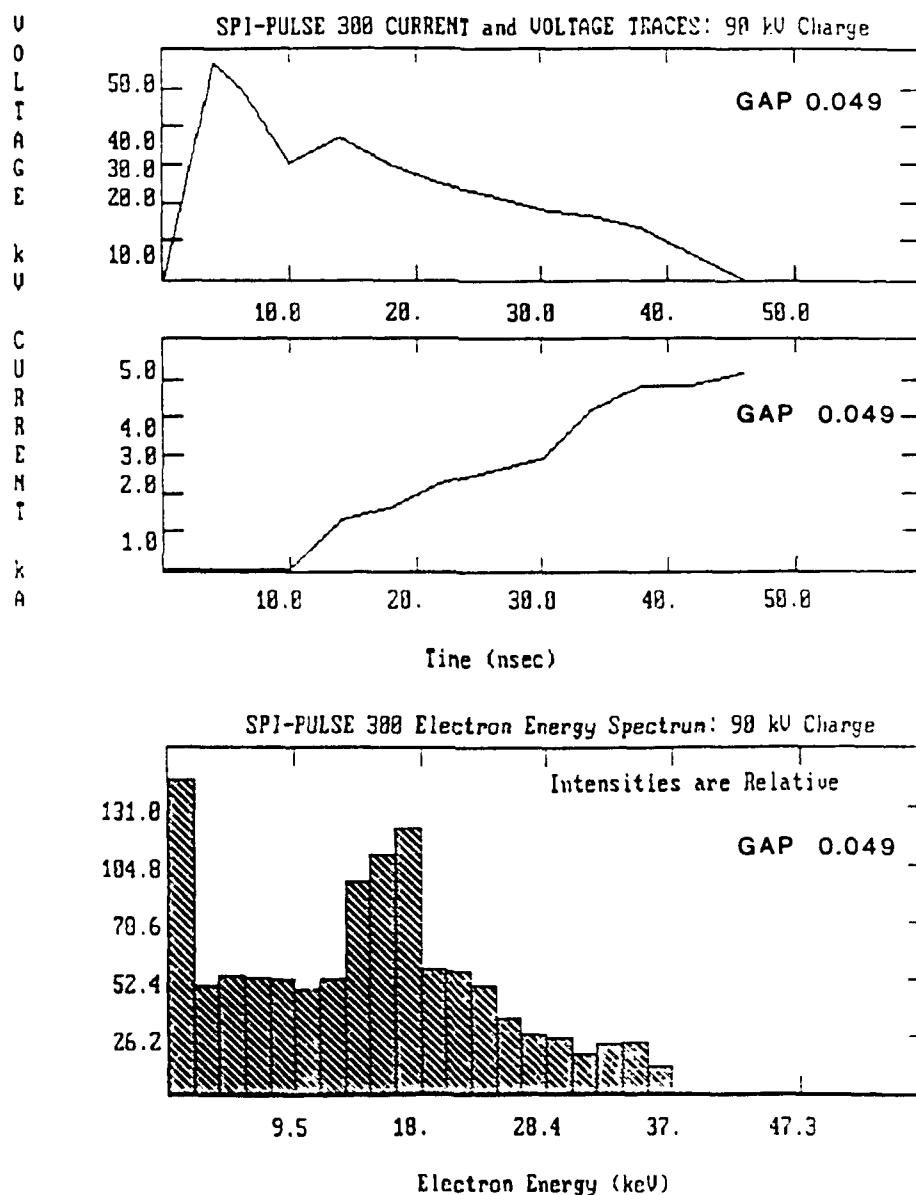

FIGURE D-11.   DIGITIZED CURRENT AND VOLTAGE FOR A TYPICAL SPI-PULSE
              SHOT ALONG WITH COMPUTED ELECTRON ENRGY SPECTRUM.

D - 14

TOTAL DEPTH-DOSE PROFILE
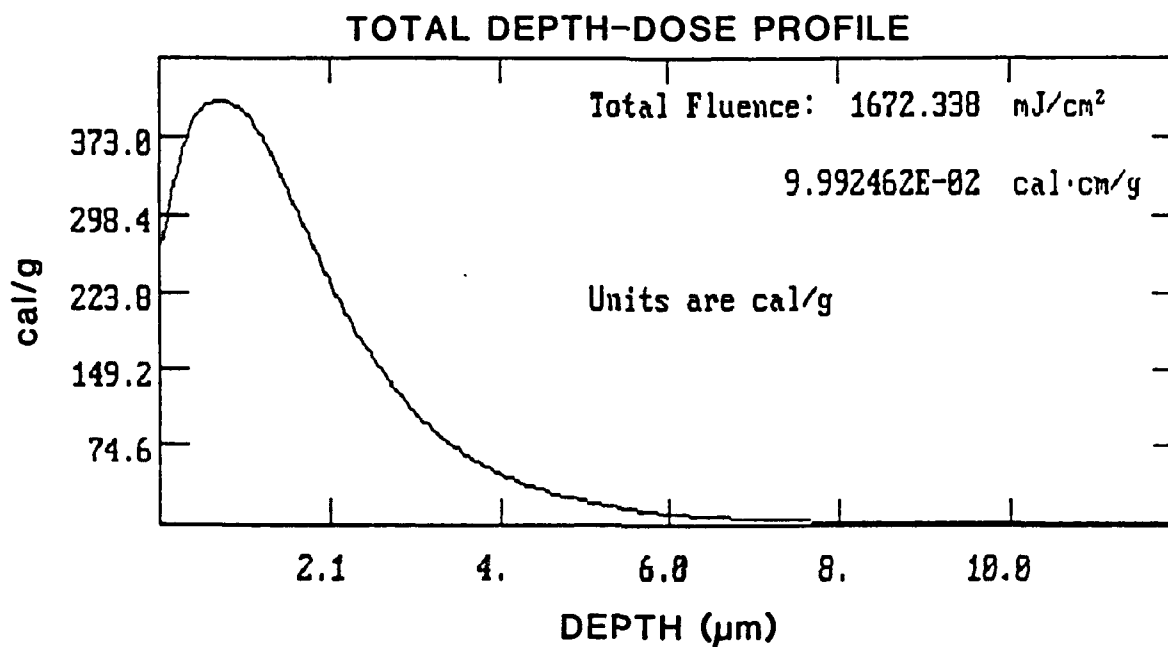
FIGURE D-12.   DEPTH/DOSE PROFILE PRODUCED BY HOTROD.

Figures D-13 and D-14 show two more useful graphs that HOTROD generates, temperature versus depth at any time (this one happens to be at time = 60 ns) and temperature versus time at any flagged depth (the depth flagged here is 0 micrometers, or the front face). All of these graphs were generated using the current and voltage traces from the SPI-PULSE 300 machine shown in Figure D-11.

TEMPERATURE PROFILE AT TIME 60
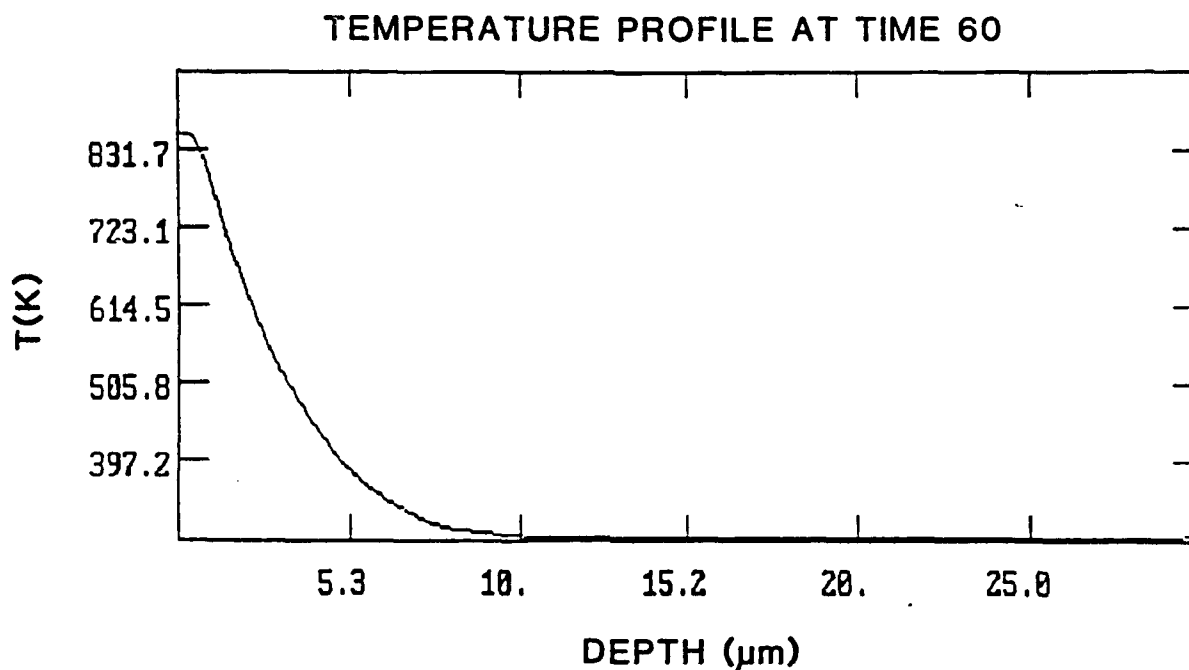
FIGURE D-13.   TEMPERATURE PROFILE PRODUCED BY HOTROD.

SPI-PULSE 300: 0.068, 100KV, Al$_2$O$_3$
FRONT FACE TEMP. vs. TIME
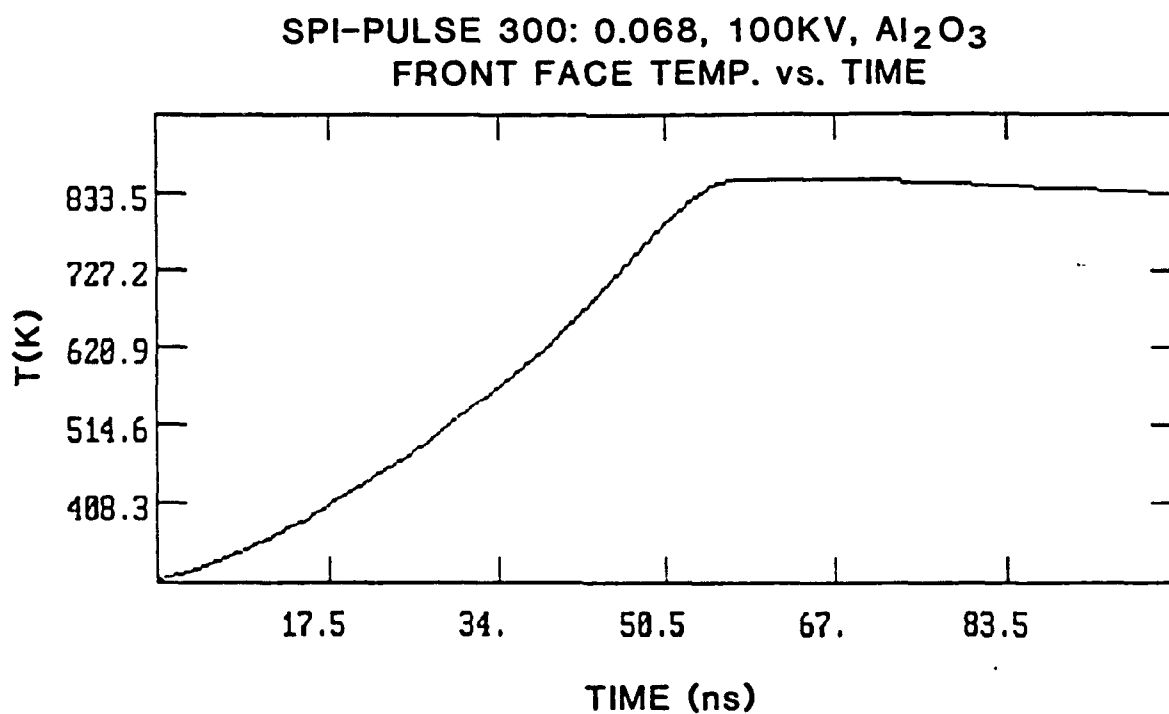
FIGURE D-14.   FRONT FACE TEMPERATURE VS. TIME PRODUCED BY HOTROD.

1. A. Goldsmith, H.J. Hirschhorn, and T.E. Waterman, Thermophysical Properties of Solid Materials, Wright Air Development Center, Technical Report 58-476, November, 1960.

2. E. Rimini in Surface Modification and Alloying by Laser, Ion, and Electron Beams, ed's J.M. Poate, G. Foti, and D.C. Jacobseon, NATO Conf. Proc. Series VI, Vol. 8, (Plenum Press, New York, 1983), Chapter 2.

3. SPIRE Corporation report, MR-10104-04, October, 1987.

4. M. von Allmen in Laser Annealing of Semiconductors, ed's J.M. Poate and J.W. Mayer (Academic Press, New York, 1982).

5. L.V. Spencer, Energy Dissipation by Fast Electrons, NBS Monograph 1, 1959.

6. J.C. Ashley, C.J. Tung, and R.H. Ritchie, IEEE Trans. Nucl. Sci. NS-22, 2533 (1975).

7. P.G. Merli and R. Rosa, Optik, 58, 201 (1981).

8. Sandia Corp., ELTRAN, One-Dimensional Monte Carlo Electron Transport Code, SC-TM-68-713, RSIC program number CCC-155.

9. L.C. Feldman, Phys. Rev. 17, 455 (1960).

10. A.T. Nelms, Energy Loss and Range of Electrons and Positrons, NBS Circular 577, 1956.

DISTRIBUTION LIST

Director
Strategic Defense Initiative Organization
Office of the Secretary of Defense
Washington, DC 20310
Attn: SDIO/SLKT (LTC M. Obal)

Director
Strategic Defense Initiative Organization
Office of the Secretary of Defense
Washington, DC 20310
Attn: SDIO/SLKT (Dr. J. Stubstad)

Director
Strategic Defense Initiative Organization
Office of the Secretary of Defense
Washington, DC 20310
Attn: SDIO/SLKT (LTC. C. Hill)

U.S. Army Strategic Defense Command
P.O. Box 1500
Huntsville, AL 35807-3801
Attn: CSSD-SL-K (G. Lowe)

U.S. Army Strategic Defense Command
P.O. Box 1500
Huntsville, AL 35807-3801
Attn: CSSD-SL-K (B. Hunter)

U.S. Army Strategic Defense Command
P.O. Box 1500
Huntsville, AL 35807-3801
Attn: CSSD-SL-S (R. Freeman)

U.S. Army Strategic Defense Command
P.O. Box 1500
Huntsville, AL 35807-3801
Attn: CSSD-SL-SA-EV (R. Bradshaw)

U.S. Army Strategic Defense Command
P.O. Box 1500
Huntsville, AL 35807-3801
Attn: CSSD-SL-SA-EV (R. Crowson)

U.S. Army Strategic Defense Command
P.O. Box 1500
Huntsville, AL 35807-3801
Attn: CSSD-SL-SA-EV (G. Pollock)

U.S. Army Strategic Defense Command
P.O. Box 1500
Huntsville, AL 35807-3801
Attn: CSSD-HE-A (B. Reeves)

U.S. Army Strategic Defense Command
P.O. Box 1500
Huntsville, AL 35807-3801
Attn: CSSD-H-Z (R. Buckelew)

U.S. Army Strategic Defense Command
P.O. Box 1500
Huntsville, AL 35807-3801
Attn: CSSD-H-Z (J. Katechis)

U.S. Army Strategic Defense Command
P.O. Box 1500
Huntsville, AL 35807-3801
Attn: SFAE-SD-GST (M. Pickens)

Air Force Weapons Laboratory
Kirkland AFB, NM 97117-6008
Attn: NTC/LT M. Black

Commander,
U.S. Army Missile Command
Redstone Arsenal, AL 35898
Attn: AMSIMI-RD-AS-OG (G. Hutcheson)

Naval Weapons Laboratory
Code 3818
China Lake, CA 93555-6000
Attn: T. Donovan/Linda Johnson

U.S. Army Harry Diamond Laboratories
2800 Powder Mill Road
Adelphi, MD 20783
Attn: SLCHD-NW-RH (C.J. Scozzie)

U.S. Army Research Office, Physics
P.O. Box 1211
Research Park, NC 27709
Attn: Dr. David Skatlud

Rome Air Development Center
Griffiss, AFB NY 13441-5700
Attn: RADC/OCSE (W. Kaveney)

Defense Technical Information Center
Cameron Station
Alexandria, VA 22314-5000

Breault Research Organization, Inc.
4601 East First Street
Tuczon, AZ 85711
Attn: R. Breault

Hughes Danbury Optical System, Inc
110 Wooster Heights Road
Danbury, CT 06810
Attn: MS848 George Gardopee

Hughes Aircraft Company
Electro-Optical and Data Systems Group
Building E1 Mail Station A133
P.O. Box 902
El Segundo, CA 90245
Attn: T.W. Daley

Institute for Defense Analysis
1801 North Beauregard Street
Alexandria, VA 22311
Attn: Janet Sater

Kaman Sciences Corporation
1500 Garden of the Gods Road
P.O. Box 7463
Colorado Springs, CO 80933-7463
Attn: Doug Caldwell

Martin Marietta Energy Systems, Inc.
P.O. box 2009
Oak Ridge, TN 37831-8063
Attn: A. Akerman

McDonnell Douglas Astronomies
5301 Bolsa Avenue
Huntington Beach, CA 92647
Attn: J. Tracy

McDonnell Douglas Astronomies
5301 Bolsa Avenue
Huntington Beach, CA 92647
Attn: J. Davidson

McDonnell Douglas Astronomies
5301 Bolsa Avenue
Huntington Beach, CA 92647
Attn: H. Rose

McDonnell Douglas Astronomies
5301 Bolsa Avenue
Huntington Beach, CA 92647
Attn: J.J. Grossman

Physitron, Inc.
Suite 101
4575 Hilton Parkway
Colorado Springs, CO 80907
Attn: P.L. Jessen

Mission Research Corporation
P.O. Drawer 719
Santa Barbara, CA 93102
Attn: R.W. Hendrick, Jr.

Lockheed Missiles and Space Company, Inc
0193-10b/204
Palo Alto, CA 94304-1187
Attn: C.M. Packer

Nichols Research Corporation
4040 South Memorial Parkway
Huntsville, AL 35802
Attn: W.R. Mendes

Physitron, Inc.
3325 Triana Blvd. Suite A
Huntsville, AL 35805
Attn: R. Skarupa

Rockwell International Autonetics Strategic
Systems Div., Defense Electronics Operations
3370 Muraloma Avenue
Anaheim, CA 92803-4192
Attn: P. Dahlgren BD21

Rockwell International Autonetics Strategic
Systems Div., Defense Electronics Operations
3370 Muraloma Avenue
Anaheim, CA 92803-4192
Attn: J.S. Matyuch OB49

Sparta Corporation
9455 Towne Centre Drive
San Diego, CA 92121-1964
Attn: L. Dunbar

Sparta Corporation
9455 Towne Centre Drive
San Diego, CA 92121-1964
Attn: G. Wonacott

Teledyne Brown Engineering Company
300 Sparkman Drive
Huntsville, AL 35807-7007
Attn: MS-50 C.E. Patty

U.S. Army Materials Technology Laboratory
Arsenal Street
Watertown, MA 02172-0001
Attn: SLCMT-BM J.F. Dignam

U.S. Army Materials Technology Laboratory
Arsenal Street
Watertown, MA 02172-0001
Attn: SLCMT-BM R. Fitzpatrick

U.S. Army Materials Technology Laboratory
Arsenal Street
Watertown, MA 02172-0001
Attn: SLCMT-BM F.P. Meyer

U.S. Army Materials Technology Laboratory
Arsenal Street
Watertown, MA 02172-0001
Attn: SLCMT-PRA

U.S. Army Materials Technology Laboratory
Arsenal Street
Watertown, MA 02172-0001
Attn: SLCMT-TML

AD _____ UNCLASSIFIED

UNLIMITED DISTRIBUTION

Key Words:
Optical baffles
Optical seekers
Aluminum alloys

U.S. Army Materials Technology Laboratory
Watertown Massachusetts 02172-0001
ADVANCED BAFFLE MATERIALS
TECHNOLOGY
Edward A. Johnson
Spire Corporation
One Patriots Park
Bedford, MA 01730-2396

Technical Report MTL TR 91-38, Oct. 1991, 78 pp - illus-tbls, Contract DAAL04-87-C-0036
D/A Project 63224C
Final Report, June 1987 - September 1990

Optical baffles reject off-axis stray light in strategic defense sensor systems. Materials must perform in operational and threat environments without contaminating the system. Traditional coatings shed particles which could compromise system signal-to-noise. Critical examination of failure modes suggested an innovative approach for superior baffle materials. Ion beam textured metals, as dark as the best traditional materials, are not damaged by ordinary handling and produce no contamination in shock and vibration tests.

END